Improvement of the Correlation between ALSE and BCI by Adjusting the Feeding and Positioning Conditions Based on Indirect Measurement of Termination Impedances Using Current Transformers

A Thesis Submitted to the Faculty of Electrical Engineering and Information Technology of Technische Universität Dortmund in Partial Fulfillment of the Requirements for the Degree of Doctor of Engineering Sciences (Dr.-Ing.)

by

Dipl.-Ing. Seyyed Ali Hassanpour Razavi

Dortmund, 2018

Date of Oral Examination:	23.05.2018
Supervisor:	Prof. Dr.-Ing. Stephan Frei
Second Supervisor:	Priv.-Doz. Dr.-Ing. Dirk Schulz

Abstract

The most commonly used automotive immunity test methods for electrical interferences from narrowband radiated electromagnetic energy are described in ISO 11452 series. Bulk Current Injection (BCI) and Absorber Line Shielded Enclosure (ALSE) apply different coupling mechanisms to assess the immunity of electronic components. While ALSE subjects the entire test setup to the electromagnetic fields generated by an antenna, BCI induces the interference signals directly into a certain part of the wiring harness by a current injection probe. ALSE is often considered as the more reliable method. However, testing with BCI is preferred as it allows performing the immunity tests in less time with less effort and cost. Despite using similar test setups, different interference currents are injected into the terminal units at each test method and therefore, the correlation between the test results is often poor.

In order to improve the correlation, the BCI method must be modified to inject the same interference current as the ALSE method. This thesis proposes an approach that searches for these modifications and makes it possible to inject the same interference currents with a BCI probe. The two main issues of concern are the calculation of the injected interference currents during real test scenarios in a simulation environment and, the measurement of the input impedance of terminal units under the operation condition using optimized current transformers. The developed models and measurement methods are combined to reproduce the ALSE currents with a single BCI probe. In line with the implementation scheme: firstly, a measurement-based approach to model the ALSE and BCI couplings to a wire-over-ground structure is developed. These models are used to determine the interference currents at the terminal units; secondly, theoretical and measurement based methods are developed to characterize current transformers. The goal is to assess the ability of a current transformer to measure the input impedance of the terminal units without disconnecting the wiring harness; thirdly, four non-invasive methods to measure the input impedance of terminal units using optimized current transformers are proposed and experimentally validated; finally, an approach to reproduce the ALSE termination currents with a single BCI probe according to an optimization process is developed and validated. Capabilities and limitations of the proposed methods and approaches are analyzed, discussed, and ultimately applied to a real immunity test setup.

.

Contents

Abbreviations

ALSE	Absorber Lined Shielded Enclosure
BCI	Bulk Current Injection
EUT	Equipment Under Test
EMI	Electromagnetic Interference
EMC	Electromagnetic Compatibility
DUT	Device under Test
AE	Auxiliary Equipment
CT	Current Transformer
SNR	Signal-to-Noise Ratio
TEM	Transverse Electromagnetic
MTL	Multiconductor Transmission Line
IF	Intermediate Frequency
SMD	Surface-Mounted Device
SPICE	Simulation Program with Integrated Circuit Emphasis
CM	Common Mode
IC	Integrated Circuit
CP	Current Probe
CT	Current Transformer
PCB	Printed Circuit Board
SWR	Standing Wave Ratio
KVL	Kirchhoff's Voltage Law
KCL	Kirchhoff's Current Law
SFG	Signal Flow Graph
CUT	Conductor Under Test
CW	Continuous Wave
VSWR	Voltage Standing Wave Ratio
RF	Radio Frequency
SPM	Single Probe Method
DPM	Double Probe Method
CDM	Current Distribution Method
ESPM	Extended Single Probe Method

ISO	International Organization for Standardization
CISPR	International Special Committee on Radio Interference
IEC	International Electrotechnical Commission
MATLAB	Matrix Laboratory

1 Introduction

Electromagnetic interference (EMI) generated by an external source can affect electric circuits under normal operation conditions. The growing number of electronic components in vehicles for monitoring, controlling and displaying various car and engine conditions or driver-assistance systems underlines the necessity of considering the electromagnetic environment in which these components operate. In general, interferences can have diverse electrical characteristics and contain a wide frequency spectrum. These interferences spread to on-board electronic components and may result in performance degradation, malfunction or even the total failure of the electronic components.

EMI is commonly divided into several categories according to the source and signal characteristics. However, to highlight the distinction in a more general manner, EMI can be classified in two types. While the narrowband EMI occupies a single frequency or a narrowband of the electromagnetic spectrum which may emanate from intended sources, the broadband EMI occupies a relatively large part of the electromagnetic spectrum and is mainly unintentional. The main focus in this work lies on the narrowband EMI.

In order to evaluate the component immunity characteristics for passenger cars and commercial vehicles, ISO 11452 provides various testing methods. The test methods, procedures, test instrumentation and levels specified in ISO 11452 are intended to facilitate component specification for electrical disturbances by narrowband radiated electromagnetic energy. A basis is provided for mutual agreement between vehicle manufacturers and component suppliers intended to assist rather than restrict. Not all test methods need be used for a given device under test (DUT), as they may provide very similar exposure to the DUT.

ISO 11452 part 2 is often called the absorber-lined shielded enclosure (ALSE) test and specifies the immunity testing by means of radiated electromagnetic fields, which are generated using antenna with a radio frequency (RF) energy source capable of producing the desired field strengths [1]. On the contrary, ISO 11452 part 4 specifies the bulk current injection (BCI) test based on current injection into a wiring harness using a current probe as a transformer, where the wiring harness forms the secondary winding [2].

ALSE and BCI are among the most common test procedures, where the electromagnetic energy is coupled in different ways to the wiring harness. While the ALSE method requires a large and costly anechoic chamber with specialized capabilities such as high-power amplifiers and is performed throughout a very sensitive calibration procedure, the number of requirements for the BCI method is much lower. From the standpoint of the power amplification, the main advantage of applying BCI is that the

low injected RF power can induce currents that would require very high radiated RF input power in case of ALSE. On the other hand, the BCI test can be carried out in a smaller shielded enclosure instead of a large anechoic chamber. Additionally, due to lower test requirements, the test can be performed more easily and repeated several times at early design stages. Due to these reasons, the BCI method is often used as the substitute for the ALSE method.

Unfortunately, the correlation of BCI to ALSE is often low. Several theoretical and experimental studies have demonstrated that radiation and injection cannot be made equivalent [3-11] in a strict sense. The reason is the different coupling mechanism during the ALSE and BCI methods. While the ALSE method gives rise to distributed coupling along the whole length of the wiring harness, the BCI method acts as a lumped source of a common mode voltage. As a consequence, the search for general conditions (even if approximate) has led to a concept that bypasses several complexities and limitations by focusing on the effect, i.e. the currents at the terminal units. This is not a limitation, since the final goal of the BCI testing is reproducing the same current levels determined by radiation at the input pins of the DUT, rather than generating the same current profiles along the wiring harness. Therefore, it has been further developed by many research groups both theoretically and empirically. However, none of the proposed methods has as yet been shown to be applicable as a substitute for the ALSE method. This implies the need to search for a coherent and pragmatic approach, which provides solutions that are practical and effective. This problem is solved in this work, by means of an optimization method, which minimizes the deviation between the ALSE termination currents (reference values) and the BCI termination currents. Such method not only requires high accurate models for the ALSE coupling and BCI coupling but also a detailed information about the input impedance of terminal units. The wiring harness can have linear or nonlinear terminations (loads). Making assumptions about the choice of termination is of paramount importance to derive general results. The focus in this work remains on the simpler but more specific case of linear terminations, which can be characterized in terms of impedances. Although assuming linear loads is certainly a limitation, it allows deriving analytical expressions in the frequency domain for the currents injected into a specific termination. Substituting large and complex systems with impedances (when observed at the ports) is consistent with the fact that the behavior of such systems is usually dominated by the impedance of their input stage [7][10]. By exploiting these assumptions, it will be possible to investigate whether similar currents at the input pins of terminal units can be achieved. In order to remain operational, the DUT must be connected to the load simulator. Therefore, the input impedance cannot be measured directly. This implies applying non-invasive methods, e.g. inductive or capacitive methods, to measure the impedance along the wiring harness, which is a function of the input impedance of the terminal units. This is done in

this work by proposing different inductive methods using toroidal current transformers such as a BCI probe.

1.1 Current State of Research

The current state of research has been categorized in four topics including: formulation and modelling of the field coupling (radiation), formulation and modelling of the bulk current injection, comparative investigations between methods and non-invasive methods to measure the impedance using current transformers.

One of the first models describing transmission lines, excited by an external electromagnetic source for the special case of a two-wire system was presented in [12]. The model was expanded to multiconductor transmission lines (MTL) in [13]. The forcing functions in this modelling approach are added to the coupling equations in terms of the vertical-electric and transverse-magnetic excitation fields. Further formulations of the field-to-MTL coupling has been proposed, where the forcing functions are expressed either only in terms of electric excitation field [14] or only in terms of magnetic excitation field [15]. Several other research teams have provided different approaches to model and analyze ALSE based on measurement or simulation methods, e.g. finite element method, Finite-difference time-domain or method of moments [16-23]. Both simulation and measurement approaches can be used to generate passive or active model of immunity test setups. The model is then applied to determine the generated disturbance in terms of forward power into any arbitrary load at the wiring harness ends.

The first analytical model to analyze the effect of the BCI probe's position, the length of the transmission line and the input impedance of terminal units is given in [24]. The comparison between the calculated and measured results in [24] demonstrates the accuracy of this modelling approach to predict the current distributions during the BCI testing. The information reported in latter publications commonly focus on two main topics: the modelling approach for BCI and the influence of certain BCI parameter on the test results. In particular, the modelling approaches require either an accurate deembedding of fixture-related effects or a detailed knowledge of the geometry of the BCI probe interior parts. Similar to the ALSE modelling approaches, the models are intended to perform the tests in simulation environments prior to the real implementation.

The comparative results between ALSE and BCI published in [3-11] indicate a significant difference between the current distributions. Furthermore, for radiated excitation, considerable differences in current distribution occur for different incidence angles and polarizations [3-4]. This draws the attention to the problem that not only the BCI current distribution does not correspond to radiation source but also there is no

unique radiated field excitation against which the BCI could be compared to. The general comparison of the current distribution in [5] indicates that the BCI testing tends to produce a more significant standing wave on the wiring harness, which is significantly influenced by the location of the BCI probe. Additionally, greater variation in the per wire current is expected by radiated fields than BCI. From theoretical point of view, even in case of the simplified excitations model, the solution for the BCI coupling equations cannot be satisfied with one injection probe. This means that only one BCI probe is not sufficient to assure the equivalence, at least in the general case [9]. Therefore, in recent years, increasing attention has been being paid to the double bulk current injection (DBCI) as a solution to improve the correlation between ALSE and BCI. The primary idea is to offer the advantage of reproducing the same injection currents in the loads as those obtained in the case of plane wave coupling modes by means of two BCI probes. Principally, the method compares the effects that the sources produce at the terminal ports, with the aim to control the probe's voltage in order to match the incident field characteristics. The approach yields results, which are not affected by any assumption on the terminal network. There are, however, several critical issues connected to the application of the DBCI such as: application of simplified circuit models of BCI in theoretical validation which neglects high-frequency phenomena occurring in the ferrite core and in the probe windings and the assumption of specific uniform plane-wave fields. In case of multiconductor transmission lines (MTL), only the common mode (CM) parameters of MTL and the CM impedance of DUT and load simulator are considered. Unfortunately, the approach gives no indication on how to obtain these parameters and assumes them as known. Additionally, the experimental results are validated only for a single wire over a ground plane. As the overall accuracy of the procedure is strictly related to the degree of uncertainty in the knowledge of the system parameters, the real implementation could face severe difficulties.

Although the physical properties and the application of ferrite cores to develop a variety of current transformers or current probes have been in the focus of interest in the last decades, specific application of transformers or current probes to measure the impedance has not gained much attention. The first application of two current probes to measure power-line impedances in the frequency range from 20 kHz to 30 MHz is developed and proposed in [43]. Other research teams improved the frequency range of measuring the power-line impedances up to 1 GHz, by introducing new calibration procedures [44-48]. The latest calibration procedure is based on a more general treatment of the equivalent circuit of the measurement system by modelling it as a general three-port network. Additionally, the definition of the CM loop impedance is first introduced by [49] instead of the ambiguous definition of CM impedance. Moreover, a non-invasive measurement method to characterize the CM loop impedance using two clamp-on current probes is presented in the same publication. In [50] and [51], a simple

approach to remove the effects of transformer from a reflection measurement with network analyzer and the pros and cons of the impedance measurement with different transformers and current probes are presented. Particularly, in [51], in order to improve the measurement, the idea of a so called “impedance probe” is proposed and the application of such probe with appropriate physical characteristics to measure the local impedance along a transmission line is analyzed. Moreover, in [52], the application of current probes to measure the input impedance of an ESD generator with both reflection method and double current probe are shown, where the frequency response of the current probe is de-embedded from direct measurement to determine the impedance up to 1 GHz. However, besides specific results and features developed in the last decades, no specific application on immunity testing is reported.

1.2 Scope of Research

An overview of the main parts of this thesis is illustrated in Figure 1.1. Based on ISO 11452, the term “load simulator” represents a physical device including real or simulated peripheral loads which are necessary to ensure DUT nominal or representative operation mode. Furthermore, the terms “wiring harness” and “test harness” are used interchangeably to indicate a wire bundle, wire harness or cable bundles between DUT and load simulator.

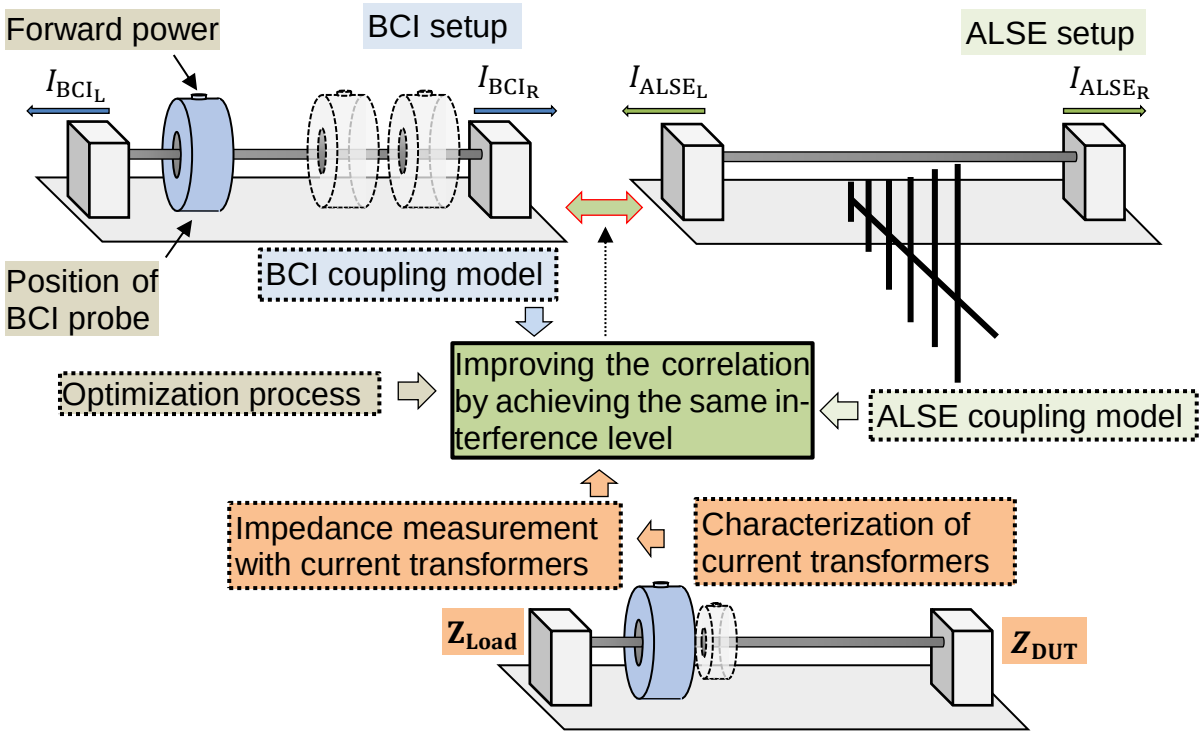

Figure 1.1: Improving the correlation between ALSE and BCI by reproducing the same interference levels with a BCI probe as during the ALSE method

The first goal will be the development of a high accurate modelling approach to simulate the ALSE and BCI coupling. The coupling models will be used to determine the

interference currents at the harness ends, which are terminated in arbitrary loads with known impedances. The second goal will be the characterization of sample commercial and optimized current transformers, to assess their ability to perform impedance measurement. The details and information obtained in this way will be used to investigate the idea of using current transformers as impedance probes in combination with vector network analyzers. The third goal will be to introduce different methods to characterize the termination impedances using a current transformer without disconnecting the wiring harness from the terminal units. The ultimate goal will be to combine the coupling models and the measured impedances with current transformers in an optimization process to minimize the deviation between the ALSE and BCI currents.

The structure of this thesis is arranged in the following order. Chapter 2 describes a measurement-based approach to model the ALSE and BCI and to determine the termination currents according to ISO 11452. Chapter 3 focuses on physical analysis and modelling of transformation phenomenon. Indications on the feasibility, strength and weakness of using different current transformers to measure the impedance are given and discussed. Chapter 4 proposes several methods to characterize the impedance of terminal units up to 1 GHz indirectly by means of current transformers. Finally, in Chapter 5, a possible application of the BCI method to substitute the ALSE method using the optimization process is introduced, investigated and discussed.

2 Measurement-Based Modelling of Immunity Test Setups

The behavioral modelling of the system-level EMC setups based on ISO 11452-2 and ISO 11452-4 has a high practical relevance. Different techniques have been proposed in the recent years to model the field excitation with antennas and the current injection with current transformers [12-32]. Despite the significant importance of these techniques to analyze the influence of different setup parameters or to predict the test results in advance, the complex and laborious ways to deal with the problem commonly result in lack of interest to use them for the real test situations. One possible solution to this problem is to use the “black box approach” based on S-parameter measurement. The idea is to describe a certain part or the entire ALSE and BCI setups, including the interference source and the wiring harness, in terms of their inputs and outputs without any knowledge of their internal structure. This can be used then to determine the amount of the coupled interference into the termination networks. The main goal in this chapter is therefore, to develop a fast and accurate measurement-based method, which allows determining the interference signal levels at the DUT and load simulator in a simulation environment. The proposed modelling method will be further used to obtain accurate models of a current transformer in Chapter 3, and to realize an optimization process to improve the correlation between ALSE and BCI in Chapter 5.

In this chapter, first of all, a brief overview of the general test conditions including the specified setup arrangement and signal levels for both test methods are given and compared according to ISO 11452. Secondly, in order to highlight the contrast between ALSE and BCI, the results obtained from a sample test scenario are given and compared. Following this, a method to characterize the homogeneous and inhomogeneous segments of a wire over ground structure in terms of per-unit-length parameters is proposed and validated. Subsequently, a method to extract measurement-based models of the BCI coupling (injection) and ALSE coupling (radiation) in immunity test setups is proposed and validated. Finally, the extracted models are used to determine the interference currents at the input ports of the termination networks.

2.1 Comparing Test Requirements and Sample Test Results

Since the introduction of the standard ISO 11452 in 1995, it has been modified several times [53]. As mentioned previously, Part 2 and part 4 of the standard represent ALSE and BCI, respectively. According to [53], the latest revision of part 2 and its approved document is the 2004 edition (ISO 11452-2:2004) [1]. The same revision of part 4 is ISO 11452-4:2004 [2], which has been the subject of minor changes since then. The latest revision of part 4 (ISO 11452-4:2011) has been renamed to “Harness Excitation Methods” [54]. In addition to the BCI method, it comprises the tubular wave coupler test method (TWC), which is based on the wave coupling into the wiring harness using the directional coupler principle [54]. In order to simplify the comparison

and to avoid version specific requirements, the latest concurrent revision of the ISO 11452, i.e. [1] and [2], is considered during this work, unless otherwise mentioned.

2.1.1 General Test Conditions Based on ISO 11452

A summary of the general conditions and basic principles of the component testing used in ISO 11452 is given in this section. Figure 2.1 shows the schematic representation of the main equipment prescribed for the ALSE and BCI tests located in an anechoic chamber.

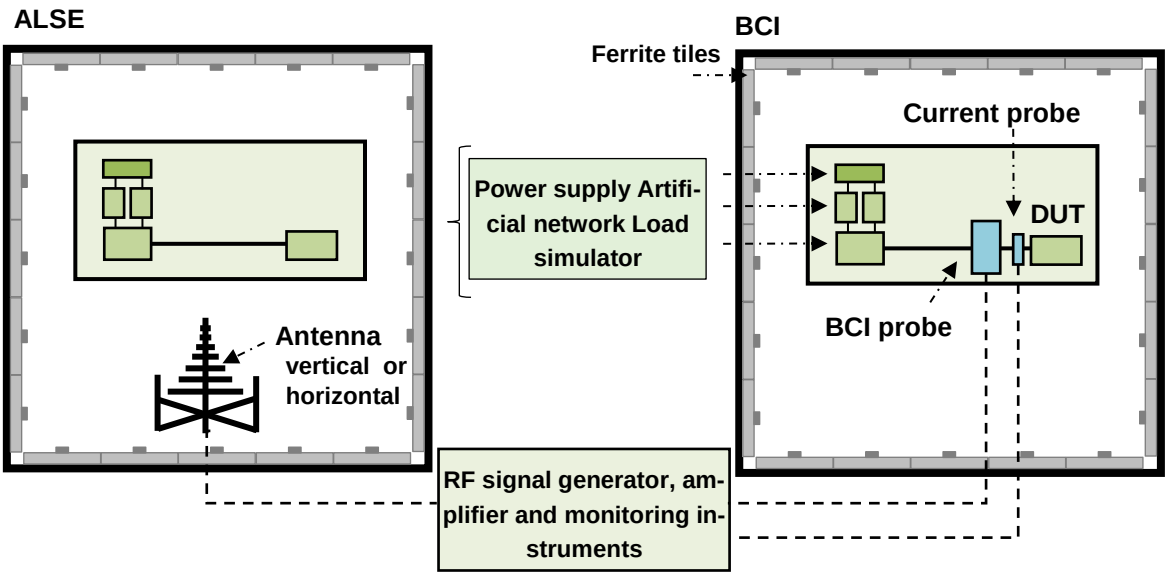

Figure 2.1: Schematic representation of the test setup during the ALSE and BCI methods. The green color represents the identical components at both test methods, which are either installed on the test bench or located outside the anechoic chamber.

A BCI test, according to ISO 11452 part 4, shall be performed in a shielded enclosure and is applicable for the automotive applications in the frequency range between 1 MHz and 400 MHz. Although, the standard recommends a shielded enclosure, it is left to the user whether to equip the enclosure with absorber materials. The BCI method comprises two different test procedures:

- substitution or open-loop method,
- closed-loop method with power limitation.

In substitution method, the required forward power to achieve a certain amount of current through a 50 Ω resistor is measured and recorded for each frequency separately (calibration procedure). The calibration must be performed in a standard calibration jig, where both opposite sides are terminated with 50 Ω resistors. The final testing is conducted by subjecting the DUT to the calibrated forward power level. The location of the BCI probe is prescribed at three different distances from the connectors of the DUT including 15 cm, 45 cm and 75 cm. Concerning the specified current at each severity level, there has been a minor change in the latest revision of the standard [54].

Table 2.1 gives the suggested severity levels for the BCI and ALSE methods according to [1], [2] and [54]. For the BCI method, the specified current at each severity level is divided in two columns, according to the revision number. From the table, it is clear that the amount of current specified at each severity level has been increased in the latest revision. On the contrary, during the closed-loop method, the forward power is increased up to the level, where the induced current reaches the specified test level or the forward power limit is reached. The forward power limit is in this case, unless otherwise specified, the fourfold of the calibrated forward power to meet a certain current value through the 50 Ω termination in the calibration jig.

Test severity level (BCI)	**Value (mA)**			**Test severity level (ALSE)**	**Value (V/m)**
	Rev. 2004	**Rev. 2011**			**Rev. 2004**
I	25	60		I	25
II	50	100		II	50
III	75	150		III	75
IV	100	200		IV	100
V	Specific value agreed between users			V	Specific value agreed between users

Table 2.1: Suggested test severity levels according to [1], [2] and [54] for the BCI and ALSE methods. The green color indicates the severity levels selected primarily for the comparison.

According to ISO 11452 part 2, an ALSE test, as indicated by its name, should be performed in a shielded enclosure equipped with absorber materials (anechoic chamber), where the free space environment is simulated for the relevant frequency range. The characteristics of the electromagnetic absorber used in the structure of chamber affects the reproducibility of the test results [56-58]. The ALSE method is specified for two antenna polarizations:

- vertical polarization between 80 MHz and 18 GHz,
- horizontal polarization between 400 MHz and 18 GHz.

For both polarizations, the forward power required to produce a specific field strength in a certain frequency is measured with a field probe (calibration procedure). The final test is performed by subjecting the DUT to the test signal based on the predetermined calibrated forward power for each antenna polarization. Based on the relevant frequency range, the test can be performed with different antenna types, which are described in detail in Section 2.3.2.

The standard ISO 11452 specify the exact arrangement and configuration of the test setup for each test method. A summary of the requirements given in Table 2.2 confirms the high similarity between the test setups. The length of the wiring harness in BCI setups is prescribed as 1000 mm in case of the closed-loop method, and 1700 mm in case of the substitution method. The part of the wiring harness parallel to the front edge of the ground plane shall be 1500 mm. However, the total length of the

wiring harness between the DUT and the load simulator (or the RF boundary) shall not exceed 2000 mm. Furthermore, the height above the metal reference plane is specified as 50 mm.

The electrical properties of the components involved in testing is only specified directly for the artificial network (AN) in the frequency range between 100 kHz and 100 MHz. The standard emphasizes that the common mode and/or differential mode impedance of each I/O pin connected to the DUT must be in compliance with the real application [55]. This open description allows a broad variety of RF impedances at the terminal units and will be discussed in Chapter 4.

Ground plane	• Thickness: 0.5 mm (minimum) copper, brass or galvanized steel • Width: 1000 mm (minimum) • Height: (900 ± 100) mm above the floor (ALSE)
Power supply and artificial network	• Power supply is connected to DUT through an AN • In case of remotely grounded DUT, two ANs are required (for the positive supply line and for the power return line) • In case of DUT locally grounded, one AN is required (for the positive supply)
Location of DUT	• (50 ± 5) mm above the metallic surface of the table on a non-conductive, low relative permittivity material ($\varepsilon_r \leq 1{,}4$) • 100 mm from the edge of the ground plane
Location of the load simulator	• Directly located on the ground plane • Bonded to the ground plane (in case of metallic case for load simulator)

Table 2.2: Similar structure of the test setup recommended for BCI and ALSE according to ISO 11452

Although the test equipment and the main arrangement of the components on the test bench are almost identical for both test methods, the main difference remains the excitation technique, which will be analyzed separately in this chapter.

2.1.2 Comparison Between Test Results

The primary step to highlight the similarities and differences between the ALSE and BCI methods is to create a proper scenario. For this purpose, as illustrated in Figure 2.2, a setup consists of a single wire over a ground plane is chosen. The wire is 1.7 meter in length and is terminated with a temperature sensor LM35 from Texas Instruments [60] (DUT) at one side and a passive load circuit at the other side. The single wire connects the analog output pin (VOUT) of the temperature sensor with the load circuit and is directly subjected to the interference signal generated with an antenna or a BCI probe. The ground pin (GND) of the DUT is connected directly to ground

plane. The DC output voltage is measured with an optical voltage sensor (Langer A200) connected to the load circuit and is monitored with an oscilloscope (LeCroy 7100). The entire process is controlled and monitored with a test software, designed for the immunity testing according to ISO 11452. The combination of the signal generator R&S SMA100A and the power amplifier PRANA DT150 is used to generate the RF interference signal during the tests. A detailed description of the test setup and components is given in Section 5.2. The sensor has only one functional mode, where the analog output (VOUT) is directly proportional to temperature. The 'fail' criterion is defined as 10% deviation from the nominal voltage of the VOUT pin before subjecting the sensor to interference (undisturbed value).

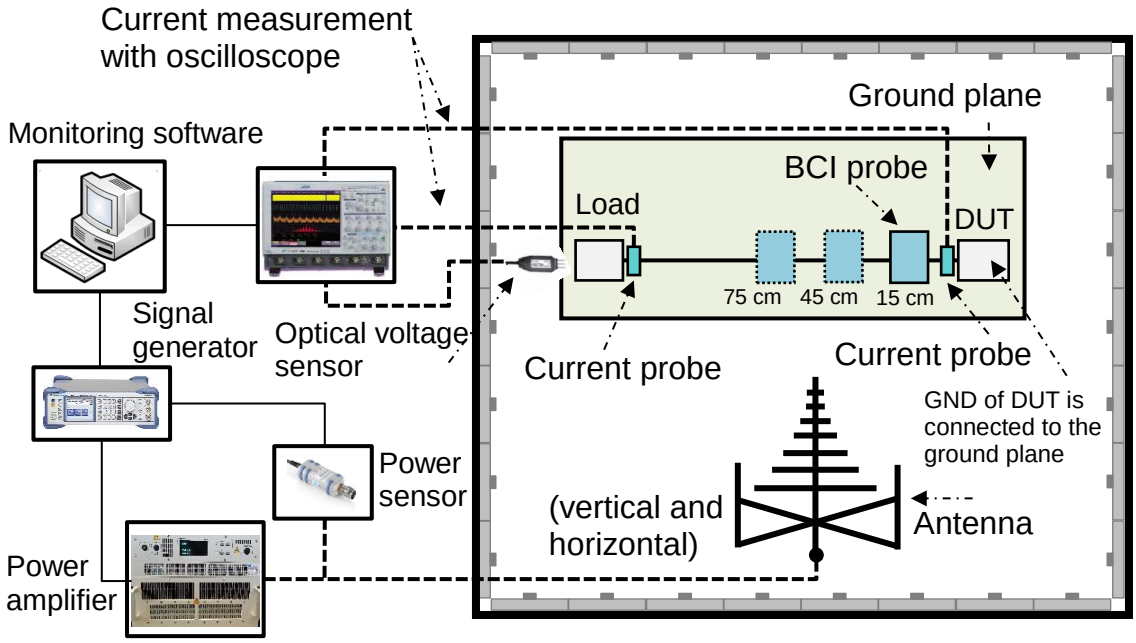

Figure 2.2: Schematic representation of the test setup and equipment during the ALSE and BCI methods

In order to select an appropriate severity level for the test scenario the following criteria are considered:

- choosing the highest possible severity level for the ALSE test with respect to the available antenna, signal generator and power amplifier,
- avoiding physical damage to the DUT during the test for the entire frequency range,
- at least one operational failure (fail) should occur during the ALSE test with both antenna polarizations.

Based on a primary investigation at different severity levels and the above-mentioned criteria, the severity level IV (100 V/m) is chosen for the ALSE test. The ALSE tests at

lower severity levels failed to produce at least one fail signal for both antenna polarizations. For the BCI test, the same severity level is chosen, i.e. severity level IV (100 mA), and both calibration and test are extended to 1 GHz. The upper limit for the forward power is restricted to 52 dBm. The ultimate immunity test is performed based on the substitution method for three different cases including:

1. ALSE with horizontal polarization of the antenna (brown),
2. ALSE with vertical polarization of the antenna (green),
3. BCI with injection probe located at 15 cm from DUT (blue).

The immunity level is defined as the highest power level that satisfies the pass criterion. In general, a typical test report includes merely the immunity levels obtained during the test in comparison to the calibrated forward power at a certain severity level [1-2]. Nevertheless, measuring the current magnitude close to the terminal unit gives a useful insight into the amount of interference levels during the test. According to ISO 11452, the test setup is subjected primarily to the calibrated forward power for the specified severity level. Following this, the power is decreased until the pass criterion is satisfied. The monitoring software records the current measured by injecting the calibrated forward power into the BCI or antenna. Although the BCI test results are commonly illustrated in logarithmic scale, the comparative results are illustrated here in linear scale to highlight the similarities and differences at the desired frequency range.

Figure 2.3 illustrates the comparison between the ALSE test results (green) and the BCI test results (blue) up to 1 GHz. The calibrated forward power to achieve 100 V/m and 100 mA are depicted in pink and red respectively. To begin, the ALSE method with different polarizations are considered. The comparison between the calibrated forward power and the measured immunity levels between 80 MHz and 1 GHz shows that the amount of power to reach the same electric field (100 V/m) is much lower in case of vertical polarization. Moreover, no obvious correlation between different antenna polarizations can be observed at frequencies, which satisfy the Fail criterion. For example, while the test is successful at 490 MHz with the vertical polarization, it fails with the horizontal polarization at the same frequency. It can be concluded from the results that there is no unique ALSE result and hence, each antenna polarization has to be considered separately.

The comparison between the test results for ALSE and BCI in this figure, can be primarily done at the frequencies between 80 MHz and 400 MHz. Overall, the calibrated forward power to reach the severity level IV is much lower in case of BCI at these frequencies. Moreover, the fail criterion is satisfied with extremely lower power levels during the BCI test. Nevertheless, it can be clearly seen, that the calibrated BCI

forward power increases significantly at higher frequencies and becomes almost similar to the calibrated ALSE forward power above 850 MHz. The current magnitudes demonstrated in Figure 2.4 confirm that higher amount of current is coupled into the termination networks during the BCI test for the calibrated forward power. Overall, the comparison between Figure 2.3 and Figure 2.4 indicates a very high correspondence between the measured current magnitudes and immunity levels.

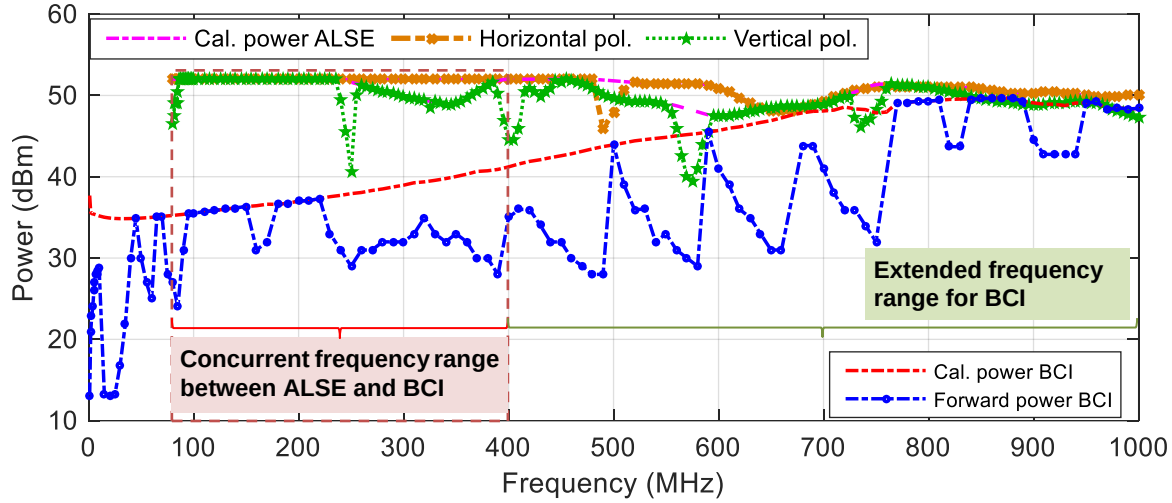

Figure 2.3: Comparison between the calibrated forward power and the measured immunity level for the severity level IV (100 mA) for the specified locations of the BCI probe according to ISO 11452-4

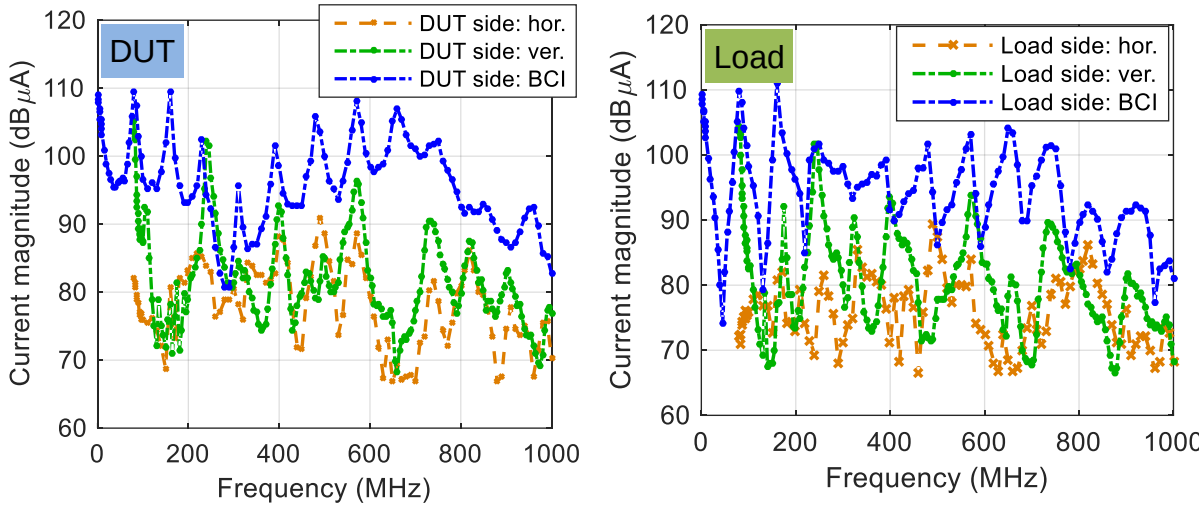

Figure 2.4: Comparison between the measured currents at the DUT side and the load side for BCI and both antenna polarizations at severity level IV

As describe in Section 2.1.1, a complete BCI test shall be performed at three different positions along the wiring harness. Therefore, the BCI test is repeated at the following positions:

1. injection probe located at 15 cm from DUT (dark blue, d=15 cm),
2. injection probe located at 45 cm from DUT (light brown, d=45 cm),
3. injection probe located at 75 cm from DUT (dark brown, d=75 cm).

The frequency range is extended up to 1 GHz and the calibrated forward power remains the same for all three setups. The immunity levels and the measured currents close to the DUT are shown in Figure 2.5. With the exception of the frequencies lower than 25 MHz, the immunity levels and the measured currents are different for each probe's position. This means that changing the position of the BCI probe directly affects the BCI test results especially at higher frequencies.

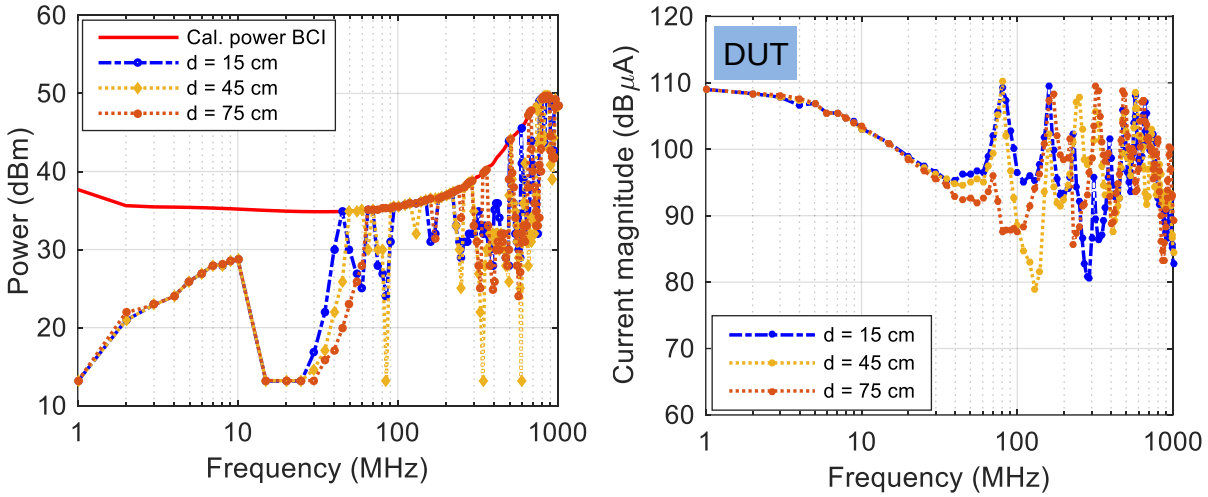

Figure 2.5: Comparison between the measured immunity levels at the specified positions at severity level IV (left), comparison between the measured currents at the DUT side with the BCI probe located at the specified positions at severity level IV (right)

As described before, the forward power was calibrated to inject 100 dBµA (100 mA) into the standard calibration jig for the entire frequency range. However, the actual injected current significantly differs from this value due to the length of the setup and the impedance of terminal units. This shows that the calibration of the power cannot provide accurate information on the signal actually injected into the DUT. Additionally, the comparison between the ALSE test results and BCI test results points out that none of the BCI probe's positions can directly substitute the ALSE method.

2.2 Modelling Approach for Injection and Radiation

In general, there are several ways to measure and represent a linear electrical network, including Z-, Y-, S-parameters, etc. The main advantage of S-parameters lies in the measurement concept, where no open and short circuits are required to obtain them [61]. However, the final network parameters can be converted from one form to the other based on mathematical operations defined in [63-64]. The physical meaning and properties of scattering parameters (S-parameters) are presented in e.g. [61], where incident and reflected normalized complex waves are used to characterize the electrical behavior of a linear network. Once the S-parameters of a network are determined, its behavior can be predicted for various steady state stimuli by electrical signals [61]. Without the loss of generality, the S-parameter modelling provides a "black box" model of a network, without any regard to the electrical components involved in

it. The interaction with other networks occurs only through ports, where the signals either enter or exit the network. This implies that the outside world has no coupling with internal elements of the network [64].

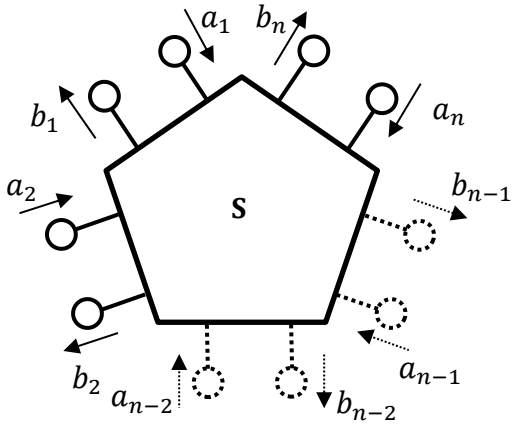

Figure 2.6: n-port network showing incident waves (a_1 a_2,…) and reflected waves (b_1 b_2,…) used in S-parameter definitions

The structure of a generic n-port network described in terms of S-parameter is illustrated in Figure 2.6. According to [61], the definition of the incident power wave a_i and the reflected power wave b_i are given by

$$a_i = \frac{V_i + Z_i I_i}{2\sqrt{|\mathrm{Re}(Z_i)|}} \tag{2.1}$$

and

$$b_i = \frac{V_i - Z_i^* I_i}{2\sqrt{|\mathrm{Re}(Z_i)|}}, \tag{2.2}$$

where V_i and I_i indicate the terminal voltage and current and Z_i indicate the reference impedance. The asterisk denotes the complex conjugate of the reference impedance. The S-parameters of a multiport network (n-port network) can be introduced in the context of matrix relationship by

$$\mathbf{b} = \mathbf{S}\mathbf{a}, \tag{2.3}$$

where **S** is a n × n matrix, which specifies the linear relation between the column vectors **a** and **b** describing the entire incident and reflected power waves. The diagonal elements of the S-parameter matrix S_{ii} and the off-diagonal elements S_{ij} indicate the reflection coefficients and transmission coefficients respectively.

2.2.1 De-embedding and Cascading of Different Networks

Combination of individual networks together to form a cascaded network or removal of the effects of the unwanted signal portions from a dataset (de-embedding)

can be done by means of appropriate mathematical operations on network parameters. Basically, each such mathematical action corresponds to introduce new equations or constraints to the main linear system of equations. This can be solved subsequently for the relevant variables to obtain a system of equations describing the new network.

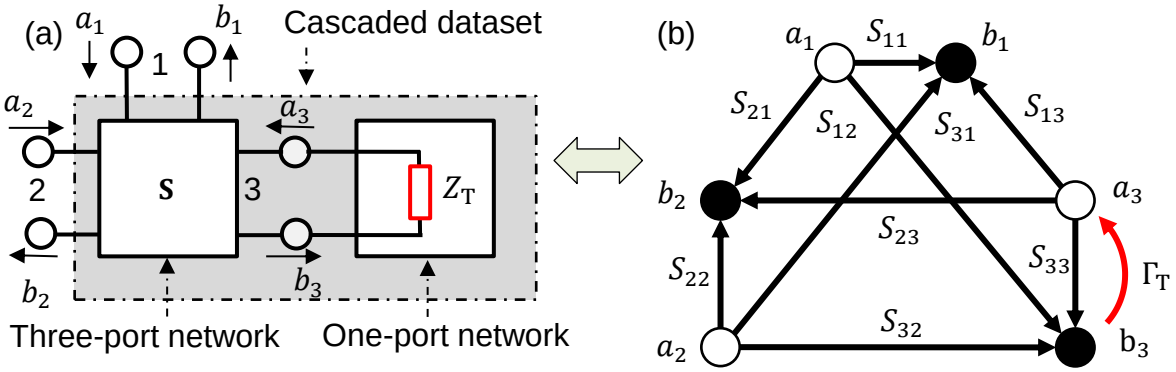

Figure 2.7: (a) Termination of a three-port network with a one-port network, (b) signal flow graph to demonstrate the incident and reflected power waves within the cascaded network

A sample procedure used to attach a single termination to a device is described below. The schematic representation of a cascaded network and the corresponding signal flow graph (SFG) is illustrated in Figure 2.7, where each port of the network is represented by two nodes indicating the incident and reflected power waves. The value of the connecting branches indicates the complex S-parameter. The effect of the one-port network is included in the SFG with the curved red arrow and the reflection coefficient Γ_T. Letting $\mathbf{S}$ represent the S-parameters of the three-port network and applying this to (2.3) yields

$$\begin{cases} b_1 = S_{11}a_1 + S_{12}a_2 + S_{13}a_3 \\ b_2 = S_{21}a_1 + S_{22}a_2 + S_{23}a_3 \\ b_3 = S_{31}a_1 + S_{32}a_2 + S_{33}a_3 \end{cases}. \tag{2.4}$$

A passive termination with the impedance Z_T attached to port 3 reflects the scattered wave b_3 back into the measurement device as a new incident wave a_3. This provides an additional equation

$$a_3 = \Gamma_T\, b_3, \tag{2.5}$$

where Γ_T is the reflection coefficient of the termination impedance in a 50 Ω system. The new equation allows solving the original system for the new reflected waves b_1' and b_2' in terms of a_1 and a_2 stimuli as

$$\begin{cases} b_1' = \left(S_{11} + \dfrac{S_{13}S_{31}\Gamma_T}{1 - \Gamma_T\, S_{33}}\right)a_1 + \left(S_{12} + \dfrac{S_{13}S_{32}\Gamma_T}{1 - \Gamma_T\, S_{33}}\right)a_2 \\ b_2' = \left(S_{21} + \dfrac{S_{23}S_{31}\Gamma_T}{1 - \Gamma_T\, S_{33}}\right)a_1 + \left(S_{22} + \dfrac{S_{23}S_{32}\Gamma_T}{1 - \Gamma_T S_{33}}\right)a_2 \end{cases}. \tag{2.6}$$

The S-parameters of the cascaded network, i.e. the new two-port network, can be recognized directly from (2.6). This approach can be expanded to obtain a more general form for an arbitrary dataset size and variable number of ports based on primary equations given in [61].

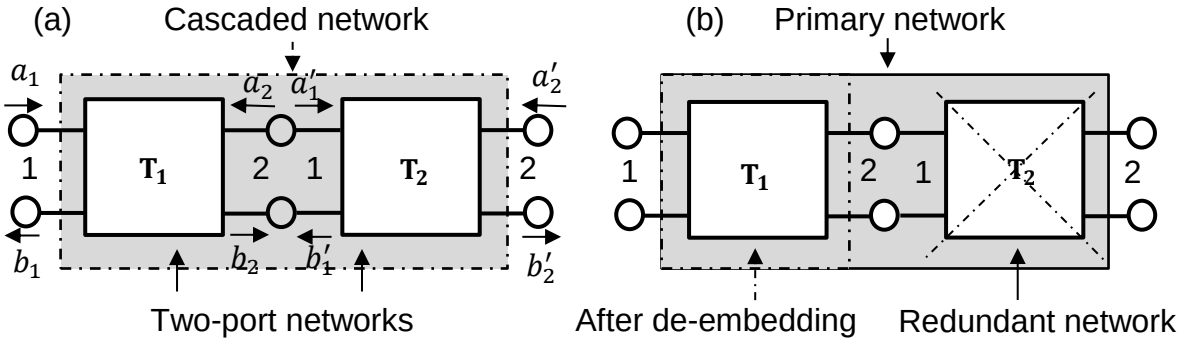

Figure 2.8: Application of T-parameter representation for: (a) combination of two two-port networks to obtain a cascaded network, (b) removal of the effect of a certain network from a primary network

However, using scattering transfer parameters (T-parameters) is a more convenient and straightforward approach to cascade or de-embed multiple two-port networks in series (see Figure 2.8). In particular, the T-parameters are intended to translate the incident and reflected waves at port 1 (a_1, b_1) to the incident and reflected wave at port 2 (a_2, b_2) as follows

$$\begin{bmatrix} a_1 \\ b_1 \end{bmatrix} = \begin{bmatrix} T_{11} & T_{12} \\ T_{21} & T_{22} \end{bmatrix} \begin{bmatrix} b_2 \\ a_2 \end{bmatrix}, \tag{2.7}$$

where T_{nn} indicates the entries of T-parameter matrix of the electrical network. The T-parameter matrix of a two-port network can be calculated in terms of S-parameters based on [64] as

$$\begin{bmatrix} T_{11} & T_{12} \\ T_{21} & T_{22} \end{bmatrix} = \begin{bmatrix} \dfrac{1}{S_{21}} & -\dfrac{S_{22}}{S_{21}} \\ \dfrac{S_{11}}{S_{21}} & \dfrac{S_{12}S_{21} - S_{11}S_{22}}{S_{21}} \end{bmatrix}. \tag{2.8}$$

Conversion to T-parameters allows describing multiple two-port networks cascaded in series as the product of their matrices. Hence, the T-parameters matrix of the cascaded network $\mathbf{T_C}$ can be obtained by multiplication of the T-parameter matrices $\mathbf{T_1}$ and $\mathbf{T_2}$ as follows

$$\mathbf{T_C} = \mathbf{T_1}\mathbf{T_2}. \tag{2.9}$$

In a similar manner, this approach can assist in removing the effect of a two-port network (redundant network) from a primary network. For this purpose, the primary two-port network is assumed to be a cascaded network consist of the redundant and desired networks. Consequently, the de-embedding can be performed by multiplying the

T-parameter matrix of the primary network $\mathbf{T_C}$ with the inverse of the redundant network $\mathbf{T_2^{-1}}$ as

$$\mathbf{T_1} = \mathbf{T_C}\mathbf{T_2^{-1}} \tag{2.10}$$

where $\mathbf{T_1}$ indicates the T-parameter matrix of the network after de-embedding. The T-parameter matrix obtained in this way can be readily converted back to the S-parameter matrix based on [64] as follows

$$\begin{bmatrix} S_{11} & S_{12} \\ S_{21} & S_{22} \end{bmatrix} = \begin{bmatrix} \frac{T_{12}}{T_{11}} & \frac{T_{11}T_{22} - T_{12}T_{21}}{T_{11}} \\ \frac{1}{T_{11}} & -\frac{T_{12}}{T_{11}} \end{bmatrix} \tag{2.11}$$

Although higher-order networks can be connected together by means of S-parameter in a similar approach as described in (2.6), the corresponding equation set becomes quite bulky and complex. In addition, using matrix multiplication in terms of T-parameters is only specified for two-port networks. Therefore, cascading and de-embedding in case of multi-port networks is done in a more general form by means of admittance parameters (Y-parameters). For instance, in order to connect a two-port network $\mathbf{Y_2}$ to port 3 of a three-port network $\mathbf{Y_1}$, first, a square zero matrix $\mathbf{Y}$ with adequate number of elements is initialized. The approach is shown in Figure 2.9. The original networks $\mathbf{Y_1}$ and $\mathbf{Y_2}$ act as subnetworks, whose elements are added to form the dataset representing the cascaded network. The resulting network still includes the effects of a redundant port, which should be eliminated from the data to ascertain the correct signal flow inside the network. The port elimination is carried out by converting the resulted Y-parameter matrix to a Z-parameter matrix and the subsequent removal of all element related to the redundant port from the Z-parameter matrix. This act is equal to leave the redundant port open. The remaining three-port matrix describes the desired cascaded network in terms of Z-parameter, which can be converted to other network parameters as described in [64].

Similarly, in order to de-embed a two-port network from a specified port of a three-port network, first, the two-port network is converted to the transfer chain representation (ABCD-parameter). The result is inverted subsequently, to achieve a dataset, which removes the effect of the frequency response of the redundant network from the three-port network. Following this, the matrix is converted back to Y-parameter and added to the three-port network in a similar manner as described for cascading.

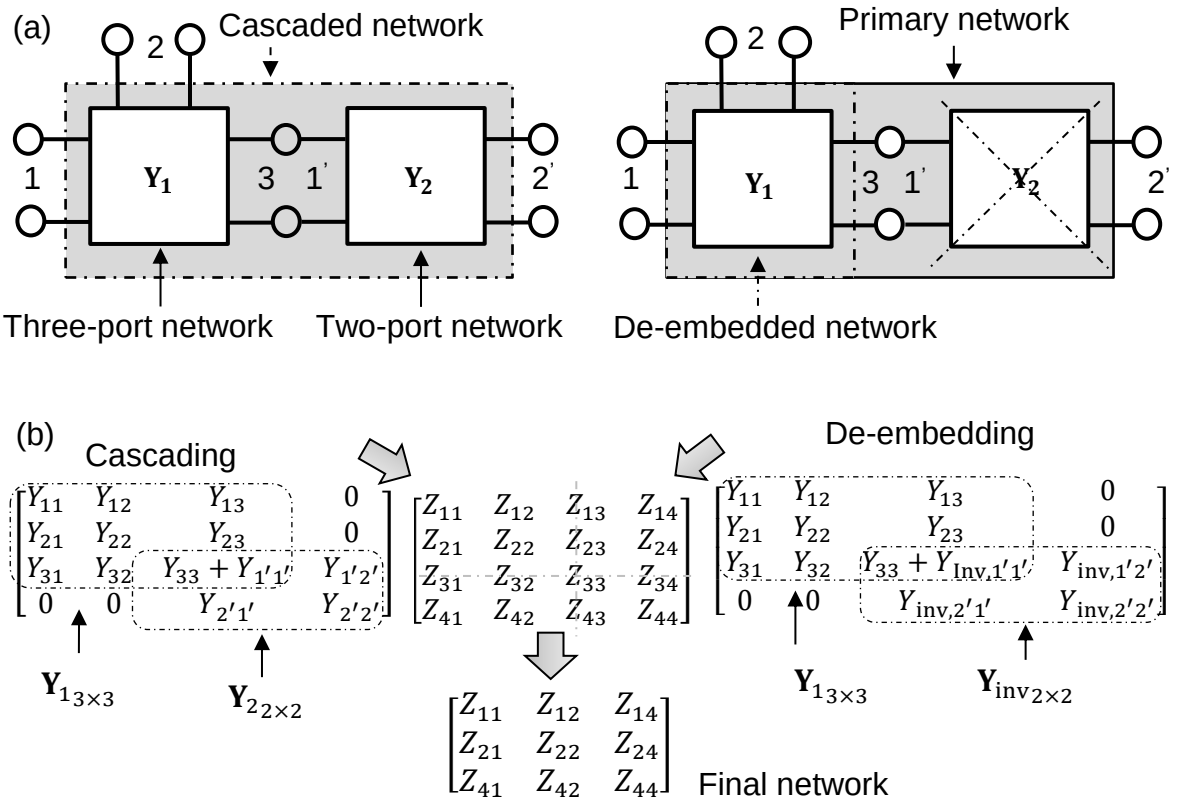

Figure 2.9: Cascading and de-embedding of a three-port network and a two-port network by means of Y-parameters (a), mathematical approach to cascade or de-embed an additional two-port network to a three-port network (b)

2.2.2 Extraction of RLCG Parameters

The dominant propagation mode on multiconductor transmission lines is the transverse electromagnetic (TEM) mode, where the electric and magnetic fields are only in the transverse plane orthogonal to the line axis [65]. Satisfaction of a TEM is the fundamental assumption in analysis of transmission lines. Despite the complex structure of a wiring harness (wire bundle) involved in measurement setup based on standard ISO 11452, signal propagation along wiring harness is commonly considered as TEM mode [6][7][9][11]. However, the inhomogeneity at wiring harness ends and the presence of injection and current probes invalidates the basic assumption of a TEM field structure through the entire wiring harness.

In order to tackle this issue and accelerate transmission line characterization, the wire bundle is replaced with a single wire and the wire over ground structure is considered as a cascaded network. The network consists of a homogenous segment at a distant location from metallic surfaces such as DUT, load simulator, test fixtures or other discontinuities along the wire and an inhomogeneous segment in proximity to those metallic surfaces. Figure 2.10 illustrates a single wire with length l located at a height $h = 5\,\mathrm{cm}$ over a ground plane. The homogenous and inhomogeneous segments are depicted in light green and dark green respectively.

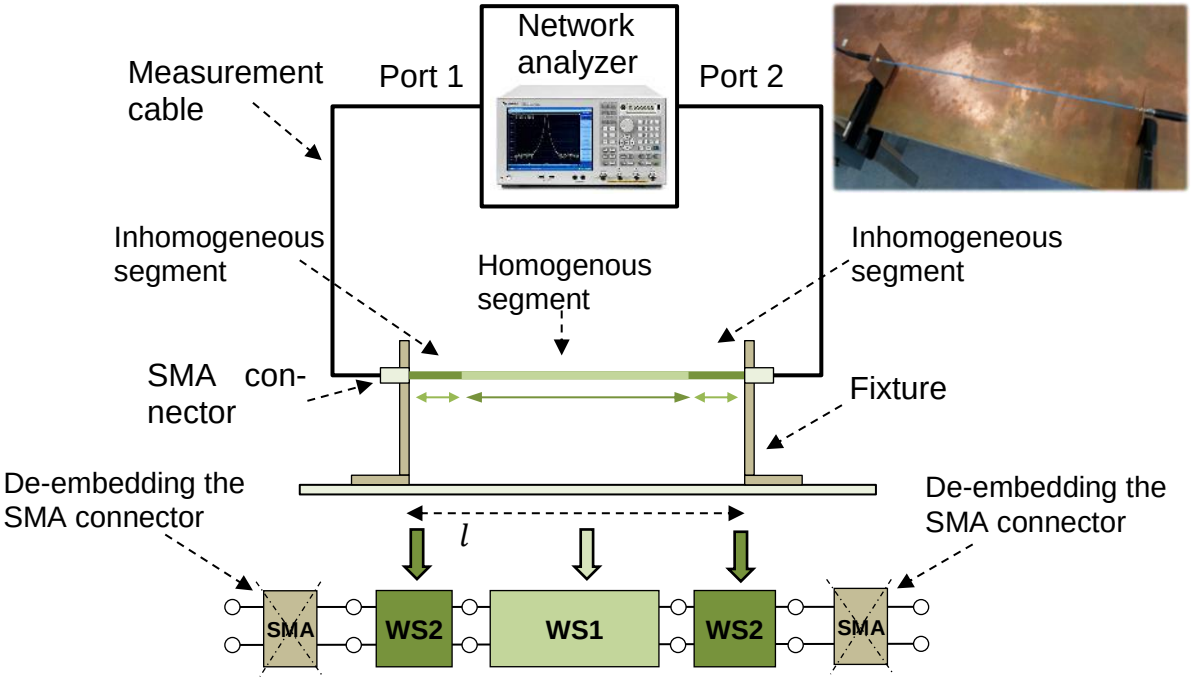

Figure 2.10: Characterization of a single wire over a ground plane with a VNA and the structure of the two-port networks for the homogenous and inhomogeneous segments according to the modelling scheme

According to [65] and [66], application of the per-unit-length (RLCG) parameterization of each segment proves to be an appropriate method, to describe the effect of transmission line with high accuracy and facilitate the de-embedding process required in the forthcoming sections. Several approaches for theoretical estimation [65-66] or measurement-based extraction of RLCG parameters exist [67-68]. In this work the parameter extraction introduced in [69] is applied, where the frequency dependent dielectric loss and conductor loss are taken into account. The parameter extraction approach introduced here for the special case of a single wire over a ground plane can be extended to MTLs in a similar manner as described in [69].

As described before, the transmission line considered in this section consists of a single straight wire spanned within two metal test fixtures. Two SMA connectors mounted on the test fixtures provide the access to the measurement instrument. According to [65], such passive structure can be characterized directly in terms of network scattering parameters. The two-port S-parameter is measured and recorded by means of a vector network analyzer (VNA) connected to the SMA connectors. First, the effect of SMA connectors is de-embedded from the raw S-parameter data. In order to obtain the transmission line parameters including the characteristic impedance and propagation constant, the S-parameter data is converted to chain parameters (ABCD-parameter). Initially, chain parameters link the voltage and current at one end of the line to the voltage and current at the other end of the line. However, the important advantage of chain parameters is that the characteristic impedance Z_c and the propagation constant γ appear directly in the matrix elements. This facilitates the estimation of transmission

line parameter from the measured data. In [65], the ABCD-matrix of a lossy transmission line in terms of hyperbolic functions are given as

$$\begin{bmatrix} A & B \\ C & D \end{bmatrix} = \begin{bmatrix} \cosh(\gamma l) & -Z_{\mathrm{c}}\sinh(\gamma l) \\ -\frac{1}{Z_{\mathrm{c}}}\sinh(\gamma l) & \cosh(\gamma l) \end{bmatrix}, \tag{2.12}$$

where l indicate the total length of the transmission line. Both Z_{c} and γ can be calculated straightforwardly by

$$Z_{\mathrm{c}} = \sqrt{\frac{B}{C}} \tag{2.13}$$

and

$$\gamma = \frac{1}{l}\operatorname{arccosh}(A). \tag{2.14}$$

Based on the definitions of Z_{c} and γ for a transmission line the corresponding frequency-dependent RLCG vectors can be determined [65]. In contrast to the L and C vectors, which demonstrate almost constant trends and provide good accuracy for a wide range of frequencies, the vector R shows a significant frequency dependency mainly due to the skin effect [65]. A good approximate expression of an element of the resistance vector at a certain frequency is given in [65][69] as

$$R(f) = R_0 + R_{\mathrm{S}} \cdot (1 + 1j) \cdot \sqrt{f}, \tag{2.15}$$

where R_0 and R_s indicate the DC resistance and the skin effect respectively. The imaginary term depicts the internal inductance. Additionally, an element of the conductance vector G is often approximated with

$$G(f) = G_0 + G_{\mathrm{D}}(1 + 1j) \cdot f, \tag{2.16}$$

where G_0 models the shunt current due to free electrons in imperfect dielectrics and G_{D} models the power loss due to the rotation of dipoles under the alternating field [69]. An ultimate goal is to extract all six parameters ($R_0, L_0, C_0, G_0, R_{\mathrm{S}}, G_{\mathrm{D}}$) from measurement results by data fitting. As described before, the influence of the fixtures cannot be neglected if high accuracy is required. The effect of the segment close to fixtures can be considered as a constant offset in the RLCG parameter values [75]. This offset is extracted by

1. calculating the RLCG vectors for the same type of wire with several lengths (here 23 cm, 51 cm, 150 cm),
2. fitting the frequency dependencies with simplified approximations based on (2.15) and (2.16),

3. linear extrapolation of the RLCG values to zero wire length.

This approach returns not only the per-unit-length parameters of the main homogenous segment but also gives an estimation for the virtual per-unit-length parameters of the inhomogeneous section close to the fixtures, where stray field effects are involved.

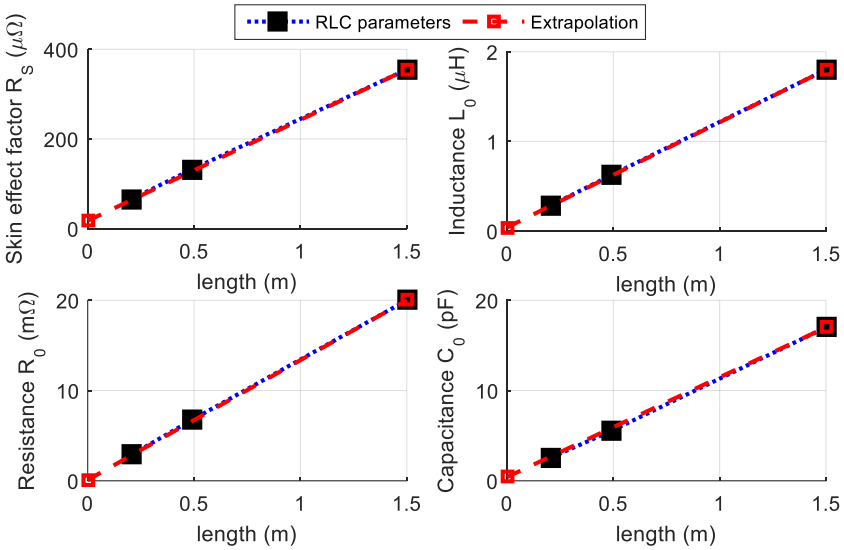

Figure 2.11: Extraction of the RLC parameters of the inhomogeneous segment by linear extrapolation of the RLC parameters of different wire lengths to the zero length

Furthermore, the effect of the SMA connectors of the test fixture is represented with a short lossless transmission line with characteristic impedance $Z_c = 50\ \Omega$ and the connectors time delay $T_D \approx 50\ \mathrm{ps}$. The effect can be de-embedded directly based on (2.10) from the raw S-parameter measurement results. The extraction of the RLC parameters of the inhomogeneous segment by linear extrapolation is shown in Figure 2.11. Table 2.3 shows the RLC parameters for both homogenous and inhomogeneous segments. The resistance, inductance, capacitance and skin effect values can be extracted with very high accuracy. However, the shunt conductance component (of air) lies outside the VNA dynamic impedance measurement range, and therefore, cannot be extracted accurately [75].

	$R_0(\mathrm{m\Omega})$	$R_s(\mathrm{m\Omega})$	$L_0(\mu\mathrm{H})$	$C_0(\mathrm{pF})$
Homogenous	9.6499	0.2411	11.898	10.425
Inhomogeneous	13.232	0.86515	20.092	20.128

Table 2.3: Extracted RLC values of the homogenous and inhomogeneous segments for the sample single wire over ground structure

In order to validate the proposed approach to estimate the behavior of the transmission line for various setup lengths, the S-parameters for a new setup with $l = 1\ \mathrm{m}$ are reconstructed with the extracted RLC parameters and compared to direct measurement data. The comparison between the magnitude and phase of the transmission line's S-parameters is illustrated in Figure 2.12. The results show that the S-parameters are

reconstructed with very high accuracy up to 1 GHz. However, to achieve a better accuracy especially at higher frequencies, more improved models to describe frequency-dependent parameters are required.

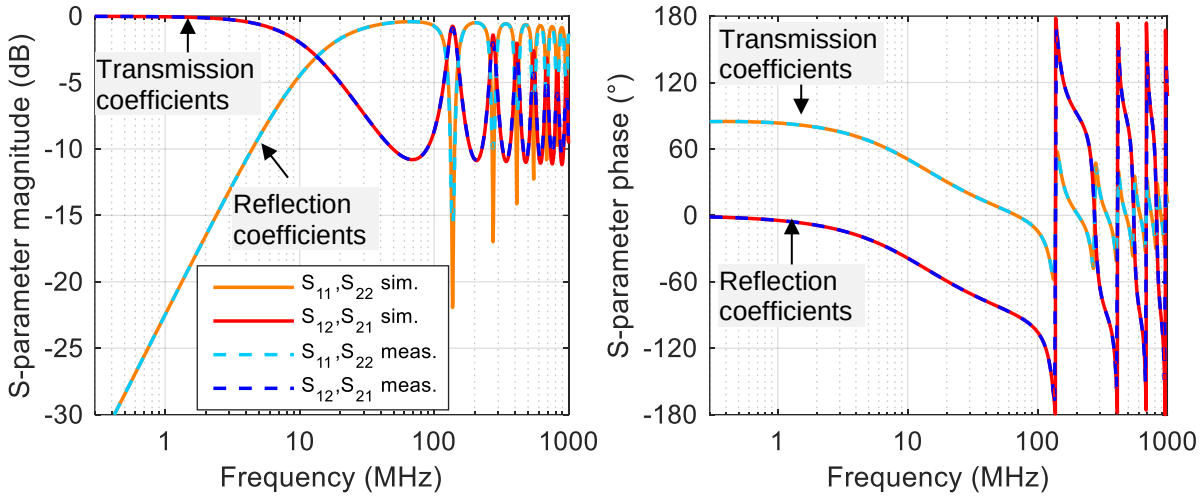

Figure 2.12: S-parameters of a single wire of length 1 m within fixtures, measurement and reconstruction based on the per-unit-length parameters

2.2.3 Modelling of BCI Coupling

As outlined earlier, BCI testing involves current injection to a DUT by means of a specifically designed current transformer (BCI probe) to assess the susceptibility thresholds up to 400 MHz. As shown in Section 2.1.2, although the exact procedure to calibrate the forward power to drive a specific amount of current into a 50 Ω load is prescribed in [2]ISO 11452 part 4, the actual current injected into a DUT during a BCI test is often significantly different. Depending on the characteristics of the test setup such as wiring harness parameters and impedance of the terminal units, the currents injected into a DUT varies from one test setup to another [11][36]. Therefore, obtaining an accurate model of the test setup will help not only to calculate the actual currents injected into the DUT and load simulator during BCI, but also to improve the correlation between ALSE and BCI in the last chapter of this work.

As described at the beginning of this chapter, the main goal in this section is to propose a measurement-based approach to model the BCI coupling, without considering the physical properties of the inner components in detail. As illustrated in Figure 2.13, a typical BCI probe consists of a single winding around a ferrite core, a metallic frame and an injection connector to connect to RF signal source [24].

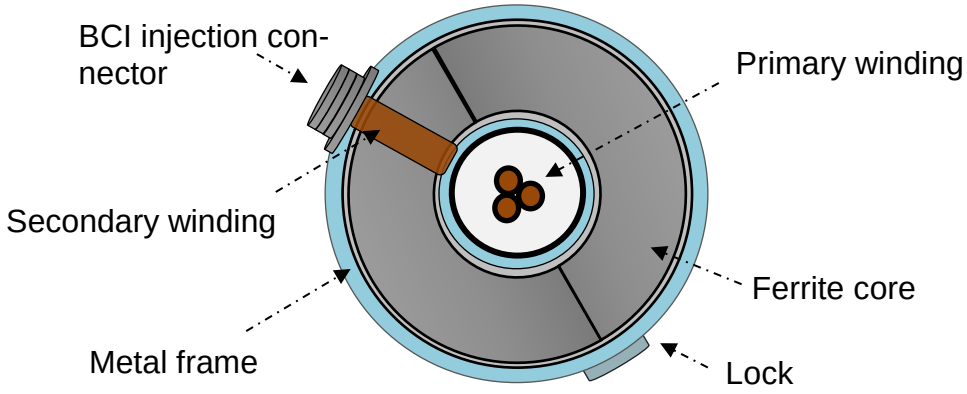

Figure 2.13: Internal structure of a sample BCI probe clamped around a wiring harness

In order to remain consistent in this work, the clamped wiring harness is considered as the primary winding and the conductor around the ferrite as the secondary winding. Based on this description, a low-frequency circuit interpretation of the BCI probe can be an ideal transformer [24]. In line with this, injection of RF interference can be modelled by lumped voltage source exciting each clamped wire. Moreover, the loading effect of the BCI probe on any clamped wire, due to the existence of the additional ferrite core, is described with an impedance in series with the lumped voltage source [24]. Although the application of this model is restricted to the lower frequency range due to the sole focus on inductive coupling, it provides a simple but highly effective tool to understand the coupling phenomenon. Additionally, this simplified model will be discussed in detail in Chapter 3 and 4 to derive simple expressions for impedance measurement with current transformer.

Most BCI probe models available in the literature assume that BCI probes behave as linear devices in the frequency interval of interest for immunity testing. In particular, the investigation in [38] indicates that no significant saturation phenomena occurs in the frequency interval as far as the forward power does not exceed the specified continuous wave (CW) power rating of the BCI probe. Hence, the BCI coupling to a wire bundle can be considered as a linear network and can be described in terms of S-parameters. As mentioned earlier, wire bundle is replaced with a single wire in this investigation. However, the same approach can be used for a wire bundle by preparing an appropriate test fixtures to expand the number of measurement ports based on number of conductors.

All investigations in this work concerning the BCI are done with a FCC F-140 BCI probe. Figure 2.14(a) shows the proposed setup to carry out a primary S-parameter measurement. The BCI probe is clamped around a single wire of the length $l = 50\ \mathrm{cm}$ spanned within two test fixtures at the height $h = 5\ \mathrm{cm}$ above the ground plane. Without the loss of generality, the same wire type and fixtures as in the previous section are used here.

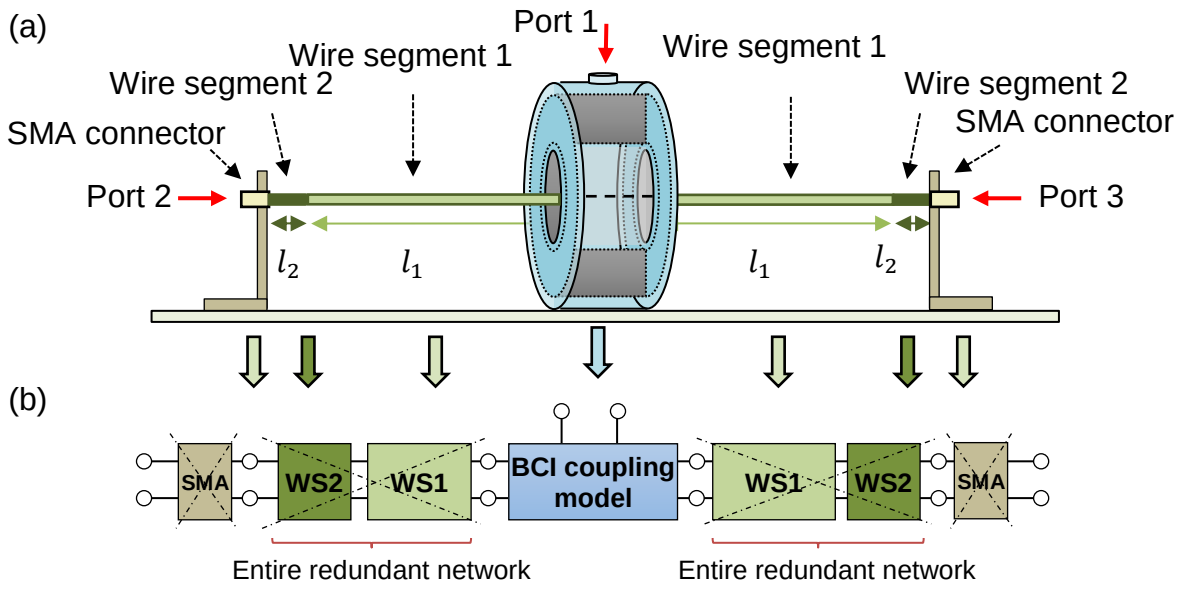

Figure 2.14: Structure of the setup to perform the primary three-port S-parameter measurement (a), de-embedding wire segment and SMA adaptors from the primary S-parameter measurement to extract the BCI coupling model

In order to perform the S-parameter measurement, a VNA Agilent E5071B, is connected to the available ports including the probe's connector port (port 1) and the test fixtures (port 2 and 3). The S-parameters are measured and recorded between 300 kHz and 1 GHz at a forward power of 0 dBm. The entire measurement structure is interpreted as seven separate networks including:

1. a three-port central network (BCI coupling network),
2. two two-port networks representing a wire segment of length 1 cm at each side close to the fixtures (inhomogeneous segment, WS 2),
3. two two-port networks representing a wire segment of 20.5 cm at each side (homogenous segment, WS 1),
4. two SMA connectors mounted on the fixtures between the calibration plane and the wire at each side (SMA).

In the beginning, the effects of the SMA connectors are removed from the raw measured data by de-embedding the corresponding phase shifts from port 2 and 3 as described in Section 2.2.1. The next step is to obtain the S-parameters of the redundant networks including the homogenous and inhomogeneous segments for de-embedding. For this purpose, the per-unit-length parameters extracted in the previous section are used to calculate the ABCD-parameters of each cable segment based on (2.12). Following this, the S-parameter can be readily calculated by converting ABCD-parameters based on [64]. The two-port S-parameters of the wire segments at each side are cascaded based on (2.9) to obtain a new two-port network, which represents the entire redundant network at each side.

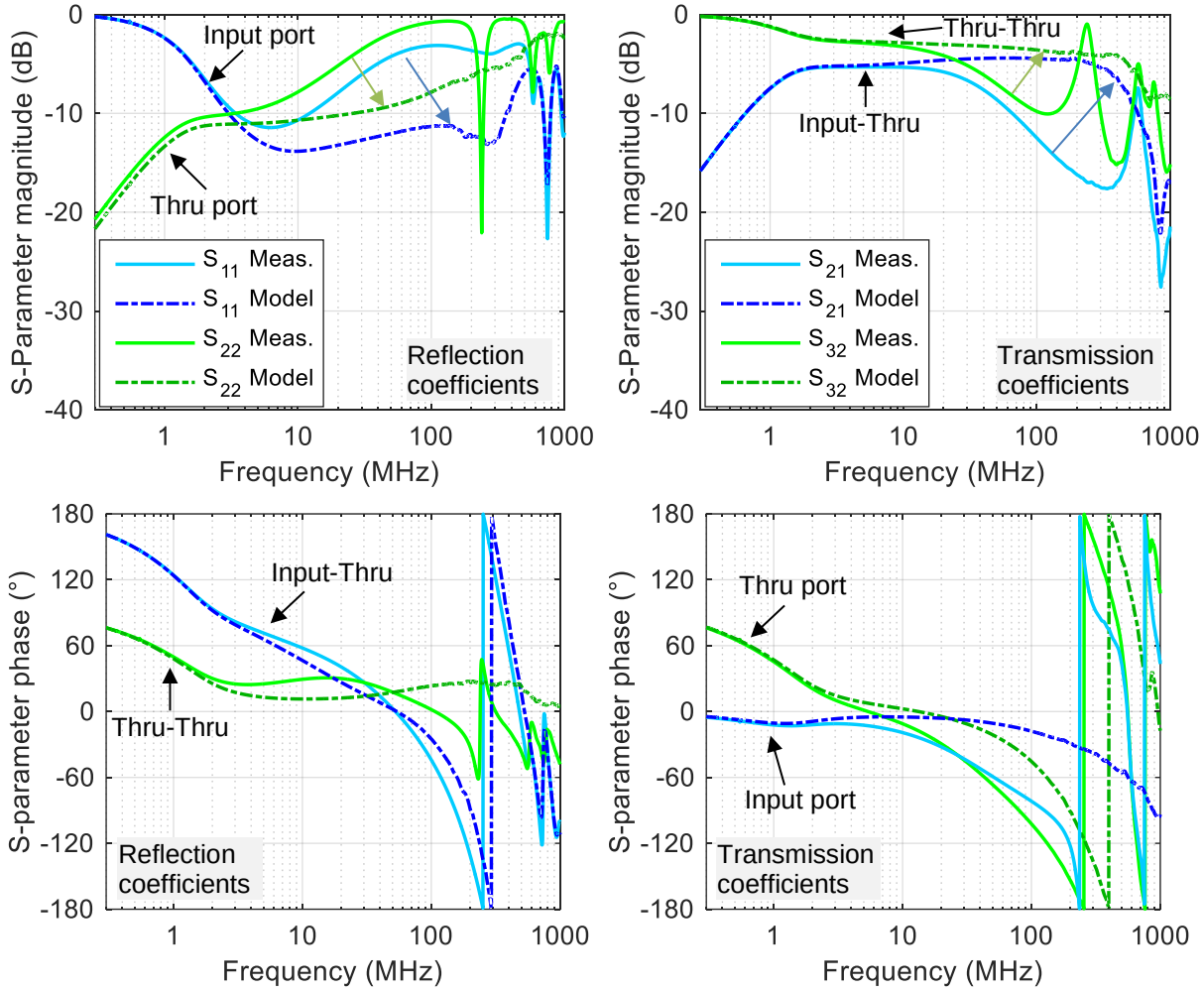

Figure 2.15: Comparison between the raw measured S-parameters during the primary measurement and the S-parameter model after de-embedding of the redundant data

Finally, each redundant two-port network is de-embedded from the three-port S-parameter as described in Section 2.2.1.The remaining three-port data belongs to the coupling of the BCI probe and the clamped wire.

The comparison between the sample coefficients of the primary three-port S-parameter and the three-port model are demonstrated in Figure 2.15. As can be seen, the de-embedding procedure has a significant impact on the magnitude and phase of the S-parameter coefficients. Moreover, the raw measured data could only be used as a coupling model at very low frequencies and the de-embedding must be carried out to obtain a reliable model for a BCI probe itself at higher frequencies. The explanation of different coefficients and their application to describe the internal structure of current transformers are given in Chapter 3.

The model is verified with a VNA measurement in a similar setup of larger length (here: 1 m). The coupling from RF-port at BCI probe to the fixture ports is measured in terms of S-parameters. The same setup is reconstructed by port-to-port cascaded connection of several involved modules.

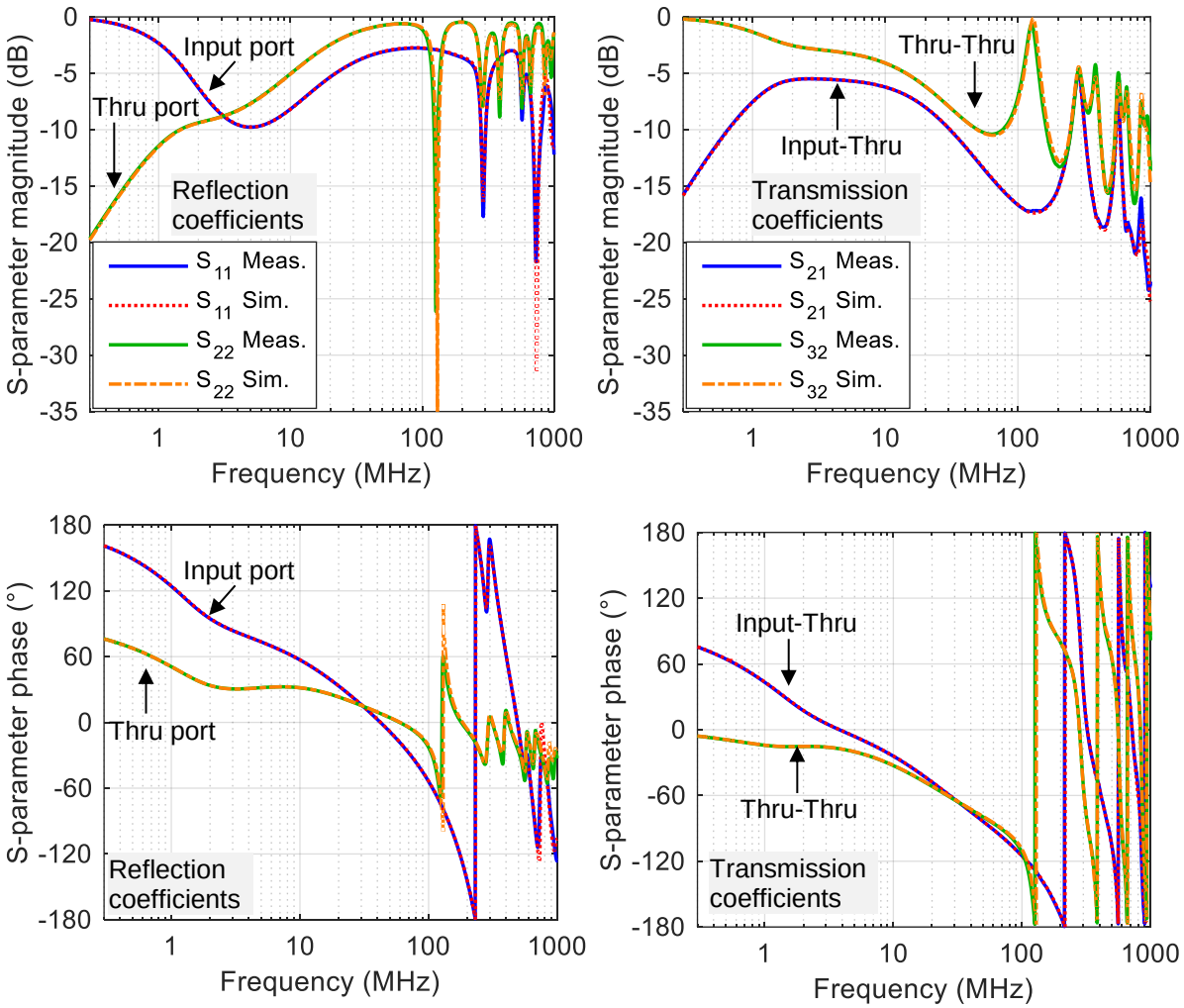

Figure 2.16: Comparison between the coefficients of the S-parameter matrix obtained from the direct measurement and simulated based on the three-port model

Since the BCI coupling dataset contains a side port (BCI probe's input port), which is not directly involved in the cascaded connection, the commonly used cascading procedure by matrix multiplication of the scattering chain parameters cannot be used. Hence, connecting the networks is performed in terms of Y-Parameters with an approach similar to one shown in Section 2.2.1. As demonstrated in Figure 2.16, the reconstructed signal transmission shows a very good agreement with the measurement data. The implemented approach foresees the application of an ad hoc calibration setup in order to simplify the complexity of a real BCI configuration while preserving acceptable coherence to the configurations recommended in ISO 11452. Appropriate design of test fixtures already characterized in Section 2.2.2 keeps the essential physical principles for the operation by resorting to simpler mechanical structures. Although the BCI model could be measured directly be reducing the length of the wire to 7 cm, the parasitic capacitive coupling between the test fixtures and the BCI reduce the accuracy at higher frequencies.

2.2.4 Modelling of Antenna Coupling

As described in Section 2.1.1, during an ALSE test, the DUT and the wiring harness are placed at a height $h = 5\,\mathrm{cm}$ above a reference ground plane. During the antenna testing or under normal operating conditions, the coupling of external fields with the wiring allows interference to reach the input ports of the DUT. Different approaches exist for describing the external coupling of an electromagnetic field to a line using transmission line theory for two-conductor lines and MTLs [12-15]. Each of these coupling formulations gives the same response for the transmission line if they are used properly [66].

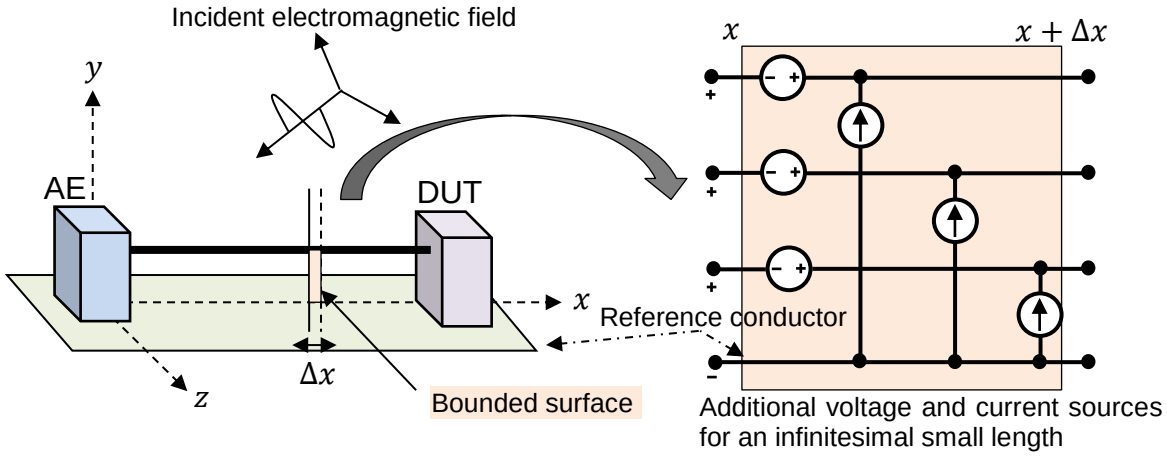

Figure 2.17: Per-unit-length equivalent sources for an infinitesimally small length of a MTL excited by an electromagnetic field as proposed in [65]

For example, a simplified test setup and the circuit interpretation of MTLs excited by an incident electromagnetic field based on [65] are illustrated in Figure 2.17. The proposed approach in [65] modifies the usual MTL equations by adding voltage and current sources defined for a surface bounded by each conductor and an infinitesimally small length between x and $x + \Delta x$. The equivalent sources are due to the normal component of the incident magnetic field and the transverse component of the incident electric field with respect to the bounded surface mentioned above. The idea behind this representation is that the incident field induces currents and charges on the conductors (wires). These induced currents and charges in turn produce a scattered field. The combination of the scattered field with the incident field, satisfy the boundary conditions on the surfaces of the line conductors. The general expression is commonly formulated in terms of the incident electric field using Faraday's law [65].

From the standpoint of immunity testing, the explicit solution for the line voltages and currents calculated based on terminal constraints (termination impedances) could be used to determine the interference level at the DUT and load simulator [65]. Nevertheless, the complexity of the real test scenarios and the existence of different parasitic effects in a non-ideal environment result in limited use of analytical approaches for

such purpose. Conversely, as mentioned earlier, the black box modelling based on S-parameter measurement appears to be a good solution to cover the entire internal structure and will be discussed hereafter.

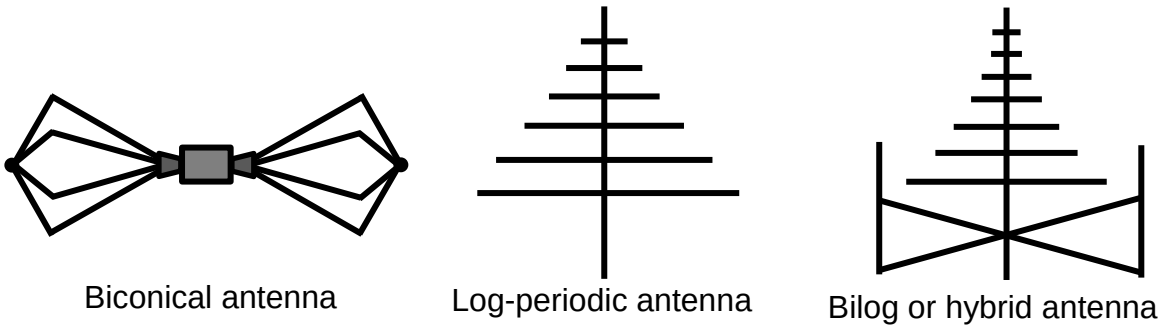

Figure 2.18: Typical antenna design used for EMC testing based on ISO 11452 part 2 up to 1 GHz

Basically, the black box model comprises the effect of the field generating device regardless of its structure and physical characteristics. However, a summary of the commonly used antennas can improve the understanding of the results achieved during an ALSE test. The typical antenna types used in radiated immunity testing based on ISO 11452 part 2 for covering different frequency ranges up to 1 GHz are:

- biconical antenna,
- log-periodic antenna,
- bilog or hybrid antenna.

As shown in Figure 2.18, biconical antenna is a broadband dipole consisting of two conical structures having common axis and vertex that are connected through the vertex to the signal generator. Log-periodic antenna usually consists of series of dipoles and has a geometry such that its impedance and characteristics repeats periodically as the logarithm of frequency [70]. For very high frequency purposes, horn antennas are commonly used. However, due to the upper limit of frequency range, they are not covered in this work. In accordance to ISO 11452 part 2, the biconical and the log-periodic antennas can be used to cover the complementary frequency ranges of 30 MHz to 300 MHz and 300 MHz to 1 GHz respectively. However, to perform any ALSE test with only one antenna, the so called bilog or hybrid antenna proves to be a good alternative [71-72]. Combination of the biconical and log periodic structures allows the bilog antenna to operate in a similar manner as biconical or log-periodic antennas over their relevant frequency range [73]. Therefore, in this section the bilog antenna Teseq CBL 6141 is chosen as the field generating device. A summary of geometrical dimension and technical specification of the antenna is given in Table 2.4. The CBL 6141 antenna radiates the field in a single direction, i.e. it is linearly polarized [73]. The imperfections, i.e. the cross polarization, are usually measured for the ratio of the field level in the intended direction to that of its orthogonal direction.

Frequency range	30 MHz to 2 GHz
Typical gain	4 dB (200 MHz to 1.5 GHz)
Impedance (nominal)	50 Ω
Average VSWR	2:1
Size antenna (L × H × W in mm)	approx. 1310 X 970 X 410

Table 2.4: Technical specification of Teseq CBL 6141B according to [73]

According to [73], the typical cross polarization for CBL 6141 varies between -35 dB and -21 dB for the frequencies over 200 MHz. Although [74] mandates a voltage standing wave ratio (VSWR) of less than 2:1 for receiver antenna systems, having a lower VSWR is also crucial during the immunity testing to minimize the power reflected from the antenna. This makes the best use of the ability of the employed power amplifier by requiring less power to generate a certain field strength. In general, high VSWR of broadband antennas, particularly at lower frequencies, means that much of the input power is reflected than radiated. In case of CBL 6141, the VSWR varies between 35:1 and 4:1 for the frequencies below 100 MHz. The high amount of the reflected power accounts for the poor efficiency at lower frequencies and may damage the power amplifier.

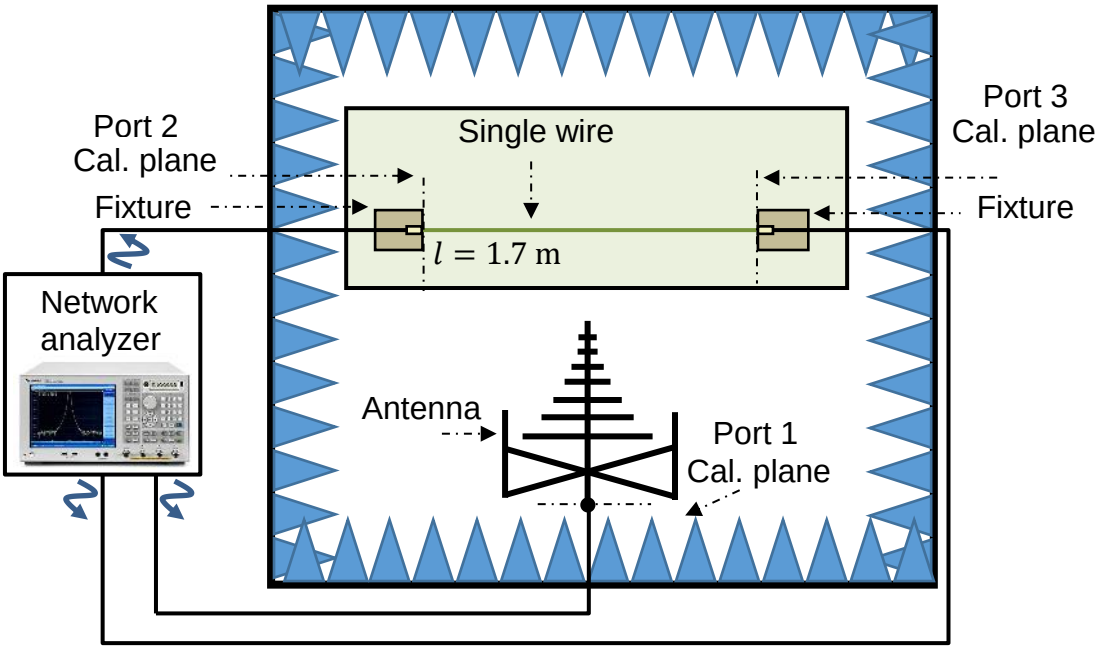

Figure 2.19: Setup for the measurement of the antenna coupling to a single wire in an anechoic chamber using a VNA and a bilog antenna

The measured three-port S-parameter magnitude and phase are illustrated in Figure 2.20 for both vertical and horizontal polarizations. In order to improve the transparency, the phase angles are unwrapped by avoiding absolute jumps between consecutive elements. Overall, the magnitude of the transmission coefficients increases over the frequency range, whereas the magnitude of the reflection coefficients declines.

Both of these observations confirm the poor efficiency of the antenna at lower frequencies. Although the measured reflection coefficients are almost identical, the transmission coefficients differ over the entire frequency range. The lower reflection coefficients at frequencies above 70 MHz corresponds to VSWR values given previously for CBL 6141 based on the antenna's datasheet. Moreover, while the magnitude of transmission coefficients of the horizontal polarization does not surpass -40 dB, the vertical polarization reaches its highest peak of -25 dB at 270 MHz.

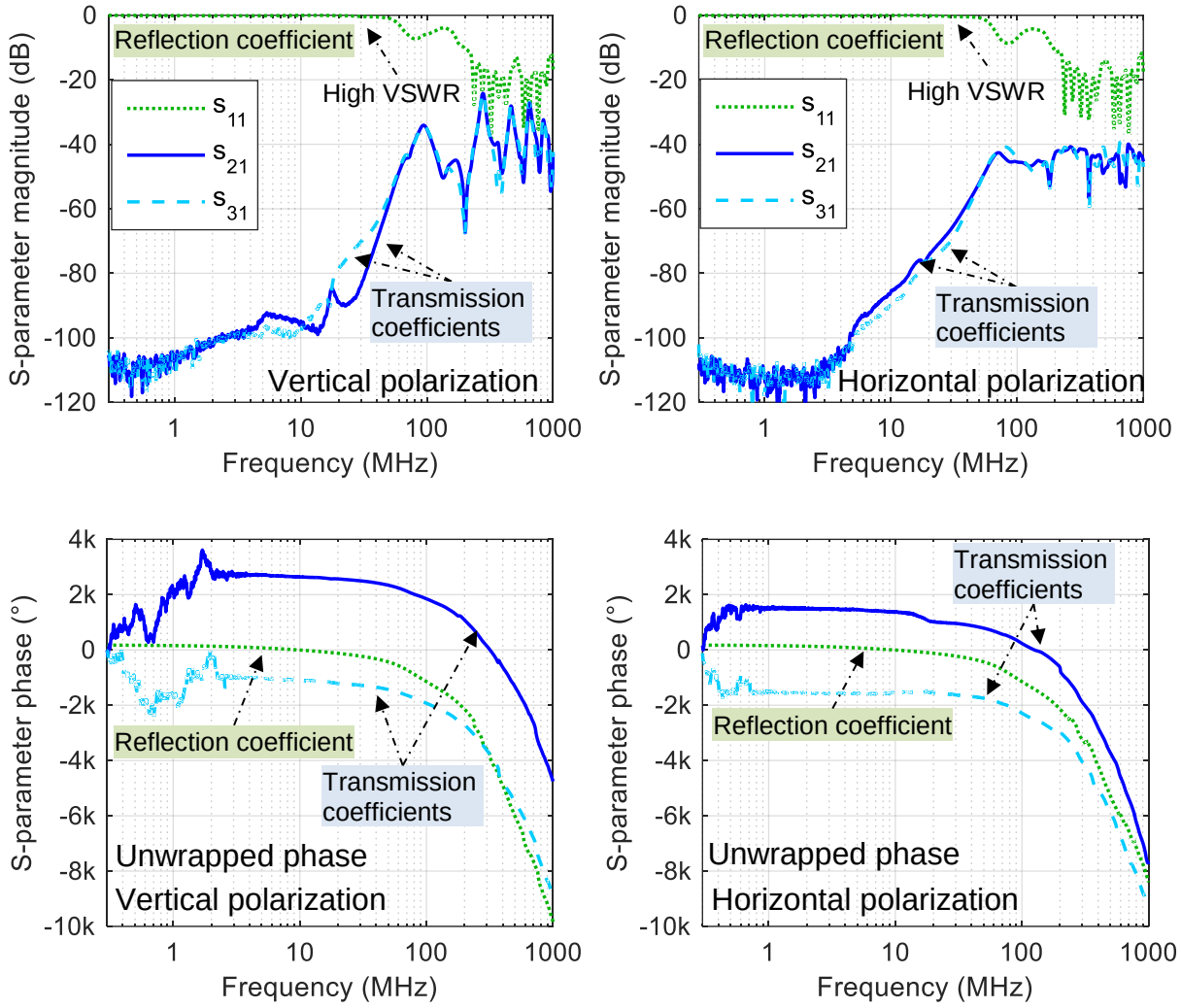

Figure 2.20: Three-port S-parameters (magnitude and phase) measured at vertical and horizontal polarizations, the phase is unwrapped to achieve better transparency

The considerable difference between both polarizations indicates that there is no unique ALSE coupling. Hence, each polarization should be considered separately, when it comes to compare BCI with ALSE. Despite the symmetric structure of the measurement setup and identical termination constraints, the magnitude of the transmission coefficients measured at port 2 and port 3 are not exactly the same. This points out the sensitivity of the ALSE method to very small changes or imperfections even under controlled conditions. Therefore, both magnitude and phase of the S-parameter coefficients are required to successfully connect other networks to the measured three-

port network and to calculate the interference levels at the input ports of termination networks.

2.3 Application and Experimental Results

Simple and accurate measurement-based methods to model the BCI and ALSE couplings were given in Section 2.2.3 and 2.2.4. In this section, the coupling models will be used to determine the RF currents coupled to the passive terminations in a setup based on ISO 11452. The simulated and measured RF currents (termination currents) are then compared for a specified signal power injected into the BCI probe or the antenna.

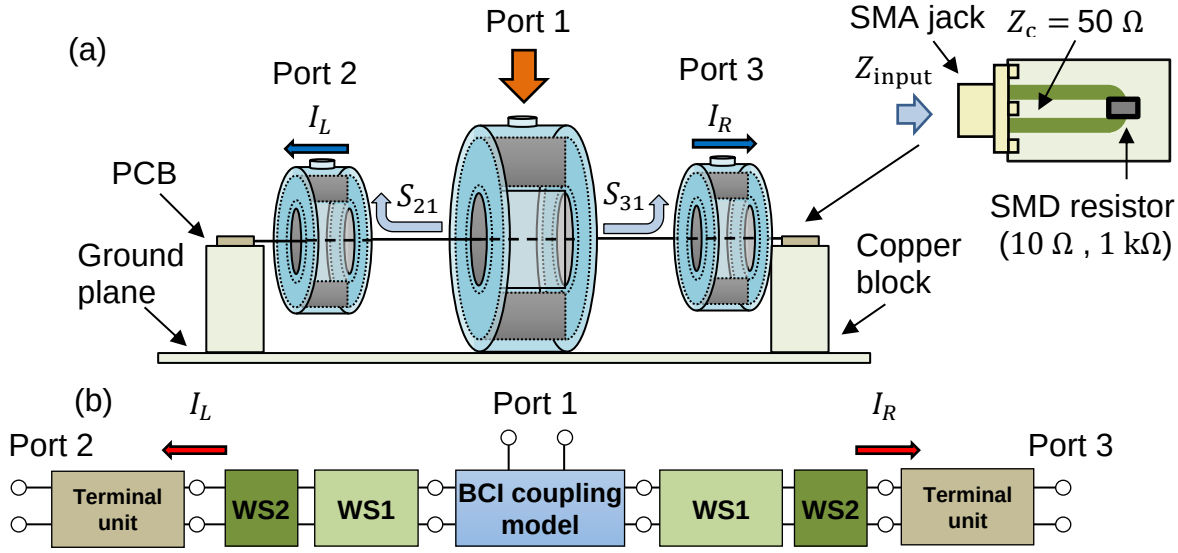

Figure 2.21: Direct measurement of the termination currents in a BCI setup and the structure of passive terminations (a), simulation of termination currents based on the BCI setup cascaded from the S-parameter models of individual setup components (b)

As illustrated in Figure 2.21(a), the terminal units include two small PCBs with only SMD resistors. Since the test setups often contain a low-impedance signal source and a high-impedance receiver, two SMD resistors of 10 Ω and 1 kΩ were selected. Both PCBs are placed upon two grounded copper blocks and connected directly to the wiring instead of the test fixtures. The termination impedance models are measured directly in terms of S-parameters by the VNA. For the purpose of model verification, a constant RF forward power of 10 dBm is injected into the input ports of the BCI probe and antenna with the VNA. The transmission coefficients are measured close to the termination PCBs by using two current probe FCC F-65 clamped around the wire. In order to the calculate the current phase correctly by means of a current probe, the phase information of the transfer impedance is required. Since the phase information is not usually given in the datasheets provided by manufactures, the complex transfer impedance must be extracted in a separate approach similar to the one given Section 3.2.3. The primary measurements are in terms of S-parameters. Hence, the measured transmission coefficients and the pre-characterized transfer impedance are required in

order to calculate the termination currents. In order to assess the capability of the models to estimate the termination currents, first, both BCI and ALSE setups are cascaded in Matlab from the S-parameters of the individual components as discussed in Section 2.2.1. The termination currents are then calculated for the given forward power level at the input port of the BCI probe or antenna.

2.3.1 Simulation of Termination Currents in BCI Setups

The structure of the BCI setup is shown in Figure 2.21(a). The probe is located in the middle of the setup. The PCB with 10 kΩ resistor and the PCB with 1 Ω terminate the left side and right side of the wire respectively. The BCI probe is connected to port 1. Port 2 and 3 are connected directly to the current probes. The transmission coefficients, S_{21} and S_{31}, are measured between 300 kHz and 1 GHz. The termination current at port 2 can be derived based on the definition of transmission coefficient S_{21} and transfer impedance Z_{T} with

$$I_{\mathrm{L}} = S_{21}\frac{\sqrt{P_{\mathrm{f}} \cdot 50\Omega}}{Z_{\mathrm{T}}}, \tag{2.17}$$

where P_{f} is the forward power injected into BCI probe and the impedance 50 Ω represents the equivalent port impedance of the VNA. The termination current at port 3 can be calculated based on (2.17) by substituting the transmission coefficient S_{21} with S_{31}. The direct measurement can also be performed by using a signal generator and a spectrum analyzer. On the other hand, to obtain a model for the entire setup and to calculate the termination currents, the individual S-parameter blocks extracted in Section 2.2.2 and 2.2.3 are cascaded according to Section 2.2.1. The final setup including the coupling model, homogenous and inhomogeneous wire segments and the passive terminations is shown in Figure 2.21(b). A straightforward method to determine the termination currents is to calculate the voltage at port 2 and 3 of the cascaded network in absence of 50 Ω port impedances. This can be done either by imposing the terminal constraints of an open-circuit into (2.4) or according to the approach proposed in [75]. In this method, the signal reflection of a new network $S_{11,\mathrm{open}}$ with open-circuit termination at port 2 and 3 can be calculated according to (2.4). Based on the predefined forward power P_f and the reference impedance Z_0, the current at the source port I_1 can be determined using

$$I_1 = \left(1 - S_{11,\mathrm{open}}\right)\sqrt{\frac{P_f}{Z_0}}. \tag{2.18}$$

The original three-port S-parameters are then converted to Z-parameters, which relate the voltages and currents at all ports together. Regardless of port 1, the current at other

ports are zero as a result of open-circuit termination. Therefore, the voltages at port 2 and 3 can be directly calculated using

$$V_{2,\text{open}} = Z_{21} I_1, \tag{2.19}$$

$$V_{3,\text{open}} = Z_{31} I_1. \tag{2.20}$$

Following this, the open-circuit voltage can be used to calculate the termination currents based on the pre-characterized termination impedances.

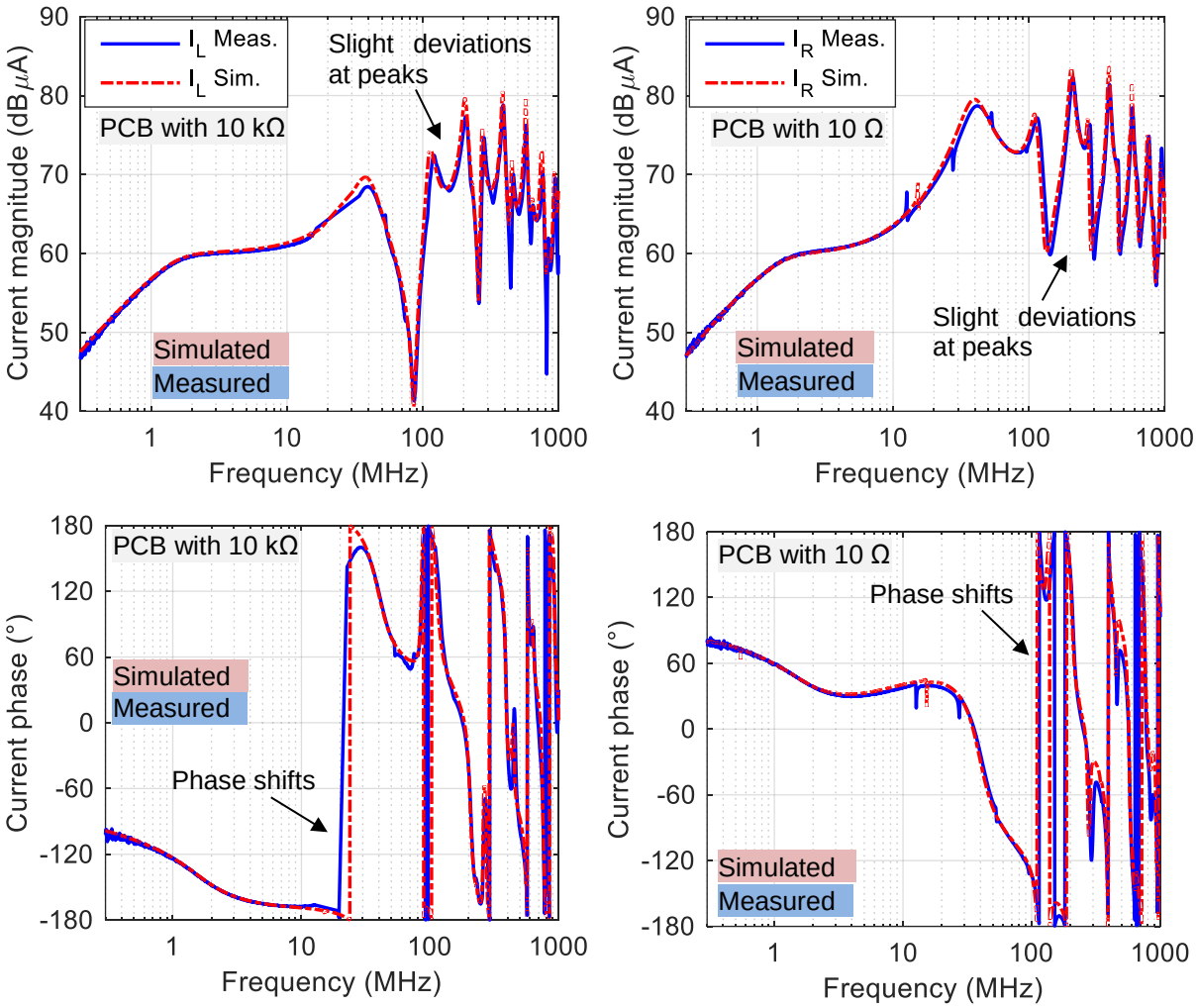

Figure 2.22: Comparison between the simulated and measured termination currents ($Z_\text{L} = 1\ \text{k}\Omega$, $Z_\text{R} = 10\ \Omega$) at an input forward power of 10 dBm

The comparative results between the measured and simulated termination currents are shown in Figure 2.22. Despite slight deviations at resonance frequencies, the results indicate a very good agreement even for the frequencies above 400 MHz for both termination networks. Additionally, as mentioned previously, the S-parameter models were primarily extracted by injecting a forward power of 0 dBm. However, to measure the termination currents, the input power is scaled up to 10 dBm. The high accuracy of the simulated results and the linearity of the setup concludes that the scaling of the power can be applied directly to determine the termination currents for other

input power levels as long as the terminal units are passive linear network. This conclusion will be used in the last chapter to accelerate the simulation of the BCI termination currents.

2.3.2 Simulation of Termination Currents in Antenna Setups

The structure of the ALSE setup for both vertical and horizontal polarization of the antenna is illustrated in Figure 2.23(a).

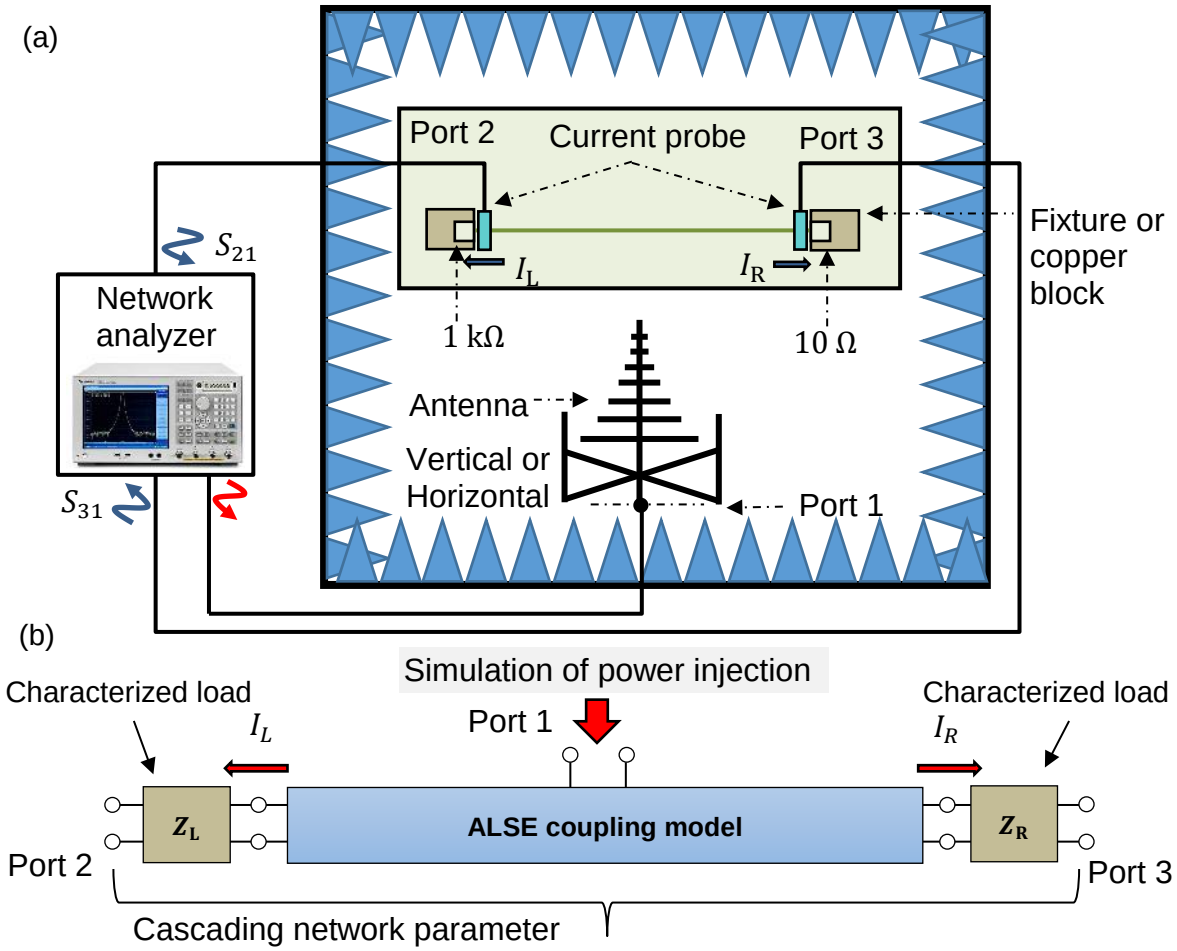

Figure 2.23: Direct measurement of the termination currents in an ALSE setup (a), simulation of termination currents based a setup cascaded from the ALSE coupling and termination networks

Similar to the BCI setup, port 1 is connected to the antenna and will be the signal source. Port 2 and 3 are connected to two current probes FCC F-65 located at the left side and right side of the wiring respectively. The structure of the wire and terminal unit remains unchanged. As described in the previous section, both transmission coefficients S_{21} and S_{31} are required to calculate the termination currents based on (2.17). In order to determine these coefficients, the entire networks including the three-port S-parameter coupling models of each antenna polarization and the characterized termination networks are cascaded. The new cascaded networks are then used to calculate the termination currents similar to Section 2.2.3.

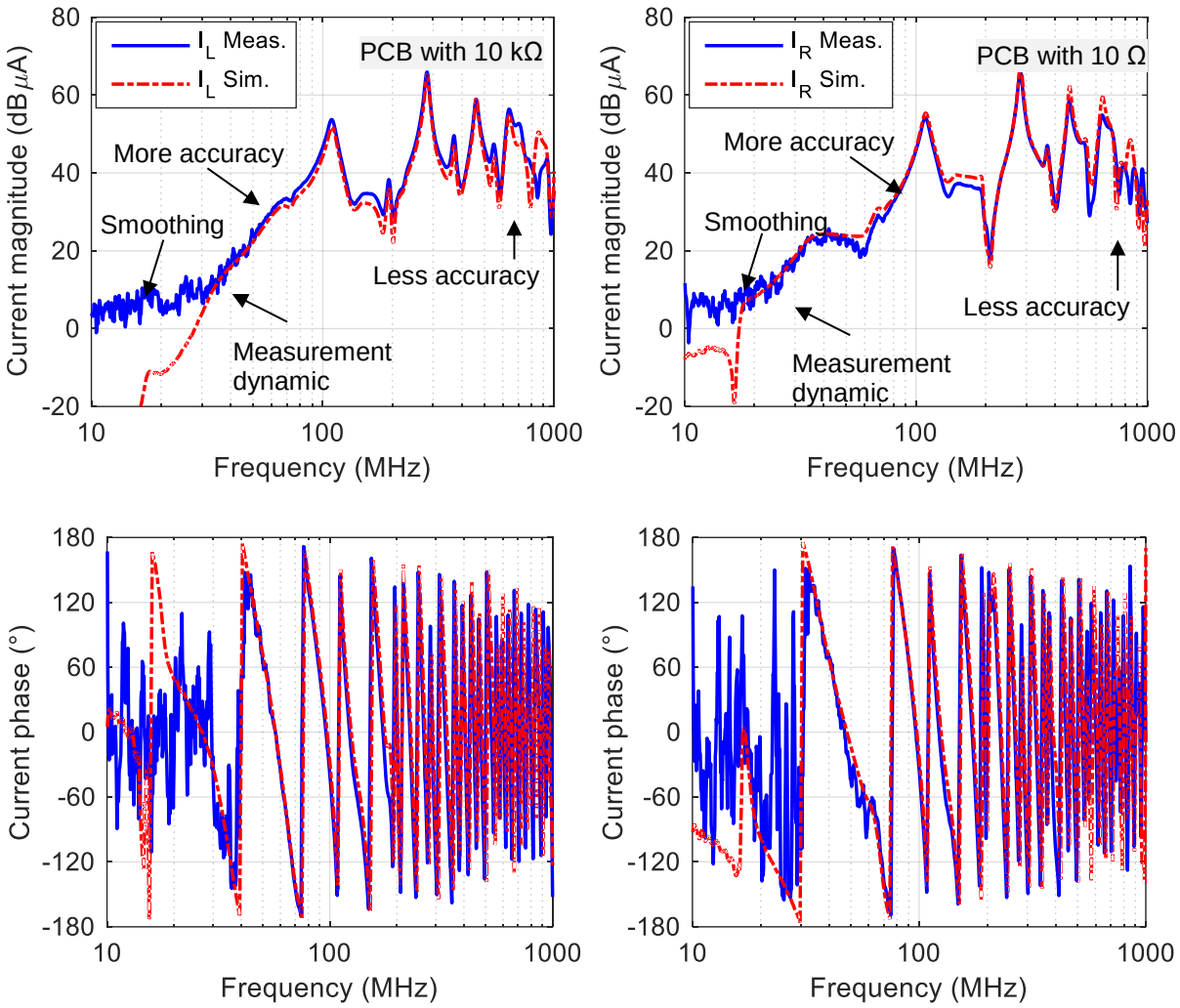

Figure 2.24: Comparison between the simulated and measured currents at the wire terminations ($Z_{\mathrm{L}} = 1\ \mathrm{k\Omega}, Z_{\mathrm{R}} = 10\ \Omega$) under the input forward power of 10 dBm for vertical polarization

Due to the difference between the components of the incident electromagnetic field, the procedure is carried out separately for each antenna polarization. However, the results are only shown for the magnitude and phase of the vertical polarization in the frequencies between 1 MHz and 1 GHz. A good congruence of the simulated and measured values can be observed for the frequency range up to 500 MHz in Figure 2.24. Similar to the BCI method, the S-parameter models were primarily extracted by injecting a forward power of 0 dBm. In order to determine the termination currents for the new forward power of 10 dBm, the termination currents are linearly scaled up. One important observation is the significant difference between directly measured and simulated results at very high frequencies in comparison to the BCI results. As described before, high sensitivity of the ALSE setup to small changes is the main reason for this behavior. Consequently, more care should be taken, when it comes to measuring or simulating the ALSE currents at frequencies above 500 MHz.

2.3.3 Virtual Calibration and Virtual Testing

In this section, the termination currents corresponding to BCI and ALSE realistic severity levels according to ISO-11452 are calculated using the developed models. For the BCI setup, first, the calibration setup network according to [2] is cascaded from the individual component in simulation environment. The virtual calibration setup consists of the BCI probe clamped around a wire of length $l = 10\ \mathrm{cm}$ connected between two test fixtures. Second, both ends of the virtual calibration setup are terminated with two ideal 50 Ω loads. Third, the termination currents I_{sim} for a forward power of 0 dBm (1 mW) are calculated using the procedure in Section 2.3.1. The forward power required to achieve 100 mA can be calculated with

$$P_{\mathrm{cal}} = 1\ \mathrm{mW} \cdot \left(\frac{100\ \mathrm{mA}}{I_{\mathrm{sim}}}\right)^2 . \tag{2.21}$$

In contrast, for the ALSE setup, the forward power necessary to reach the severity level of $100\ \mathrm{V/m}$ is measured directly with a field probe PMM EP-600. Alternatively, the datasheet of CBL 6141 gives only the forward power to obtain an electric field magnitude of $10\ \mathrm{V/m}$ in a distance of 3 m from the antenna. Although a simple prediction of the forward power to reach $100\ \mathrm{V/m}$ could be calculated by appropriate scaling of the electric field and distance to antenna, using the real calibration data proves to be more reliable and accurate.

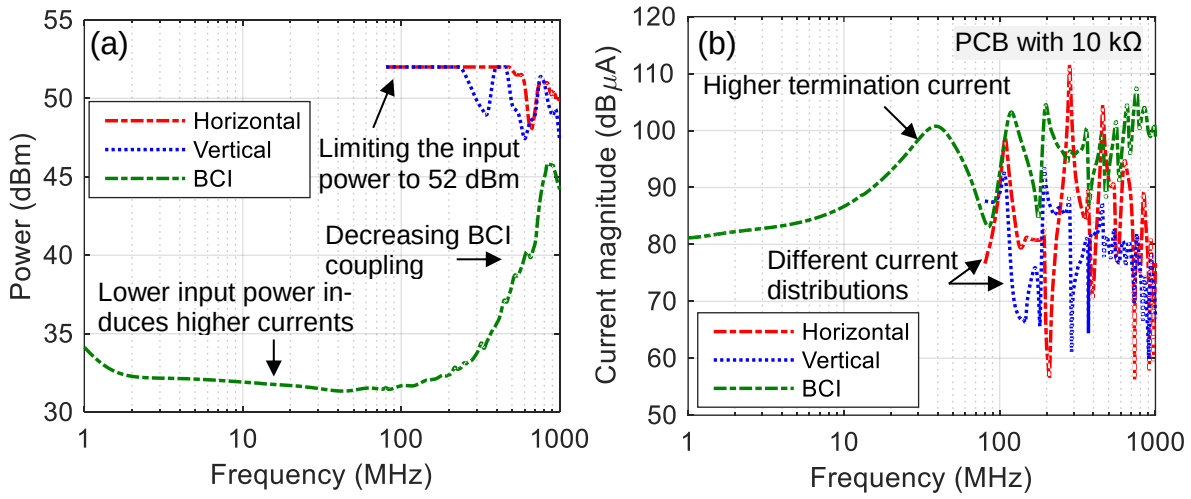

Figure 2.25: BCI calibration forward power determined by simulating the BCI calibration setup and ALSE calibration forward power measured directly in an anechoic chamber (a), termination current simulated under the calibrated forward powers (b)

Following the calibration procedure, the calibrated forward power is virtually injected into the BCI and ALSE setup models as described in Section 2.3.1 and 2.3.2. The calibrated forward power and the corresponding current at the low-impedance are shown in Figure 2.25. Based on the capability of the used power amplifier (Prana DT 150), the forward power is limited to 52 dBm. Due to strong inductive coupling between the BCI probe and wiring harness the amount of power injected into the input

port to reach 100 mA is much less than the injected power to reach the severity level of 100 V/m by ALSE. The different coupling mechanism of both procedures results in significantly different current patterns injected into both terminations for the calibrated RF input power level.

3 Characterization and Modelling of Current Transformers

Using toroidal current transformers (CT) in variety of EMC test procedures for injecting current into wiring harness as well as for monitoring current flow has gained a wide acceptance in automotive industry. In general, a simple CT consists of a primary winding, a magnetic core and a secondary winding. With respect to the immunity test setups in this work, the clamped wiring harness (test harness) and the winding around the core are considered as the primary and the secondary respectively.

From the technical standpoint, the optimal design of CTs demands high efforts and obligates the designers to employ complex techniques to achieve the best performance in a wide frequency range. However, from the user standpoint, CTs are predesigned for a certain purpose with a given figure of merit to characterize the performance. For example, injection probes and monitoring probes are mainly classified in terms of insertion loss and transfer impedance. The provided product descriptions or datasheets mostly give no information about the inner structure or the physical properties such as the core material and number of turns. For example, according to [76], the current probe FCC-F65 is only characterized in terms of its transfer impedance at a certain frequency range. Conversely, in case of magnetic cores, the provided datasheets contain a comprehensive description of material characteristics with respect to their application. The limited information in case of injection and current probes, particularly with regard to the immunity testing, has the disadvantage that the interaction of a CT with other components of an immunity test setup is unknown and the CT cannot be employed for any other purpose rather than the intended.

Additional built-in components in CTs due to the design considerations, characteristics of the core material such as core losses, and the existence of stray capacitances between different metallic structures introduce variety of side effects into test results [77-83]. For instance, at higher frequencies, the metallic body of commercial current transformers (CCT) introduces a heavy discontinuity along the wiring harness resulting in different propagation conditions compared to the case where the CT is absent. The identification and detailed examination of these interactions require an accurate model, which comprises both dominant and subordinate effects in the entire frequency of interest [84-85].

Furthermore, an accurate modelling of CTs allows for employing them in different applications such as measuring the impedance. As mentioned earlier, the term “indirect impedance measurement” is used in this work in respect of measuring the input impedance of DUT and load simulator under operation conditions with a CT. In the specific case of a single wire over a ground plane, the input impedance of a DUT (termination impedance) indicates the opposition that the DUT offers to the interference

signal generated by a BCI probe or an antenna. A simplified representation of an immunity test setup is shown in Figure 3.1. The term “termination node” is a virtual node defined to distinguish between the wire segment and the DUT input (DUT pin). This node represents the connection point between the wire end and the DUT pin. On this basis, the term “termination impedance” represents the input impedance between the termination node and the ground node. The same definition is used for the input impedance of load simulator. In case of wire bundles, where the wires are connected to the DUT with two or multiple pins, the input impedance between each termination node and the ground is considered as the DUT impedance.

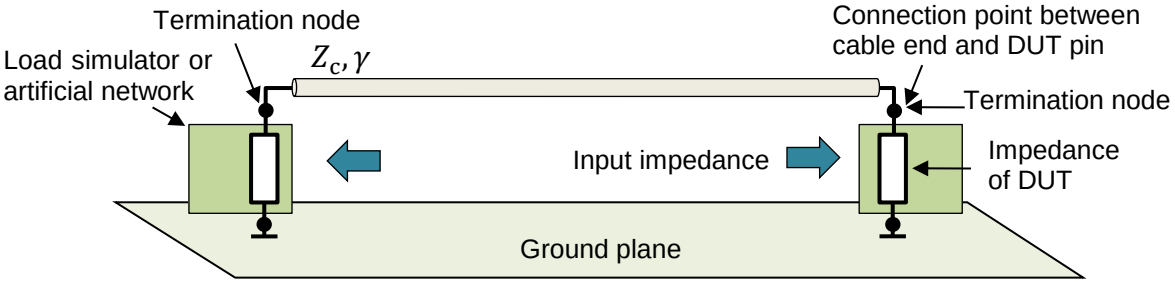

Figure 3.1: Simplified representation of an immunity test setup to clarify the terms and definitions used in this work regarding the termination impedances

The idea of using CTs to measure the impedance can be realized in different ways and will be discussed extensively in Chapter 4. Among the proposed implementation techniques in this work, using a CT directly as an impedance probe in combination with a VNA incorporates the very basic idea that can be put into effect with the least effort. As mentioned previously, the term “loop impedance” is used in this work to indicate the impedance attached to the primary winding of a CT. Assuming a VNA to be connected to the secondary winding, the term “impedance probe” describes a CT that is used to determine the loop impedance. However, concerning a CT clamped around a wiring harness in an immunity test setup, the loop impedance can be interpreted from another perspective. According to transmission line theory, the loop impedance at any point along the wiring harness in an immunity test setup can be considered as the accumulated transformed impedance of terminal unit at both harness ends, i.e. DUT and load simulator (see Section 4.1 for details). Thus, having knowledge of the loop impedance is the first step to relate the measured reflection data with a VNA to the impedance of terminal unit. However, the reflection data is significantly affected by the CT’s frequency response, which must be removed from the measurement by an appropriate de-embedding procedure.

To sum up, two objectives are chosen for this chapter. The primary objective is to show the capability of the measurement-based modelling to illustrate different transformation phenomena in CTs up to 1 GHz. The secondary objective is to use these

models to assess the possibility of combining a CT and a VNA for the purpose of indirect impedance measurement. Therefore, in this chapter, first, the operation of CTs is described based on Maxwell's equations. According to an improved equivalent circuit, the transformation characteristics of a generic CT are analyzed. For this purpose, the mathematical expressions for different figures of merit, including output impedance, insertion impedance and transfer impedance, are derived. These mathematical expressions are then used to predict and interpret different behavior of these impedances at low and high frequencies. In Section 3.2, similar to the previous chapter, the three-port network model for different CTs are extracted from the S-parameter measurements. Following this, the models are used to determine the output impedance, insertion impedance and the transfer impedance. Moreover, the models are used to compare the characteristics of sample commercial current transformers (CCT) and self-made current transformers (SCT) optimized for impedance measurement. Finally, in Section 3.3, the idea of using a CT as an impedance probe is analyzed using the extracted three-port network models. The complexities and limitations of measuring loop impedance in combination with a VNA and the subsequent de-embedding are investigated. Based on a brute force sensitivity analysis, several indications on the practicability, strengths and weaknesses of using different CTs for indirect impedance measurement are given and discussed.

3.1 Description of Transformer Operation

In general, according to [76] and [86], the design of CCTs is commonly a function of different parameters including:

- dimension of the wiring harness,
- operational bandwidth,
- maximum current rating,
- sensitivity (for monitoring probes),
- continuous wave (CW) power rating and effectiveness to deliver the amplifier forward power to the wiring harness (for injection probes).

Moreover, the structure commonly offers the clamp-on function of the probe and is enclosed in a metallic shield to prevent capacitive coupling. Despite a broad variety of possible realization schemes, the internal structure of a sample CT as proposed in [87] for the purpose of current measurement and its main components are illustrated in Figure 3.2. The structure is further simplified in this section to facilitate an in-depth analysis of the physical aspects.

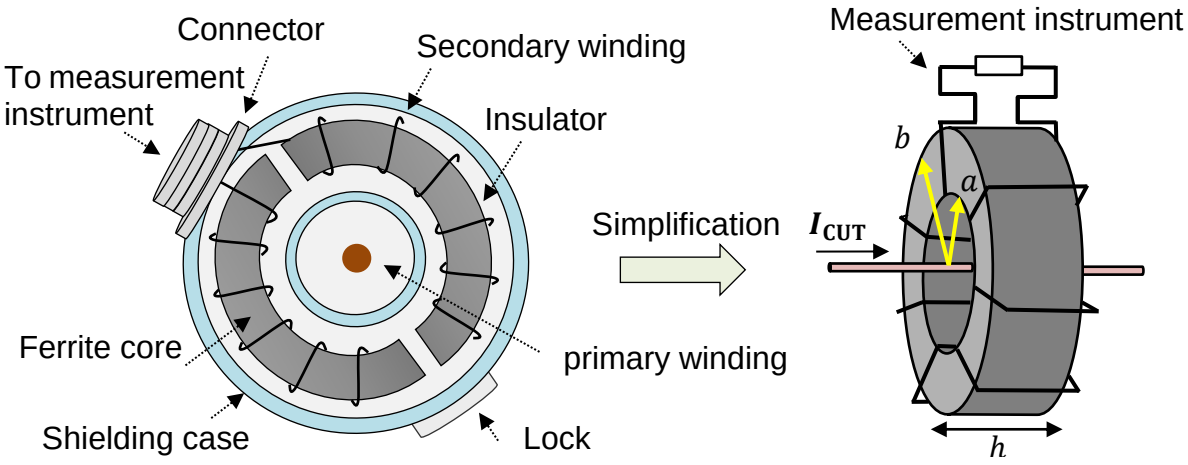

Figure 3.2: Internal structure of a typical CCT designed to measure the current in EMC applications [74] and the simplification of the structure to facilitate the analysis

3.1.1 Theoretical Background

According to Maxwell–Ampère equation, the relation between the altering current flowing in the primary and the created magnetic field strength $\mathbf{H}$ can be described by

$$\nabla \times \mathbf{H} = \mathbf{J} + \frac{\partial \mathbf{D}}{\partial \mathbf{t}} \xrightarrow{\text{LF approx.}} \nabla \times \mathbf{H} = \mathbf{J}, \tag{3.1}$$

where $\mathbf{D}$ is the electric displacement field and $\mathbf{J}$ is the current density. The effect of the derivative of $\mathbf{D}$ with respect to time can be ignored for low frequencies to simplify the approximation primarily [77]. The resulting time-varying magnetic field strength $\mathbf{H}$ is related to the time-varying magnetic flux density $\mathbf{B}$ by

$$\mathbf{B} = \mu \mathbf{H}, \tag{3.2}$$

where μ represents the permeability of the inner side of the secondary winding. From another point of view, according to Maxwell–Faraday equation, a time-varying magnetic flux density always accompany an electric field

$$\nabla \times \mathbf{E} = -\frac{\partial \mathbf{B}}{\partial t}. \tag{3.3}$$

Furthermore, the magnetic flux Φ through a cross sectional area of the secondary winding $\mathbf{A}$ is equal to the surface integral of the normal component of the magnetic field density $\mathbf{B}$ passing through that surface and can be formulated by means of a scalar product as follows

$$\Phi = \iint_A \mathbf{B} \cdot d\mathbf{A} \tag{3.4}$$

where $d\mathbf{A}$ indicates an infinitesimal area element of the surface. The electromotive force $\mathcal{E}$, i.e. the voltage between the terminals of the secondary winding, can be related to the magnetic flux by applying the Kelvin-Stokes theorem. In this way, the integral of the curl of the electric field over the cross sectional area can be related to the line integral of the electric field around the boundary of cross sectional area $\boldsymbol{l}$ with

$$\mathcal{E} = \oint_{l} \mathbf{E} \cdot d\boldsymbol{l} \xrightarrow{\text{Kelvin–Stokes theorem}} \mathcal{E} = \iint_{A} \nabla \times \mathbf{E} \cdot d\mathbf{A} = -\iint_{A} \frac{\partial \mathbf{B}}{\partial t} \cdot d\mathbf{A} = -\frac{\partial \Phi}{\partial t}. \quad (3.5)$$

The negative sign indicates that the induced voltage and the change in magnetic flux have opposite signs. This means that the variation of magnetic flux through the surface, bounded by the secondary winding induces an electromotive force whose value is determined by the rate of change of the magnetic flux. The resulted electromagnetic force creates a current in the secondary.

In general, the impact of the magnetic flux on the circuit in which the current is changing is called self inductance. Similarly, the impact of the magnetic flux on an adjacent circuit is called mutual inductance. Both of these parameters can be derived for a CT based on size, shape and core material. For example, in case of a toroid with a square cross section, N turns at the secondary and a single turn at primary, the self and mutual inductance can be derived from Ampère's circuital law given in (3.1). Assuming an inner radius a, outer radius b and the cross sectional radius h, the magnetic field density at radius r for any closed path l is given by applying the integral form of (3.1) as

$$\oint_{l} \mathbf{B} \cdot d\boldsymbol{l} = \mu NI \Rightarrow \mathbf{B} = \frac{\mu NI}{2\pi r} \mathbf{e}_{\boldsymbol{\varphi}}. \quad (3.6)$$

The direction of the vector $\mathbf{B}$ is tangential to the closed path and is given by the unit vector $\mathbf{e}_{\boldsymbol{\varphi}}$. According to (3.4), the magnetic flux through one turn of the toroid can be obtained by integrating over the rectangular cross section with $d\mathbf{A} = h\,\mathrm{d}r\,\mathbf{e}_{\boldsymbol{\varphi}}$ as the differential area element

$$\Phi = \int_{a}^{b} \left(\frac{\mu NI}{2\pi r} \mathbf{e}_{\boldsymbol{\varphi}}\right) h\, dr\, \mathbf{e}_{\boldsymbol{\varphi}} = \frac{\mu NhI}{2\pi} \ln\left(\frac{b}{a}\right). \quad (3.7)$$

Hence, the self inductance is derived by dividing the total magnetic flux by the current as

$$L_{\mathrm{ss}} = \frac{N\,\Phi}{I} = \frac{\mu N^2 h}{2\pi} \ln\left(\frac{b}{a}\right). \quad (3.8)$$

The inductance of the other winding, i.e. the clamped conductor, can be derived similarly by correcting the number of turns. In order to derive the mutual inductance, the amount of magnetic flux from the circuit in which the current is changing is required. Assuming an ideal coupling, the derived magnetic flux in (3.7) remains unchanged and can be used directly to derive the mutual inductance as follows

$$M = \frac{\Phi}{I} = \frac{\mu N h}{2\pi} \ln\left(\frac{b}{a}\right). \tag{3.9}$$

Comparing equations (3.8) and (3.9) reveals that

$$M = \frac{L_{ss}}{N}. \tag{3.10}$$

This expression indicates that the mutual inductance is inversely proportional to the number of turns. Despite crude representation of ideal transformers, the results incorporate useful approximations, if the geometrical dimensions and relative magnetic permeability of the core are known. Two other effects that are involved in the operation of a CT are leakage inductance and winding capacitance. In general, CT designs at higher frequencies, requires considerably more care in specifying the winding specification. For instance, the physical orientation and spacing of the windings affect the leakage inductance and winding capacitance. Although leakage inductance and winding capacitance are actually distributed throughout the winding in a CT, they are commonly considered as lumped elements [78]. The effect of winding capacitance is considered in this thesis with C_p and C_s for the primary and secondary windings and the effect of leakage inductance is incorporated with coupling factor k. Both of these effects will be discussed later in this chapter.

As given in (3.2), the permeability μ is the ratio of magnetic field density $\mathbf{B}$, to the applied magnetic field H. Regardless of the shape and size of the applied core, a detailed information about the permeability of the core material is required to illustrate the CT properties. For this purpose, the relative permeability μ_r is specified as the ratio of the permeability of a specific medium to the permeability of free space μ_0 [77]. In order to improve the comparison of magnetic materials and their frequency characteristic especially at higher frequencies the complex permeability is defined as

$$\mu = \mu' - j\mu'' = \mu_0(\mu_r' - j\mu_r''), \tag{3.11}$$

where the real part μ' represents the energy storage and the imaginary part μ'' represents the energy dissipation or losses. Both of these highly frequency dependent parameters are measurable and often provided by the manufacturer of the core material. The selection of μ' and μ'' depends on application.

3.1.2 Core Losses

An ideal CT is typically assumed as a transformer with no losses, i.e. the windings are purely inductive with no leakage inductance and the core is loss free [77]. However, in reality, core losses play a crucial role in understanding and interpreting the behavior of CTs [77-80]. Basically, core losses originate in different sources including hysteresis losses, eddy current losses, residual losses [77-79]. The hysteresis loss is the result of the irreversible rotation of magnetization vector due to the microscopic structure of the core material. The eddy current loss is due to the conductivity of the core material while experiencing an altering magnetic field and is a function of frequency. The residual loss is the main contribution to the dissipation of ferrites at lower frequencies resulting from the excitation of the uniform spin precession in ferrite and domain wall damping within ferrites [77-79]. In order to describe the loss phenomena in this work the term “core losses” is used to comprise the various types of losses that occur in ferrites. The general drawback of such lumped-parameter description strategy is that the different components involved in loss phenomena cannot be separated. However, as the aim of the research was not to analyze the detailed characteristics of magnetic cores, the lumped-parameter model proves to be a very useful approach to describe the loss phenomena.

As mentioned above, the behavior of a CT is strongly related to the core material and the core geometry. According to Section 3.1.1 a good figure of merit to compare different core characteristics is the complex relative permeability of the material. For example, generally, soft ferrite materials such as Manganese-Zinc ferrite (MnZn) and Nickel-Zinc ferrite (NiZn) demonstrate a high real part μ' and a low imaginary part μ'' [77]. This characteristic account for a stronger magnetic field density inside the core and less core losses. An important consequence of using soft ferrites as the core material is the higher magnetic flux between windings and hence, can be considered as a criterion for a good inductive coupling [77]. Moreover, in case of toroidal core shapes, the continuous magnetic path tangential to the core’s surface yields the lowest flux leakage. This means that a better transformation behavior can be achieved by combining a toroidal-shaped core with appropriate material characteristic, i.e. high storage term μ' and low energy dissipation term μ''.

3.1.3 Improving the Idealized Model

Understanding a CT operation can be made easier by using a lumped equivalent circuit model. According to [77], for an ideal CT the impedance transformed from the primary terminals to the secondary side is given by

$$Z_{\mathrm{out}} = \left(\frac{N_{\mathrm{s}}}{N_{\mathrm{p}}}\right)^2 Z_{\mathrm{loop}} \xrightarrow{N_{\mathrm{s}}=N_{\mathrm{p}}=1} Z_{\mathrm{out}} = Z_{\mathrm{loop}}, \tag{3.12}$$

where Z_{loop} is the impedance connected to the primary terminals (loop impedance) and N_{p} and N_{s} are the number of turns of the primary and secondary. Although simplified, (3.12) demonstrates the apparent impedance available at the secondary side due to the transformation act by any ideal CT. However, an improved lumped parameter circuit describing the CT's operation differs considerably from an ideal CT. Based on the investigations in [81-85] and the level of complexity in this work, the lumped parameter model illustrated in Figure 3.2 is chosen as a trade-off to describe the fundamental aspects of transformation phenomena. The model comprises all essential components such as self inductance of the primary and secondary windings, L_{pp} and L_{ss}, and the mutual inductance M to provide an acceptable approximation for the operation of a CT. The impact of the measurement device, additional elements and losses are given in terms of the representative resistors, which will be described hereafter. The circuit will be used during this chapter to interpret the behavior and derive mathematical expressions for different transformation aspects.

In general, the transformation equations can be described by using Kirchhoff's voltage law (KVL) at each side with

$$V_{\mathrm{p}} = j\omega L_{\mathrm{pp}} I_{\mathrm{p}} - j\omega M I_{\mathrm{s}}, \tag{3.13}$$

$$V_{\mathrm{s}} = j\omega L_{\mathrm{ss}} I_{\mathrm{s}} - j\omega M I_{\mathrm{p}}, \tag{3.14}$$

where V_{p} and V_{s} represent the voltages across the primary and the secondary windings. As described before, the complex effect of the core losses can be incorporated by the resistive component of the complex permeability μ''. However, incorporation of core losses can be further simplified by considering them as a resistor R_{cl} in parallel with the secondary winding [81]. The additional resistor R_{add} represents the built-in elements, which may be added due to design purposes [81] . Additionally, the effect of the flux leakage between windings is incorporated in terms of the coupling coefficient k given by

$$k = \frac{M}{\sqrt{L_{\mathrm{ss}} L_{\mathrm{pp}}}}, \tag{3.15}$$

where the coefficient k is a fractional number between 0 and 1 [77]. No coupling and full coupling are represented with 0 and 1 respectively.

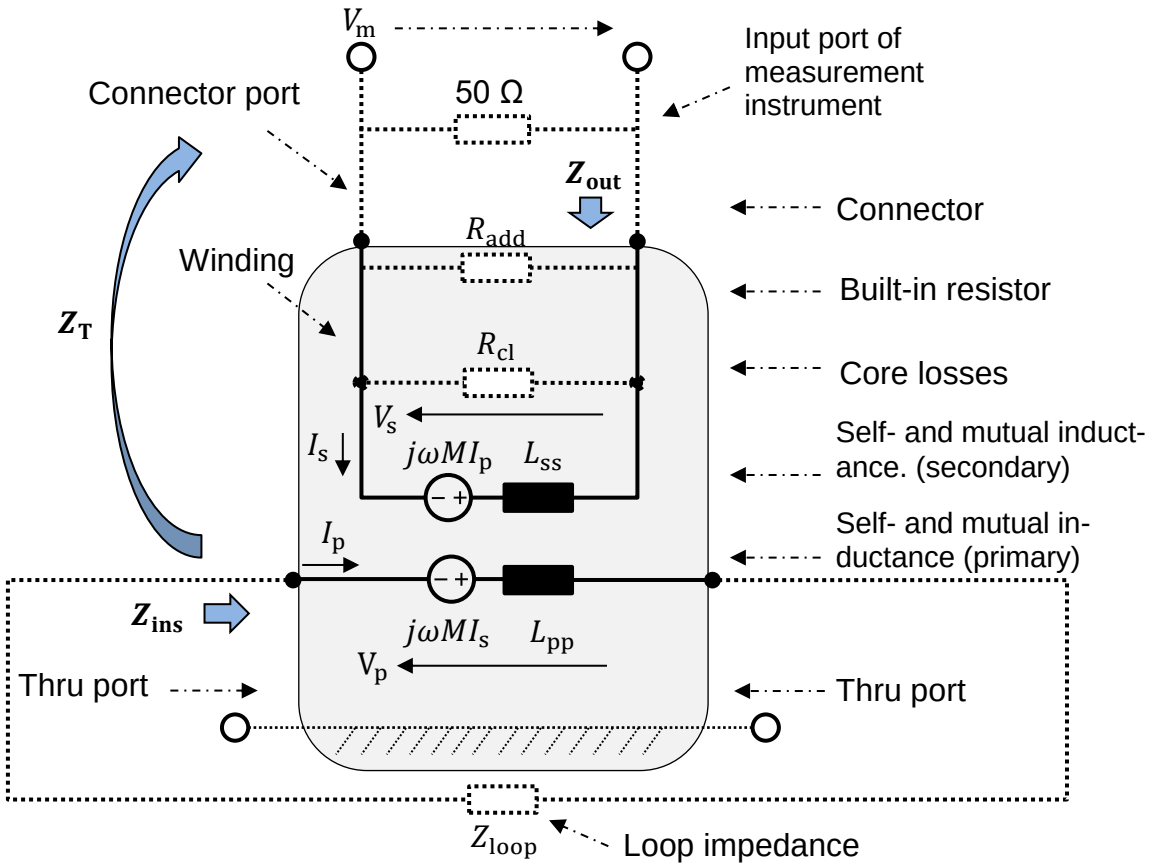

Figure 3.3: Lumped parameter model of a CT attached to a measurement device with 50 Ω input impedance

3.1.4 Derivation of Output Impedance

The connector port of a CT clamped around a conductor is the only directly accessible port, where the measurement instrument is usually connected. According to Figure 3.3, the output impedance Z_{out} available at the secondary terminals is a result of the self inductance of the secondary side L_{ss} in series with the transformed impedance due to the mutual inductance (regardless of the elements represented by dashed line). Based on (3.13) and (3.14) the output impedance can be derived as

$$Z_{\mathrm{out}} = \frac{V_{\mathrm{m}}}{I_{\mathrm{s}}} = -\frac{V_{\mathrm{s}}}{I_{\mathrm{s}}} = j\omega L_{\mathrm{ss}} + \frac{\omega^2 M^2}{Z_{\mathrm{loop}} + j\omega L_{\mathrm{pp}}}. \tag{3.16}$$

The effect of leakage flux can be included by substituting (3.15) into (3.16)

$$Z_{\mathrm{out}} = j\omega L_{\mathrm{ss}} + \frac{\omega^2 k^2 L_{\mathrm{ss}} L_{\mathrm{pp}}}{Z_{\mathrm{loop}} + j\omega L_{\mathrm{pp}}}. \tag{3.17}$$

A further improvement of the equivalent circuit can be achieved by considering the capacitive coupling between the terminals of each winding. Assuming that the inductive coupling is maximum, i.e. $k = 1$, the effect of parasitic coupling at primary side and the

secondary side, C_p and C_s, and the additional resistive elements can be incorporated with

$$\frac{1}{Z_{\mathrm{out}}} = \frac{-\omega^2 C_{\mathrm{p}} L_{\mathrm{pp}} Z_{\mathrm{loop}} + j\omega L_{\mathrm{pp}} + Z_{\mathrm{loop}}}{j\omega L_{\mathrm{ss}} Z_{\mathrm{loop}}} + \frac{1}{R_{\mathrm{s}}} + j\omega C_{\mathrm{s}}, \tag{3.18}$$

where R_{s} represents the resistive elements at the secondary side, i.e. $R_{\mathrm{s}} = R_{\mathrm{add}} \,||\, R_{\mathrm{cl}}$. Despite the relative complex behavior of the first term, the admittance is restricted to the values higher than the second and third terms in (3.18). In other words, the output impedance is always less than the smallest impedance in this parallel network. Low-resistive elements or higher parasitic capacitance C_s strengthen this effect. From (3.15) and (3.17) can be concluded that the output impedance is expected to increases linearly with frequency primarily. However, the middle and high frequencies are dominated by core losses, built-in elements and the capacitive couplings at the secondary side. This highlights the effect of the connectors at very high frequencies, where the output impedance is significantly influenced by the CT's connector.

3.1.5 Derivation of Insertion Impedance

The second parameter covering the interaction of a CT with a wiring harness is the insertion impedance Z_{ins}, which is defined as the impedance appearing in series with the clamped conductor [82][83][87]. In other words, the insertion impedance describes the loading effect of a CT on the clamped conductor. In general, little material exists concerning the details of loading effect or the implementation scheme to achieve a desired insertion impedance value in a wide frequency range. According to the guidelines for EMC current probes given in [87] the maximum allowable insertion impedance is equal to 1 Ω for the entire frequency range of interest. The reason for this choice is the perturbation produced by CTs clamped around the wire harness during the normal operation or test conditions. A CT with high insertion impedance alters considerably the primary current flow and therefore, may lead to incorrect test results [82-83].

Basically, the act of transformation is bilateral. This means that the impedance attached to the secondary winding is transformed to the primary side as well. Consequently, the entire considerations regarding the output impedance are valid for the derivation of the insertion impedance. For example, a rough estimation can be made for the insertion impedance based on the approximation for an ideal CT. Based on (3.12), for an ideal CT with more than 8 turns of winding at the secondary side and a 50 Ω load, the insertion impedance is approximately less than 1 Ω, which is an acceptable value for most applications [87]. Nevertheless, the equivalent circuit model illustrated in Figure 3.3 can be used to improve the primary estimation based on (3.12). According to Figure 3.3 the total impedance available at the primary side Z_{p} can be derived based on (3.13) and (3.14) with

$$Z_{\mathrm{p}} = j\omega L_{\mathrm{pp}} + \frac{\omega^2 M^2}{R + j\omega L_{\mathrm{ss}}}, \tag{3.19}$$

where R represents the entire resistive elements in parallel at the secondary side including the built-in resistor, core losses and the termination impedance of the measurement instrument ($R = R_{\mathrm{add}} \,||\, R_{\mathrm{cl}} \,||\, 50\Omega$). Basically, the insertion impedance is a result of two dominant terms: the introduction of a magnetic core material inside the primary circuit and the transformation of the secondary impedance into the primary side [77]. In order to relate Z_{p} to the insertion impedance for a CT with N windings at the secondary side, the effect of the primary inductance in absence of core has to be removed from the (3.19). For this purpose, according to [51][82][83], the insertion impedance can be calculated using

$$Z_{\mathrm{ins}} = \frac{j\omega L_{\mathrm{ss}}}{N^2} + \frac{\omega^2 M^2}{R + j\omega L_{\mathrm{ss}}} - j\omega L_{\mathrm{w}}, \tag{3.20}$$

where L_{w} represents the inductance of the primary winding. Substituting (3.10) in (3.20) and rearranging the expression yields

$$Z_{\mathrm{ins}} = \frac{1}{N^2}\frac{j\omega L_{\mathrm{ss}} R}{R + j\omega L_{\mathrm{ss}}} - j\omega L_{\mathrm{w}}. \tag{3.21}$$

This can be applied to approximate the behavior at lower and higher frequencies. At low frequencies, the impedance of the wire is negligible and $R \gg \omega L_{ss}$. Hence, the insertion impedance can be approximated with the frequency-dependent expression as follows

$$Z_{\mathrm{ins}} \approx \frac{1}{N^2} j\omega L_{\mathrm{ss}}. \tag{3.22}$$

In the middle frequency range, the impedance of the winding is still negligible and $R \ll \omega L_{\mathrm{ss}}$. Hence, the insertion impedance can be approximated with

$$Z_{\mathrm{ins}} \approx \frac{1}{N^2} R \tag{3.23}$$

At higher frequencies, however, the inductance ωL_{w} becomes dominant and the insertion impedance can be approximated with

$$Z_{\mathrm{ins}} \approx -\frac{1}{N^2} j\omega L_{\mathrm{w}}. \tag{3.24}$$

Although the abovementioned equations describe the insertion impedance, the parasitic capacitive couplings can also result in some deviations to the approximated values. For example, the capacitive coupling between different metallic structures including windings, outer surface of CCTs and the ground plane may become dominant

at high frequencies. This effect can be incorporated by adding lumped capacitive elements to each side similar to (3.18).

3.1.6 Derivation of Transfer Impedance

The third parameter is the transfer impedance Z_{T}, which is defined typically for commercial current probes as the ratio of the voltage developed across the connector port of the probe to the current flowing through the clamped conductor. This can also be interpreted as the sensitivity of the measured voltage to the current changes at primary side and can be derived from (3.13) and (3.14) as

$$Z_{\mathrm{T}} = \frac{V_{\mathrm{m}}}{I_{\mathrm{p}}} \Rightarrow Z_{\mathrm{T}} = \frac{-V_{\mathrm{s}}}{I_{\mathrm{p}}} = \frac{j\omega MR}{j\omega L_{\mathrm{ss}} + R} \tag{3.25}$$

where V_{m} is the measured voltage at the connector port of probe or CT. Similar to (3.19), the resistor R represents the entire resistive elements in parallel at the secondary side ($R = R_{\mathrm{add}} \,||\, R_{\mathrm{cl}} ||\, 50\Omega$). The effect of flux leakage can be considered by substituting the mutual inductance with the one given in (3.15) by

$$Z_{\mathrm{T}} = \frac{j\omega k^2 L_{\mathrm{ss}} L_{\mathrm{pp}} R}{j\omega L_{\mathrm{ss}} + R}. \tag{3.26}$$

Equation (3.25) can be applied to approximate the behavior at lower and higher frequencies. According to (3.25), the low frequency and the high frequency approximation of the transfer impedance is given by

$$Z_{\mathrm{T}} \approx j\omega M \tag{3.27}$$

and

$$Z_{\mathrm{T}} \approx \frac{M}{L_{\mathrm{ss}}} R \tag{3.28}$$

respectively. In general, the behavior of the voltage across the output terminals V_m can be explained by assuming the secondary side as a low pass RL filter. The simplified structure is illustrated in Figure 3.4(a). By assuming a constant current at the primary swept in the frequency range of the interest, the effect of the mutual inductance can be considered as a current-controlled voltage source (CCVS) whose instantaneous value increases linearly with frequency at 20 dB/decade (green). As can be seen clearly in Figure 3.4(a), the self-inductance of the secondary side, core losses, built-in resistor and the port impedance of the measurement device forms a low pass RL filter. At low frequencies, the filter indicates a flat response up to the corner frequency, which is specified by both resistive and inductance components of the filter. At higher frequencies RL filter has a roll-off rate of 20 dB/decade (blue). By combining the impact of CCVS and the frequency response of the RL filter, the behavior of the input voltage

can be approximated. The result depicted in red indicates that at low frequency region the voltage rises with frequency. However, at the frequency region above the corner frequency. the voltage shows a flat behavior. According to the definition of the transfer impedance given in (3.25), the similar behavior is expected for the transfer impedance.

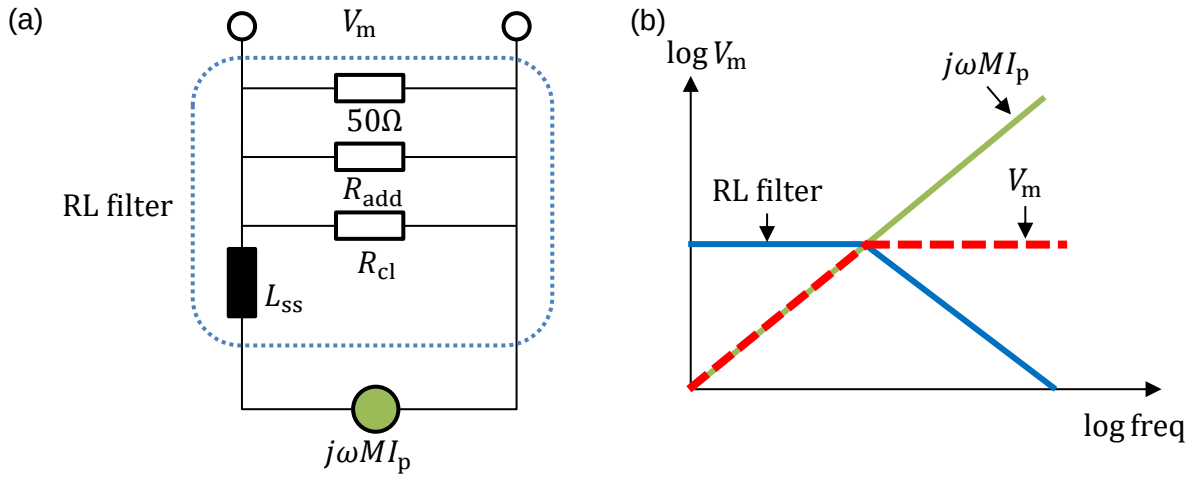

Figure 3.4: Equivalent circuit describing the secondary side of a CT based on RL filter interpretation (a), approximation of the output voltage behaviour at low and high frequencies (b)

In general, current probes are designed to provide a flat frequency response over a certain frequency band, which corresponds to the approximation given by (3.28) for higher frequencies. Additionally, to obtain maximum sensitivity for measuring current, the transfer impedance should be as high as possible. The common value for transfer impedance is between 0.1 Ω to 5 Ω [87]. Conversely, for injection probes, the insertion loss commonly replaces the transfer impedance. The insertion loss curves provided by manufactures of BCI probes are normally obtained in a calibration setup with 100 Ω loop impedance [76], and show the ability to inject a certain amount of power into the standard circuit. The analytical derivation of insertion loss is not covered in this work.

3.2 Measurement-Based Modelling of Current Transformers

As described before, although the representation of CTs in terms of the lumped parameter model is acceptable for describing various properties, a more accurate model obtained in situ is required to cover the spectral content. For this purpose, the three-port model of a CT based on a S-parameter measurement proves to be appropriate. The modelling approach is similar to that of a BCI probe in Section 2.2.3. As illustrated previously in Figure 3.3, the CT's connector (connector port) and the terminals between the clamped conductor and the ground plane at each side (thru ports) represent all three ports of the network. The measurement setup is illustrated in Figure 3.5. Since both thru ports aren't accessible directly, the single wire is spanned within two vertical fixtures in 50 mm over a copper ground plane. The length of the wire is 30 cm. This length is deliberately selected to obtain a trade-off between de-embedding inaccuracies and the parasitic coupling with fixtures. Additionally, both transitional SMA

connectors are used to make the thru ports accessible to the measuring device. The list of the measured CTs and ferrite cores is given in Table 3.1. The list can be divided to two major categories: the commercial current transformers (CCT) and the ferrite cores used to make the self-made current transformers (SCT) from different manufacturers.

	Manufacture	Model	Core material	cross sectional radius (mm)	Connector type	Abbr.
1	Fischer Custom Communications	F-65	-	19	N	F-65
2		F-36-2	-	19	SMA	F-36
3		F-140	-	70	N	F-140
4	Tektronix	CT1	-	18	SMB	CT1
5	Fair-Rite	596 800 2701	NiZn	12	SMA	F1
6		596 700 2701	NiZn	12	SMA	F2
7		596 600 2701	NiZn	12	SMA	F3
8		595 202 0801	NiZn	12	SMA	F4
9	Würth Elektronik	742 712 22	NiZn	27	SMA	W1
10		742 727 22	MnZn	27	SMA	W2

Table 3.1: Overview of the CCTs and cores chosen in this section, the term cross sectional radius indicates the length of the CT parallel to the wire and corresponds to h in Figure 3.2

The CCT category includes three current probes and a BCI probe. They are a part of EMC measurement setups and are typically characterized in terms of their transfer impedance or insertion loss. The second category include the different cores from soft ferrite materials. The ferrite cores are equipped with a single winding and a SMA connector to form the secondary side of a CT. The ferrites used in this work can further be divided in two subdivisions: the toroidal NiZn ferrites suitable for broadband or inductive applications (F1, F2, F3, F4) and the snap ferrites from NiZn or MnZn adapted to the cable diameter for interference suppression (W1, W2).

A four-port Agilent E5071B network analyzer is used to obtain the S-parameters between 300 kHz and 1 GHz. As shown in Figure 3.5, the three-port S-parameter dataset is recorded by connecting the port 1 with the connector port directly and SMA connectors with second and third port of the VNA. The effect of the measurement cables is calibrated with a full three-port calibration. Additionally, the measurement cables are equipped with several snap ferrites to decouple the measurement instrument from the measurement setup. The de-embedding procedure is carried out similar to Section 2.2.3 by interpreting the setup as three separate modules including: a two-port network on the left (fixture and wire), a three-port central module (CT model), and a two-port network on the right (fixture and wire). The single wire and test fixtures are characterized in advance according to Section 2.2.2 and are considered together as a two-port network with a known S-parameter matrix.

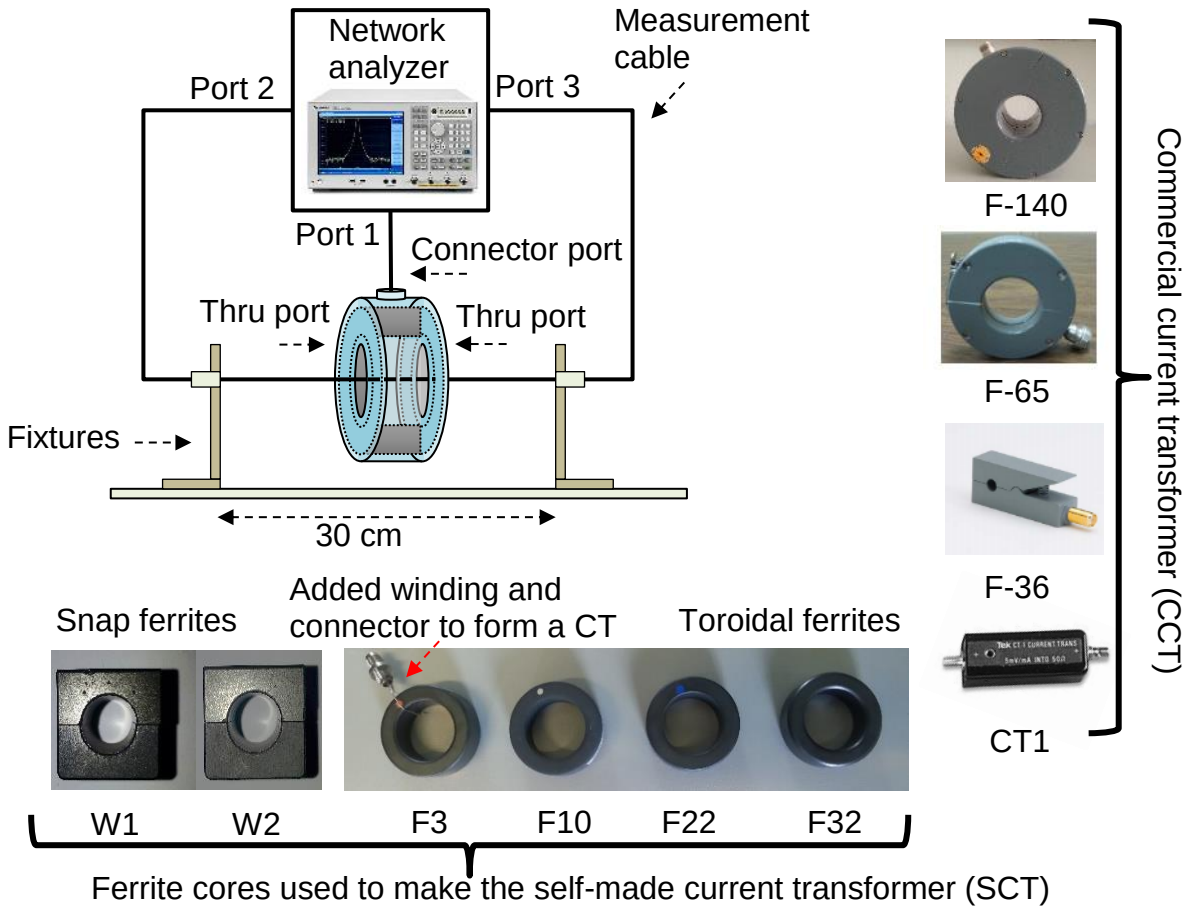

Figure 3.5: Setup for measuring the S-parameters to obtain the three-port CT model after de-embedding the redundant segments from the raw measurement data

3.2.1 Determination of Output Impedance

According to (3.16), the output impedance is a direct function of different parameters, including self inductance, mutual inductance and loop impedance. Therefore, a comprehensive analysis of output impedance cannot ignore the amount of loop impedance. However, in this section, the focus remains on the behavior of the secondary side in absence of any load at the primary side by giving useful indications on loss phenomena based on a reflection measurement with VNA. In general, the frequency behavior of CT's secondary side can be determined straightforwardly in a setup composed of a VNA connected to the connector port of a CT in absence of the primary winding. However, to facilitate further investigations and to avoid repeating the measurements, a similar structure is prepared by using the three-port CT model.

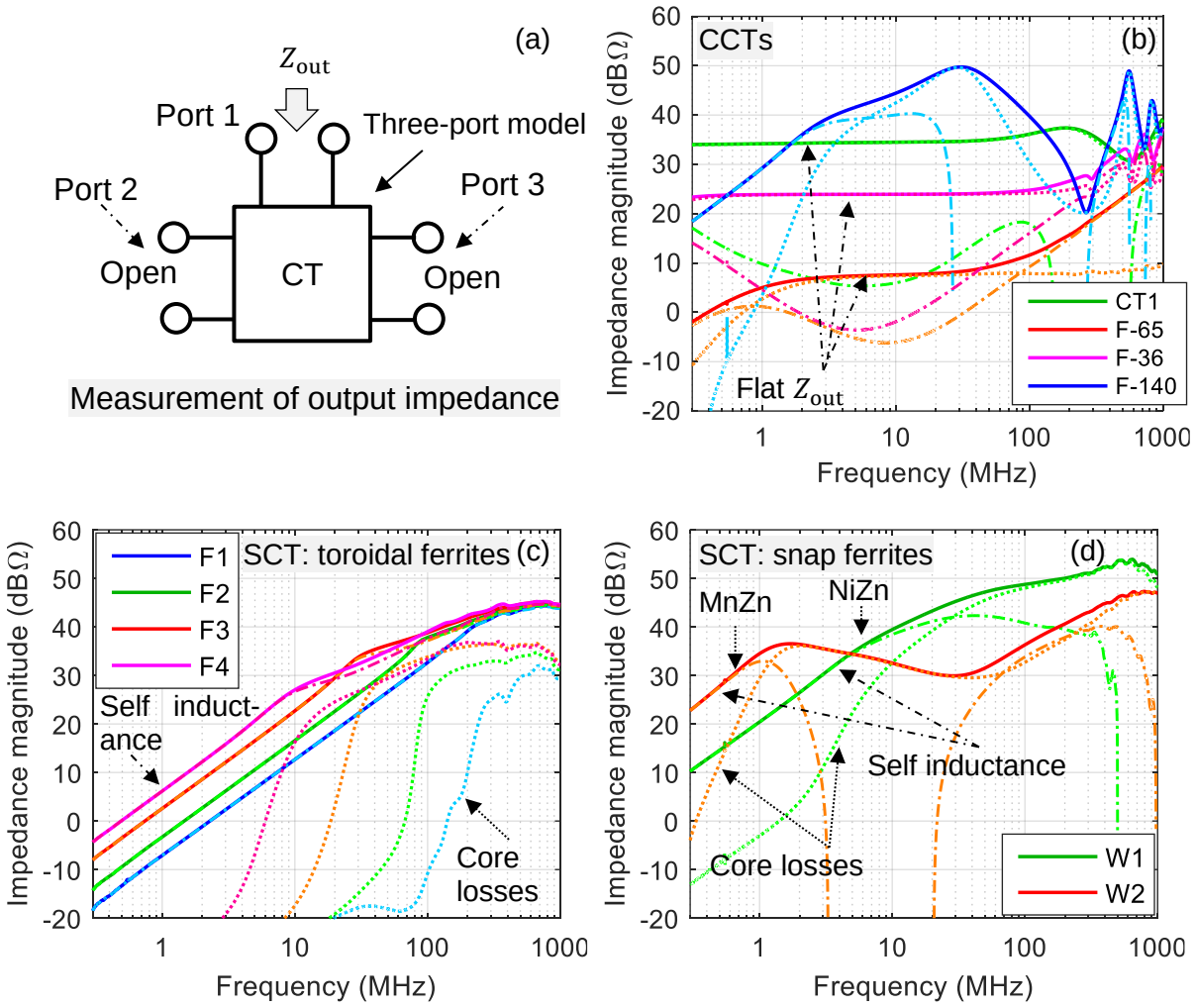

Figure 3.6: Application of three-port S-parameter dataset to determine CT's output impedance (a), the impedance magnitude of the CCTs (b), SCTs from toroidal ferrites (c), SCTs from snap ferrites (d). The impedance magnitude is shown with solid line. The real part of the complex impedance is represented with (---) and the imaginary part is represented with (···).

The three-port CT model comprises the effect of the 50 Ω impedances of the measurement ports, which have to be removed from three-port model. For this purpose, first, as illustrated in Figure 3.6(a), the open circuit condition is realized at port 2 and port 3 based on Section 2.2.1. To avoid numerical problems in the simulation environment, open circuit condition can be implemented, for example, by replacing each port impedance (50 Ω) with a very high-impedance load. Second, the new one-port S-parameters model is converted to Z-parameters to obtain the output impedance [63]. The results demonstrated in Figure 3.6 include not only the magnitude but also the positive real and imaginary parts of the complex output impedance. In order to achieve a better distinguishability, the impedance curves are illustrated separately. Figure 3.6(b) includes the result for the CCTs including CT1, F-36, F-65 and BCI probe (F-140). Figure 3.6(c) includes the results for the SCTs made from toroidal ferrites, F1, F2, F3 and F4. Figure 3.6(d) includes the results for the SCTs made from snap ferrites, W1 and W2.

Overall, the output impedance of the SCTs in Figure 3.6(c) and Figure 3.6(d) exhibits the expected behavior discussed in Section 3.1.4, i.e. the output impedance of a parallel circuit. The positive slope at the lower frequencies is dominated by the inductive behavior (self inductance of the secondary side) and the output impedance rises at 20 dB/decade up to the corner frequency. The effect of core losses is more apparent in the middle frequency region between the corner frequency and the maximum output impedance. The lower slope of the output impedance magnitude corresponds to the effects of the frequency dependent core losses described in Section 3.1.2. At the high frequency region, the impedance decreases due to the dominant effect of the capacitive couplings on the parallel impedance. Conversely, the flat real parts in Figure 3.6(b) indicate that except for the BCI probe (F-140), the output impedance of the CCTs is dominated by the additional built-in resistors. For example, in case of CT1, an additional 50 Ω resistor can be observed. This corresponds to the internal structure of CT1 given in [52]. In case of the BCI probe (F-140), the length of the secondary winding is more than 12 cm. As described in 3.1.2, this complex behavior of the output impedance is caused by an increase in the induced eddy currents as well as an increased magnetic loss due to the shape and size of the core. In particular, the results for toroidal and snap ferrites in Figure 3.6(c) and (d) highlight the effect of the core material and the connector on the output impedance. While there is a significant difference between the output impedance at lower frequencies due to different core materials, the output impedances tend to converge at higher frequencies due to the connector.

A further step in this investigation could be the characterization of core properties based on the estimated output impedance. There are a variety of linear, impedance based measurement methods for the characterization of core losses such [80][89][90][91][92]. To achieve linear operating conditions in these methods, losses are measured typically with the excitations that minimize the nonlinear core effects. As an alternative, curve-fitting approximation of the output impedance value to a model such as (3.18) can be used to determine different parameters at the secondary sides including self inductance and resistive elements. However, as mentioned earlier, due to the inherent behavior of the magnetic material and the dimensional effects such as eddy currents and dimensional resonances [26][29][79], the core material exhibits complicated frequency profiles that typically cannot be predicted analytically. In order to overcome this difficulty and obtain a fast and accurate representation of the frequency response of the ferrite core, the complex, frequency-dependent, self inductance $L(\omega)$ is commonly used to relate the output impedance and the material properties. This is the usual characterization approach which is often applied on manufacturers' data, reported from measurements on relatively small cores under the assumption that eddy current loss is small for those cores [79]. The relation between the output impedance and the inductance is given by

$$Z_{\text{out}} = j\omega L(\omega). \tag{3.29}$$

Hence, the self inductance can be simply obtained by dividing the complex output impedance by $j\omega$. However, as mentioned above, the effect of the input connector is dominant at higher frequencies. Therefore, it has to be de-embedded from the output impedance by means of a two-port network or a simple LC circuit describing the frequency response of the connector.

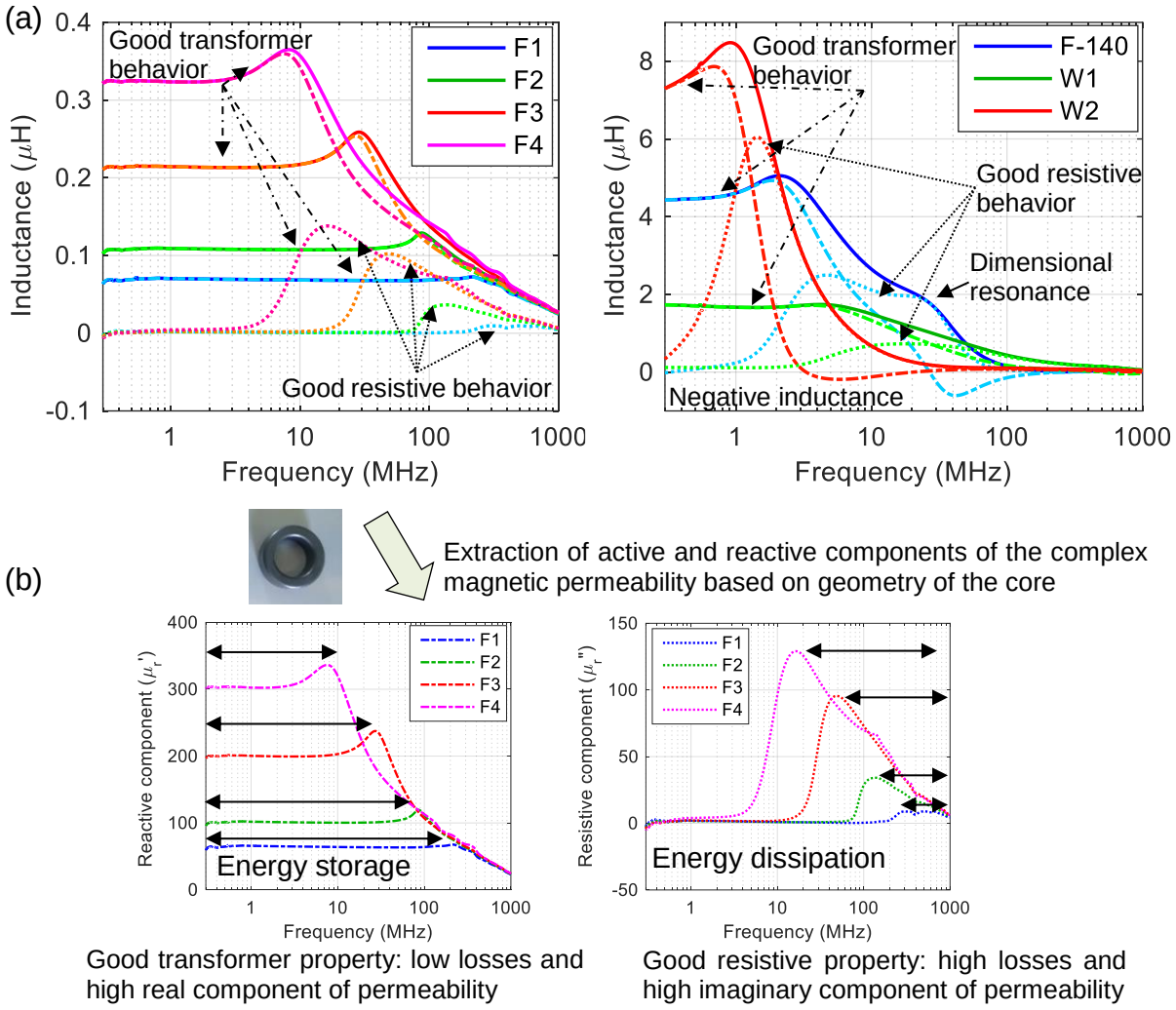

Figure 3.7: Extraction of the complex, frequency dependent inductance from the output impedance of SCTs and the BCI probe (F-140), the real part (···) and imaginary part (···) are demonstrated for the complex value of the extracted inductance. The magnitude is shown with solid line. (a), Extraction of active and reactive components of the complex magnetic permeability based on the geometry of core for the SCTs from toroidal ferrites based on the calculated L_0 (b)

The estimated results are shown in Figure 3.7(a) and Figure 3.7 (b) only for SCTs and the BCI probe (F-140). Since (3.29) only comprises the inductive behavior of the secondary side, the effect of the additional built-in elements in CT1, F-65 and F-36 has to be removed from the output impedance to be able to demonstrate the inductive behavior of the secondary side. As can be seen the inductances take complex and frequency dependent values, which are mainly caused by the core losses. Overall, the

inductance magnitude exhibits a flat behavior followed by a peak and a sharp negative slope. In particular, the inductance of the BCI probe (F-140) has a second frequency peak (around 30 MHz), followed by negative values of inductance. This is due to a dimensional resonance, which typically occurs in large ferrite cores [79]. The obtained inductance can also be interpreted in terms of equivalent complex permeability spectra of the ferrite core, by resorting to the concept of complex relative permeability [79][80][89] with

$$Z_{\mathrm{out}} = j\omega L_0(\mu_r' - j\mu_r'') \tag{3.30}$$

where L_0 denotes the inductance that would be measured if the core had unity permeability. This parameter depends on the geometry (shape and size) of the core and was previously derived for toroidal shapes in (3.8). The obtained reactive and resistive components of the complex permeability correspond very well to the core properties of the toroidal ferrite cores given in [93]. For other shapes, it can be derived based on the effective cross-sectional area of the core and the and the effective magnetic length as described in [77-80].

From the results, it can be concluded that the measurement-based parameter is a powerful tool to investigate different core characteristics and loss phenomena and allows a fast and accurate determination of the complex impedance of the CT under small signal sinusoidal excitation. However, two critical issues remain:

- representing the nonlinearities of the cores,
- separating the measured resistance into components related to the various types of losses that occur in ferrite.

Therefore, more complex methods are required for the characterization of cores. An accurate solution to overcome these issues is proposed in e.g. [79]. The approach is called “impedance analyzer core loss measurement”, which permits the determination of the complex impedance of a given core under large signal sinusoidal excitation by means of an impedance analyzer along with separate linear amplifiers and attenuators.

3.2.2 Determination of Insertion Impedance

The derivation of insertion impedance based on the proposed lumped parameter model was given in Section 3.1.5. In order to measure the insertion impedance of a CT, the three-port network model can be used. In a similar manner as for the output impedance, first, the three-port network model has to be terminated properly. For this purpose, as illustrated in Figure 3.8(a) the connector port (port 1) is terminated with a 50 Ω impedance to emulate the standard port of the measurement device. Moreover, the terminals of port 3 are shortened to create a closed loop at the primary side.

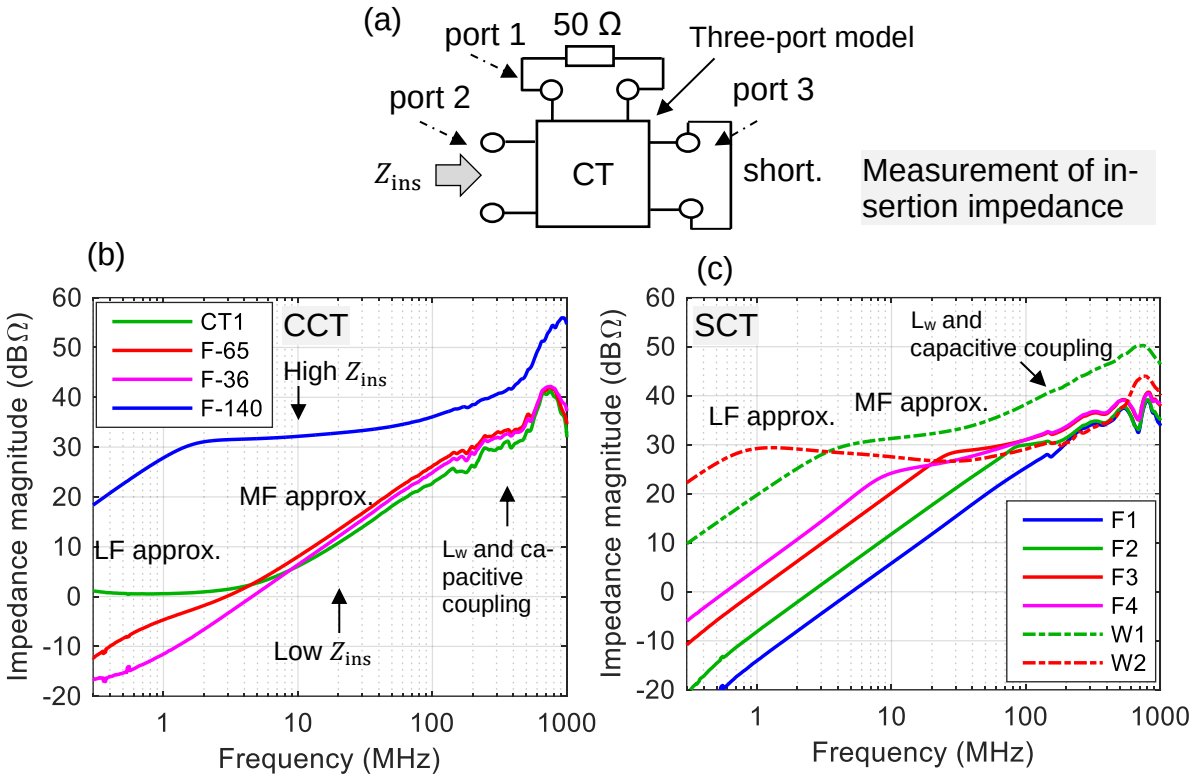

Figure 3.8: Application of three-port S-parameter dataset to determine the insertion impedance (a), the extracted impedance magnitude of the CCTs (b), SCTs (c)

The measured insertion impedances are shown in Figure 3.8(b) and Figure 3.8(c). Overall, none of the analyzed CTs correspond to the maximum allowable insertion impedance of 1 Ω as specified in [74] up to 1 GHz. In case of SCTs and the BCI probe (F-140) the impedance rises linearly with frequency at 20 dB/decade up to the corner frequency and corresponds to (3.22). At middle frequencies, the slope decreases. This is the region where the impedance of the clamped wire is still negligible and the core losses become dominant. At higher frequencies, the behavior of winding inductance L_{w} is dominant and the insertion impedance is highly affected by the capacitive couplings and the errors related to the extraction of the three-port model. Conversely, as mentioned earlier, regardless of the BCI probe, the commercial current probes are designed to have the least possible insertion impedance. High number of turns at the secondary side, additional built-in elements and appropriate core material lead to an acceptable insertion impedance at lower frequencies. However, the impact of insertion impedance on the current flow in wire harness cannot be neglected at higher frequencies and should be taken into account for the analysis of EMC test setups.

3.2.3 Determination of Transfer Impedance

Typical datasheets of current monitoring probes provide merely the magnitude of the transfer impedance measured in a standard calibration fixture [74][86]. To reduce calibration errors and to maximize the measurement accuracy, calibration is generally

performed in a 50 Ω end to end system. The aim of such structure is to minimize the voltage standing wave ratio at the input of the calibration fixture [74]. However, in accordance with the definition of the transfer impedance given in Section 3.1.6, it can also be calculated directly from the extracted three-port model.

According to Figure 3.9(a), the current flowing into the second port I_2 for a known forward power P_{Fwd}, can be calculated by

$$I_2 = (1 - S_{22})\sqrt{\frac{P_{\mathrm{Fwd}}}{Z_0}}, \tag{3.31}$$

where S_{22} is the reflection coefficient at port 2 and Z_0 is the reference impedance of the measurement system. Additionally, the corresponding induced voltage across the first port V_{m} for any power at the second port is calculated by

$$V_{\mathrm{m}} = S_{12}\sqrt{P_{\mathrm{Fwd}} \cdot Z_0}, \tag{3.32}$$

where S_{12} is the transmission coefficient between port 1 and port 2. The transfer impedance can be calculated by substituting (3.31) and (3.32) in the definition of Z_{T} given in (3.25) as

$$Z_{\mathrm{T}} = \frac{V_{\mathrm{m}}}{I_{\mathrm{p}}} = Z_0 \frac{S_{12}}{1 - S_{22}}. \tag{3.33}$$

For this purpose, first, the calibration setup is prepared by connecting 50 Ω to port 2 and 3. The transfer impedance is then calculated using (3.33).

The estimated transfer impedance Z_{T} are shown in Figure 3.9(b) for the CCTs. As expected, CT1, F-65 and F-36 demonstrate a flat magnitude in a wide frequency range. For example, F-65 and F-36 with a 1 Ω transfer impedance will have a 1 V output for a current passing through of 1 A. Both low and high frequency behaviors correspond well with (3.27) and (3.28) and the equivalent circuit given in Section 3.1.2. As described before, the added resistor does not affect the open circuit voltage, but it lowers the corner frequency of the LR filter illustrated in Figure 3.4. Conversely, the BCI probe and SCTs exhibit an inconstant transfer impedance trend with a higher sensitivity to the current changes at their primary side. The transfer impedance reaches higher values due to the absence of low-resistive, built-in elements. Nevertheless, as mentioned earlier, the core losses and the port impedance of measurement device act as the resistive elements of the LR filter and dominate the parallel circuit at the primary side, especially at higher frequencies. Hence, a parallel resistance at the connector port of SCTs or BCI probe can be used to extend the flat region of frequency response at the expense of their sensitivity.

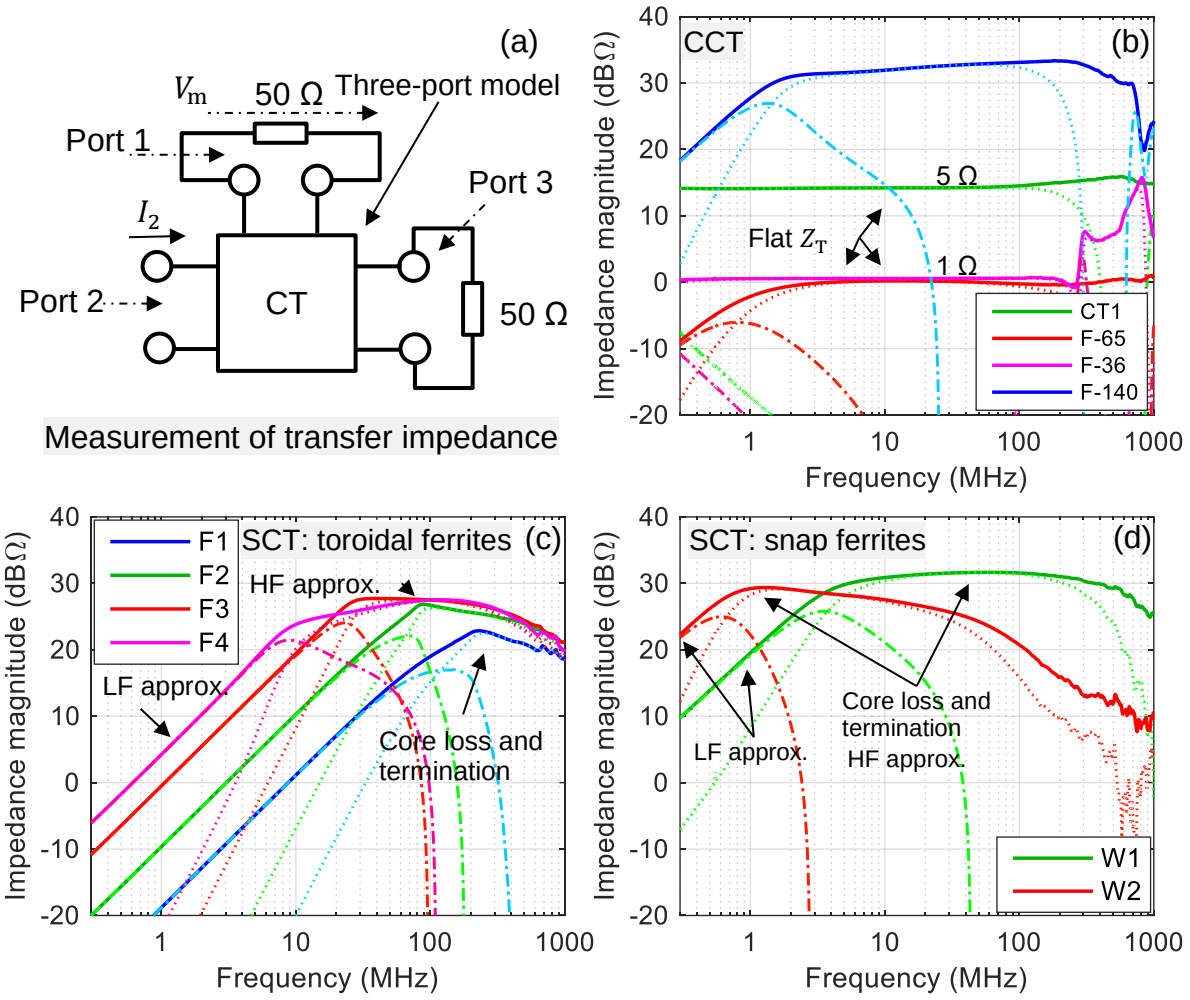

Figure 3.9: Application of three-port S-parameter dataset to determine CT's transfer impedance (a), the extracted impedance magnitude of the CCTs (b), SCTs from toroidal ferrites (c), SCTs from snap ferrites (d). The impedance magnitude is shown with solid line. The real part of the complex impedance is represented with (-·-) and the imaginary part is represented with (···).

3.3 Impedance Transformation

In line with the concept of impedance measurement with CTs based on reflection measurement with a VNA, an accurate determination of loop impedance as an intermediate value is from considerable importance. The aim here is to assess the practicability, strength and weakness of a CT as an impedance probe in combination with a measurement instrument and a de-embedding process based on the extracted three-port model.

3.3.1 Limitations of Measurement

According to (3.18), the impedance measured directly at a CT's connector port is the result of the loop impedance weighted by the transfer function of the CT. Therefore, a straightforward method to determine the loop impedance is to remove the impedance transfer function from the measurement.

Basically, VNA measurements are associated with different sources of error, which are mainly classified as systematic, random, and drift errors [94]. During a VNA calibration, the systematic errors are characterized and most of them are mathematically removed from the raw measurement data. Although, the effect of other sources of error may be reduced by means of appropriate measures such as considering a warm-up phase or using a shielded enclosure [94], they cannot be removed completely. One crucial limitation according to different publications is that any uncertainty measurement is valid only for the same parameters settings, same measurement equipment and the same ambient conditions [94][96]. Although any change to these parameters requires repeating the uncertainty measurements and analysis, typical values can serve as a useful tool in this particular area. For example, according to [95] and [97], a typical network analyzer, after a complete calibration, shows a deviation of typically 0.05 dB and 2° which continuously decreases during a warm up phase to typically 0.005 dB and 0.1°. Another limitation is measurement of very low or very high impedances. In this case, the magnitude of the reflected signal is so close to 1 that it is difficult to be distinguished by the VNA's detector. This fundamental problem of the one-port measurement technique and the related sensitivity to errors have a direct impact on the accuracy of the calculated impedance based on S-parameter measurement with a VNA [98].

As described in Section 3.2.2, in order to satisfy the requirements of [74] concerning the insertion impedance and to ensure specific transfer impedance, commercial current probes are equipped with higher number of turns at secondary side. Moreover, they are optimized with additional built-in elements at the secondary side. The commonly used EMC current probes typically operate at the impedance ratio of 1:50 to achieve an insertion impedance less than 1 Ω for a wide frequency range. However, the impedance ratio can even reach 1:2500 in case of special current probes, to guaranty the required insertion impedance at very high frequencies [51]. According to transmission line theory, variation of the voltage and current ratio along a line for mismatched terminations leads to different maxima and minima at different locations along the line. Even in case of a matched line, where the termination impedances are equal to the characteristic impedance, the sum of termination impedances appear at the primary side of the CT, which is clamped around the line. According to transmission line theory, the impedance at any point along the line can be considered as the sum of both termination impedances transformed to this point. Impedance transformation along a line will be completely discussed in Chapter 4 in order to relate the termination impedances to the loop impedance. Any impedance at the primary side of the above-mentioned CT, i.e. loop impedance, is transformed directly to the secondary side and the VNA port. For example, assuming a matched transmission line with $Z_{\mathrm{c}} = 300\ \Omega$ and a CT with 1:50 or 1:2500 impedance ratio, the reflection coefficient S_{11} at the VNA port can be calculated by

$$S_{11} = \frac{Z_t - 50}{Z_t + 50} \tag{3.34}$$

where Z_t represents the transformed impedance. According to (3.34) the reflection coefficients for 1:50 and 1:2500 impedance ratios will be -0.029 dB and -0.0006 dB respectively. Both of the calculated reflections coefficients lie far below the measurement uncertainties of a typical VNA given in [95][97].

3.3.2 Brute Force Sensitivity Analysis

As shown earlier, the output impedance at the secondary side is a direct function of CT's characteristics and the loop impedance, i.e. the impedance attached to the primary side. A straightforward approach to assess the feasibility of a CT for impedance measurement is to compare the output impedances resulting from open and short circuits at the primary side.

Basically, the open and short conditions can be considered as the boundaries for the possible loop impedances. Therefore, determination of the corresponding output impedances gives a comprehensive overview of the transformation codomain, where the output impedances are constrained to fall. The difference or the gap between the upper and lower boundaries can be used to form a conclusion about the feasibility or the weakness of a CT for the purpose of impedance measurement. The bigger the difference between the resulted output impedances, the more appropriate the CT is for impedance measurement and the higher is the sensitivity. Additionally, as the impedance is a complex value, such investigation can be performed for both magnitude and phase of the complex value.

For this purpose, as illustrated in Figure 3.10(a), the output impedance of the CTs is measured for the open and short circuit conditions by terminating the thru ports of the extracted three-port model. As shown in Figure 3.10(b), F-65 and F-36 remain almost insensitive to the impedance changes at the primary side. This behavior corresponds to the expected output impedance of optimized current probes with built-in, low-resistive elements and high number of turns at the secondary side. Consequently, they are not appropriate for impedance measurement. In case of CT1, the situation is different. Although the results point out the existence of a built-in resistive components at the secondary side, the key difference is the value of the output impedance. Here, it can be clearly seen that the codomain of the CT1 at frequencies above 20 MHz lies in the region, where the VNA operates with high sensitivity, i.e. near 50 Ω. Conversely, as mentioned earlier, the BCI probe (F-140) has a 1:1 impedance ratio with no additional built-in element. The results of the BCI probe (F-140) show a significant big gap at a wide frequency range. Although the results at high frequencies are affected by the length of the windings and the dimensional resonances, the output impedance at these frequencies lies again in the region with an acceptable VNA sensitivity. From the

abovementioned observations can be concluded that CT1 and BCI probe are appropriate for impedance measurements.

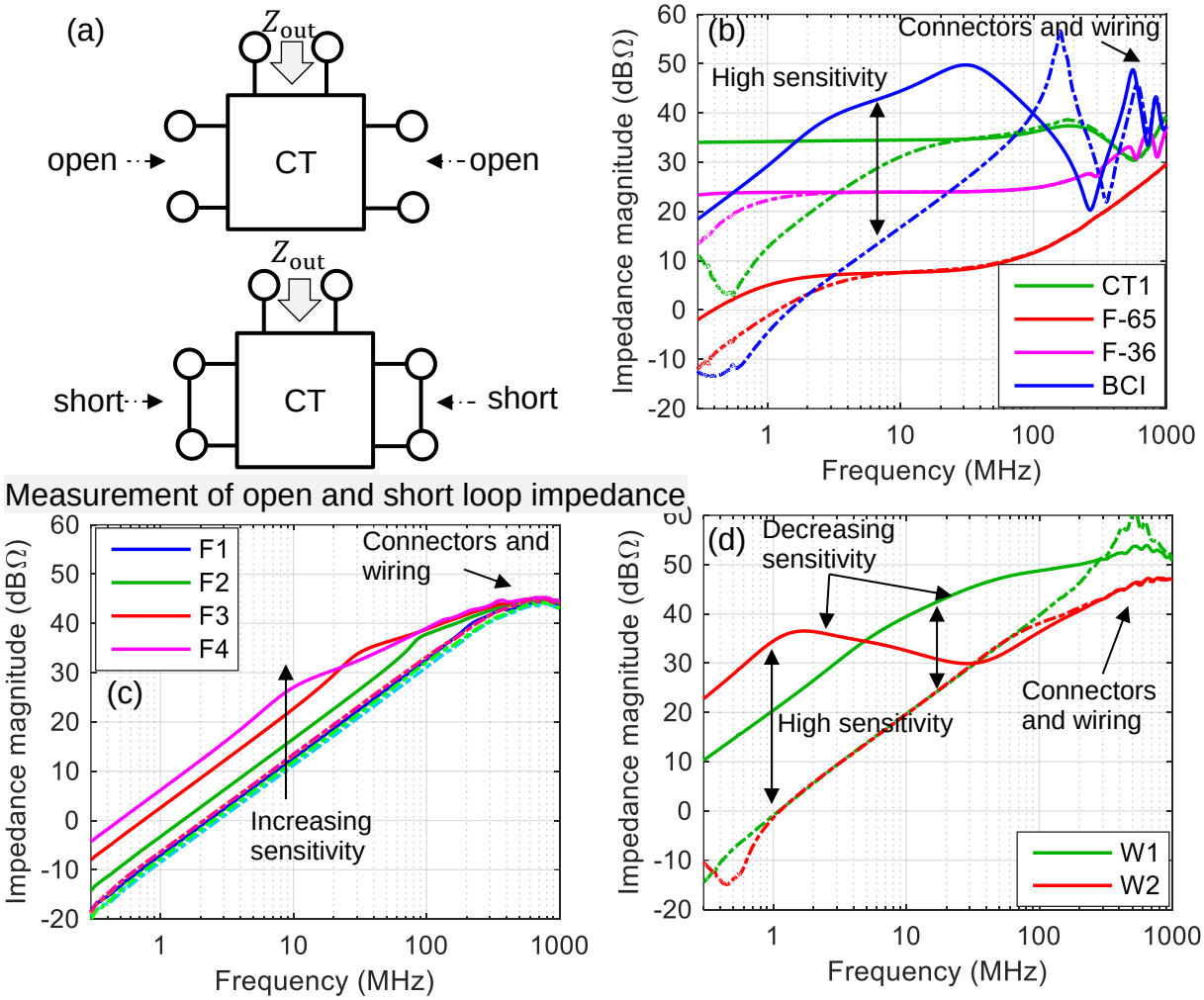

Figure 3.10: Measurement of the open and short circuits at the primary side by means of the extracted three-port model (a), comparison between the behaviour of the output impedance for an open circuit (–) and short circuit (-–-) at the primary side of the CCTs (b), SCTs from toroidal ferrites (c), SCTs from snap ferrites (d)

The overall behaviors of the SCTs shown in Figure 3.10(c) and Figure 3.10(d) are similar. The secondary side of the SCTs consists of a single winding. Regardless of the different geometries, the only difference is the core material. For example, it can be clearly seen in Figure 3.10(d) that the codomain of the W2 at frequencies above 30 MHz is highly affected by the inductance of the secondary winding. Conversely, in case of W1, the gap between the output impedances remains distinguishable even over 100 MHz. Similarly, the behavior of the output impedances shown in Figure 3.10(c) is distinguishable at lower frequencies. The trend at higher frequencies for all SCTs, as expected, is highly affected by the connector and core losses. From the observations can be concluded again that the high reactive component and low resistive component of the magnetic permeability at a certain frequency play vital roles to achieve a bigger gap.

In a similar manner, the brute force method can be expanded to a range of loop impedances at the primary side to obtain a better overview about the regions with higher sensitivity to the changes of loop impedance. For this purpose, a parametric surface specified by two independent variables including the loop impedance and the frequency is selected. The only difference to the previous illustration is the use of reflection coefficient instead of output impedance, i.e. the height is represented by means of a colormap proportional to the reflection coefficient magnitude instead of the output impedance magnitude.

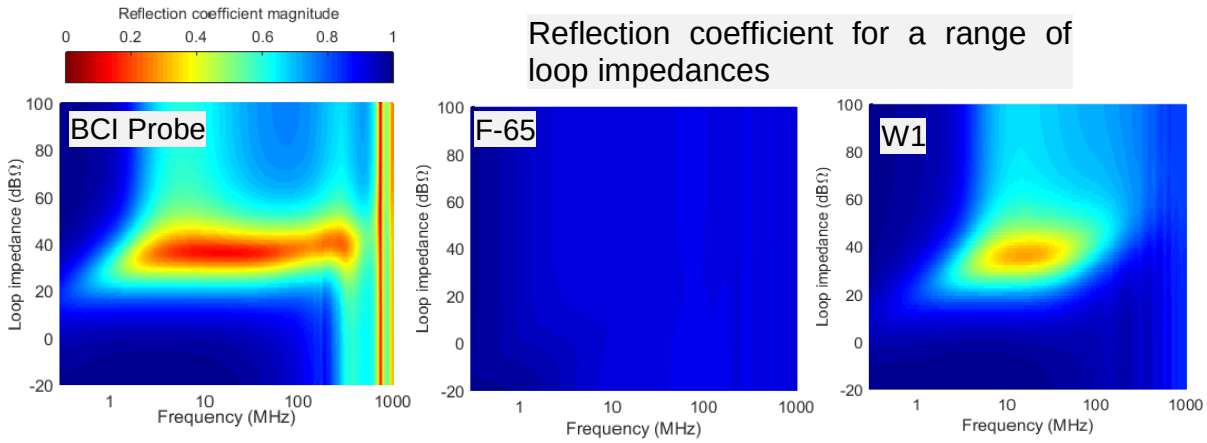

Figure 3.11: Reflection coefficient of the sample CTs including the BCI probe F-140, F-65 current probe and SCT with W1 ferrite for different loop impedances at primary side between 0.1 Ω and 100 kΩ

As mentioned earlier, VNA initially measures the complex reflection coefficient. This means that the magnitude of the entire possible output impedances is mapped into an interval between 0 and 1. Employing the reflection coefficient for such illustration appears to provide more distinguishable values than the output impedance. Thus, similar to the open and short circuit simulations, the reflection coefficient is calculated for the loop impedances between 0.1 Ω and 100 kΩ by cascading appropriate loads to the extracted three-port model. The results are illustrated by means of the wireframe surface in Figure 3.11 for three sample CTs. As expected, the results indicate that the current probes F-65 is not appropriate for the impedance measurement. It remains almost insensitive to impedance changes at the primary side. Conversely, the impact of the changes of loop impedance can be directly seen in case of the BCI probe F-140 and W1. Consequently, they can be used for the impedance measurement. As can be seen, the illustrated results for the sample CTs give a better insight into the possibility of measuring the impedance than the primary illustration of the brute force method, by giving more details about the regions with higher sensitivity. Similar procedure can be used to calculate the rate of change describing how the output impedance changes in relation to the loop impedance.

3.3.3 Validation of Brute Force Method

As mentioned before, a straightforward approach to determine the loop impedance is to remove the frequency response of the CT from the measured reflection data using an inverse function. The details of this approach are discussed extensively in Chapter 4. Therefore, the given results here are considered as preliminary. In order to validate the brute force method, a setup consists of a cable of length $l = 1\,\mathrm{m}$ was spanned within two fixtures. As illustrated in Figure 3.12(a) both ends of the wire are terminated with 50 Ω SMA-resistors. Three CTs including a BCI probe (F-140), W1 and F-65 are chosen for the validation. The one-port S-parameters is recorded by positioning each CT in the middle of the structure with the VNA Agilent E5071B. As mentioned above, the removal of the CT's frequency response is carried out using the single probe method (see Chapter 4). The raw measured impedance before de-embedding (primary results) and after de-embedding the CT's frequency response is shown in Figure 3.12(b).

As mentioned previously, according to transmission line theory, the impedance at any point along the wire can be considered as the sum of both termination impedance of wire ends transformed to this point. The determined loop impedance for the BCI probe (F-140) and W1 show a similar behavior. At lower frequencies, the sum of both termination impedances can be directly seen. However, at the frequencies above 10 MHz the effect of the wire is dominant and the estimated loop impedance is highly affected by the impedance transformation along the wire. Conversely, the measured loop impedance with the current probe F-65 does not follow the expected behavior neither at low frequencies nor at high frequencies. As described earlier, this behavior can be explained by the built-in, low-resistive elements and the high number of turns at the secondary side

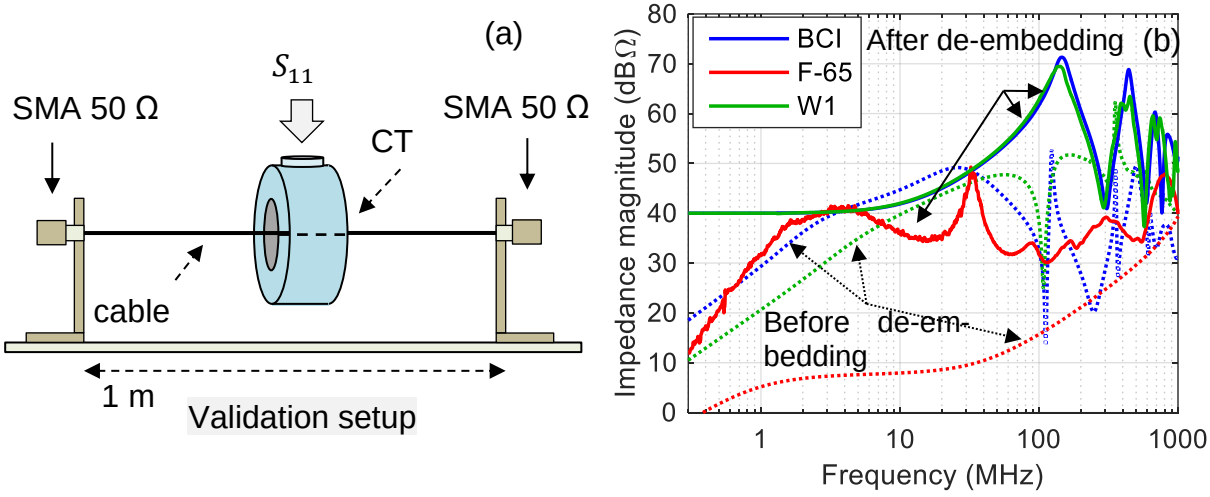

Figure 3.12: Validation setup for the brute force method (a), comparison between the raw measured impedance (…) and the determined loop impedance (solid lines) for the BCI, F-65 and W1 (b)

3.3.4 Optimized Impedance Transformer

From the stand point of impedance measurement, the output impedance is the key and primary quantity to determine the loop impedance. As mentioned earlier, a straightforward method to determine the loop impedance is to measure the reflection at the connector port of a CT. The loop impedance can be then calculated by removing the impedance transfer function of the CT from the measured reflection. The success of using CTs to measure the loop impedance is a complex function of three parameters including:

- physical properties and structure of the CT,
- properties of the measurement instrument,
- de-embedding method.

The first aspect is the physical properties and the structure of the CT. According to the theoretical background in Section 3.1.1, any change of the primary current produces a new magnetic field, which induces a new secondary current. From another point of view, any change to the loop impedance leads to a change of the output impedance. This means that, theoretically, any CT can be used for the purpose of impedance measurement. Nevertheless, the investigation in Section 3.3 showed that not every CT is appropriate for this purpose. Therefore, the success of using a CT as an impedance probe requires considering the CT, the measurement instrument and the de-embedding together. However, each of these items should fulfill certain criteria to make the impedance measurement possible. From the observations in this chapter, an optimized impedance probe should have the following properties:

- Permeability of Core: the complex magnetic permeability describes the frequency-dependent behavior of the magnetic permeability. A ferrite core with high reactive component μ_r' and low resistive component μ_r'' has less stray fields and less core losses. The MnZn ferrites cover lower frequencies than NiZn. Therefore, with respect to the frequency range of immunity tests the NiZn is more appropriate. Although modern materials such as nanocrystals offer higher reactive and lower resistive components in a wider frequency range, due to the brittle character of the nanocrystal, their application as core is still inappropriate [51][80]. An impedance probe requires high μ_r', to have a good inductive coupling between measurement instrument and the wiring harness. High μ_r'' increases the ohmic losses which attenuate the signal and therefore, reduce the measurement dynamic. Both of these frequency-dependent parameters have to be valid for the desired frequency range. The curves representing μ_r' and μ_r'' are commonly given up to a certain frequency in the datasheets of magnetic materials. Higher frequency behavior can be determined with the proposed method in Section 3.2.1.

- Permittivity of Core: typical relative permittivity of cores from MnZn or NiZn ferrites is $\epsilon_r \approx 10 - 30$ for the frequencies between 1 MHz and 1 GHz. Although permittivity is mainly ignored at low frequencies, it can become an important parameter at high frequencies. Having a high permittivity increases the parasitic capacitive couplings, e.g. between windings.
- Number of turns: an equal impedance ratio (1:1 turns) transforms the loop impedance directly without being multiplied. This is the most appropriate impedance ratio. A CT with high impedance ratio reduces the dynamic of measurement. Such measurement suffers from the high output impedance at the CTs connector port.
- Shape and Size: the toroidal shape has the lowest flux leakage due to the continuous magnetic path tangential to the core's surface. Measurements with a CT with smaller dimensions are less affected by capacitive couplings.
- Additional elements: low-impedance elements at the secondary side makes it difficult to measure the loop impedance and require higher measurement dynamic.

Besides the above-mentioned properties the following measurements can be used to make a statement about the feasibility of a CT to be used as an impedance probe:

- Measurement of the transfer impedance: a CT with high transfer impedance is a good candidate for impedance measurement. The transfer impedance of 0 dB in commercial current probes are achieved by combination of high number turns and additional low-impedance elements at the secondary side, which are inappropriate for the impedance measurement.
- Brute force analysis of the codomain of transformation: having a distinguishable reflection coefficient for different loop impedances at the desired frequency range means wider codomain of transformation and is appropriate for the impedance measurement.

The second aspect is the property of the measurement instrument. As mentioned previously, VNAs have generally the disadvantage of a limited dynamic range and calibration problem. Although these effects cannot be removed completely, they can be reduced by averaging, reducing IF bandwidth. and performing a warm-up phase.

The third aspect is the de-embedding approach, i.e. removing the CT's frequency response from the raw measurement data. The focus in this chapter was on de-embedding based on the three-port model and reflection measurement. A perfect de-embedding removes the entire frequency response of the CT from the raw reflection data. However, several problems exist in realizing a perfect de-embedding:

- The first problem is that no direct de-embedding approach exists to remove a three-port network from a one-port network. Such de-embedding is commonly carried out by means of a single-ended to differential port conversion, which can affect the accuracy of the determined loop impedance.
- The second problem is the error related to the measurement-based modelling. The three-port model used as a de-embedding data is a result of a complex de-embedding procedure. Based on the considerations in Chapter 2, the de-embedding of the three-port model is prone to errors. These errors propagate through the measurement, modelling and de-embedding chain and affect the final inaccuracy.

The brute force method and the analysis of transfer impedance are promising tools to predict the strength and weakness of a CT at a certain frequency range. From the results in Section 3.3.2 and 3.3.3, the BCI probe F-140, CT1 and the entire SCT's with 1:1 turn ratio (except W2 due to the limited bandwidth) are appropriate for the impedance measurement based on the reflection measurement up to 1 GHz. Conversely, the current probes F-36 and F-65 are definitely unemployable for the impedance measurement purposes based on reflection measurement.

4 Impedance Measurement with Current Transformers

In automotive electronic systems, the wiring harness is often assumed to be the main coupling path. During the ALSE and BCI tests, the coupled electromagnetic energy to the wiring harness produces an interference at the terminals of DUT and load simulator. The wiring harness prescribed for both methods is generally considered as a multiconductor transmission line (MTL) above a ground plane. Apart from the coupling mechanism of these test methods, the main variable components of the test setups are the terminal units. In line with the idea of reproducing the same interference current at terminal units with a BCI probe, accurate information about the input impedance of the DUT and load simulator (termination impedance) is from considerable significance. As mentioned earlier in this thesis, the terminal units are assumed to be linear. The definition of termination impedance and the scope of this thesis were given in Section 3.1. This chapter proposes and investigates four methods to characterize the magnitude and phase of termination impedances by means of current transformers (CT). The main focus remains on solving the problem for the specific case of a single-wire over a ground plane with two unknown termination impedances. Each method is analyzed separately based on a predefined impedance configuration. Limitations of the proposed methods to deal with the termination impedance matrices in case of wire bundles and a possible solution to break down the problem are given and discussed.

In this chapter, Section 4.1 formulates the BCI coupling by means of a simple transformer model for the general case of MTLs. Complexities and limitations of determining the termination impedances based on an inverse function are discussed. Section 4.2 to Section 4.5 describe four methods to determine the termination impedances including

- single probe method (SPM),
- double probe method (DPM),
- current distribution method (CDM),
- extended single probe method (ESPM).

In order to validate the proposed methods, three sample load configurations are chosen based on the common characteristic impedance of a wiring harness in immunity setups based on ISO 11452. Due to the appropriate physical proprieties and availability of BCI probe in BCI immunity test setups, it is used as the main CT in this chapter. As described in Chapter 3, other optimized CTs can also be used for this purpose.

4.1 Theoretical Formulation of the Problem

According to ISO 11452, the terminal units of the wiring harness include the DUT on one side and the load simulator on the other side. While the impedance of the artificial network is prescribed at least up to 100 MHz, the impedance of all other terminal units varies depend on the design and structure of the DUT and load simulator. The aim in this section is to formulate the relation between the output impedance of a CT around a wiring harness and the termination impedances by means of a simplified modelling of the coupling phenomenon.

4.1.1 Setting Up a System of Equations

Among different methods to model CTs in Chapter 3, a simplified form of the lumped parameter model is commonly used to describe the application of CTs to inject current into a wiring harness or to monitor the current flow [24]. The simplified model approximates the CT's behavior by using an inductively coupled circuit as illustrated in Figure 4.1. The effect of the termination impedances on the left and right side of the wiring harness can be incorporated by two $1 \times \mathrm{n}$ matrices $\mathbf{Z_L}$ and $\mathbf{Z_R}$.

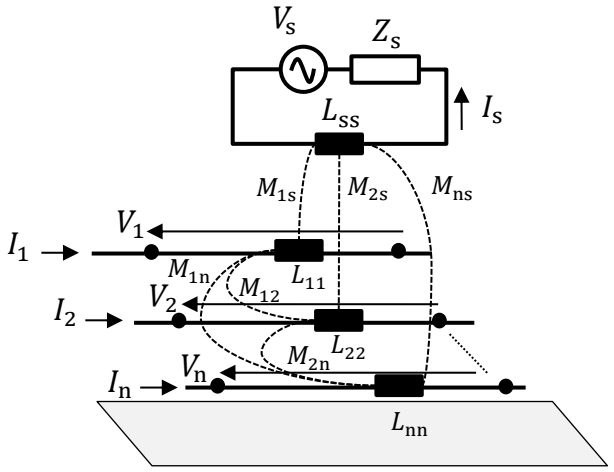

Figure 4.1: Equivalent model for an injection or monitoring CT around a MTL. The voltage source $\mathrm{V_S}$ in case of monitoring circuit is equal to zero ($\mathrm{V_S} = 0$)

The self inductance of the CT and the self inductance of each wire section are presented with L_{ss} and L_{ii}. The CT-to-wire and the wire-to-wire mutual inductances are presented with M_{is} and M_{ij}. The system of equations describing the inductively coupled model of a CT clamped around a MTL can be obtained by applying Kirchhoff's voltage law (KVL) for each wire section separately as follows

$$V_1 = j\omega(L_{11}I_1 - M_{12}I_2 - \cdots - M_{1\mathrm{n}}I_\mathrm{n} - M_{1\mathrm{s}}I_\mathrm{s}),$$

$$V_2 = j\omega(-M_{12}I_1 + L_{22}I_2 - \cdots - M_{2\mathrm{n}}I_\mathrm{n} - M_{2\mathrm{s}}I_\mathrm{s}),$$

$$\vdots \qquad (4.1)$$

$$V_{\mathrm{n}} = j\omega(-M_{1\mathrm{n}}I_1 - M_{2\mathrm{n}}I_1 - \cdots + L_{\mathrm{nn}}I_{\mathrm{n}} - M_{\mathrm{ns}}I_{\mathrm{s}}),$$

$$I_{\mathrm{s}} = (j\omega L_{\mathrm{ss}} + Z_{\mathrm{s}})^{-1}\big(V_{\mathrm{s}} + j\omega(M_{1\mathrm{s}}I_1 + M_{2\mathrm{s}}I_2 + \cdots + M_{\mathrm{ns}}I_{\mathrm{n}})\big),$$

where I_{s} indicates the current at the secondary winding of the CT. As described in Chapter 3, each clamped wire section can be considered as a separate primary winding and the loop impedance is defined as the impedance connected to the primary terminals. Figure 4.2 illustrates the simplification of a CT around a wiring harness. The self inductance and the cross coupling between the clamped conductors are not shown in this figure. Assuming a separate loop impedance for each winding, provides the possibility of relating the voltage across the clamped wire section to the loop impedance. Hence, substitution of the voltage across each clamped wire section i with the corresponding current I_i and loop impedance Z_{loop_i} in (4.1) result in a new system of equations as follows

$$\begin{aligned}
-Z_{\mathrm{loop}_1}I_1 &= j\omega(L_{11}I_1 - M_{12}I_2 - \cdots - M_{1\mathrm{n}}I_{\mathrm{n}} - M_{1\mathrm{s}}I_{\mathrm{s}}),\\
-Z_{\mathrm{loop}_2}I_2 &= j\omega(-M_{12}I_1 + L_{22}I_2 - \cdots - M_{2\mathrm{n}}I_{\mathrm{n}} - M_{2\mathrm{s}}I_{\mathrm{s}}),\\
&\vdots\\
-Z_{\mathrm{loop}_{\mathrm{n}}}I_{\mathrm{n}} &= j\omega(-M_{1\mathrm{n}}I_1 - M_{2\mathrm{n}}I_1 - \cdots + L_{\mathrm{nn}}I_{\mathrm{n}} - M_{\mathrm{ns}}I_{\mathrm{s}}),\\
Z_{\mathrm{out}}I_{\mathrm{s}} &= j\omega(-M_{1\mathrm{s}}I_1 - M_{2\mathrm{s}}I_2 - \cdots - M_{\mathrm{ns}}I_n + L_{\mathrm{ss}}I_{\mathrm{s}}),
\end{aligned} \tag{4.2}$$

where Z_{out} indicates the impedance measured at the connector port of the CT (output impedance). The entire self- and mutual inductances are the inherent characteristics of the CT-MTL network and can be measured or calculated based on the setup configuration as given in Chapter 3.

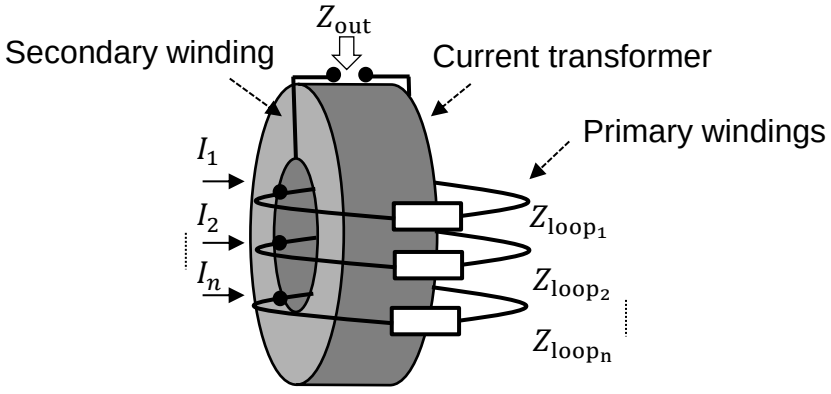

Figure 4.2: Simplified structure of a CT clamped around multiple primary windings to relate the loop impedance to the output impedance

Based on (4.2), if the entire self- and mutual inductances are known, a single impedance measurement at the connector port of a CT clamped around a MTL result in

an underdetermined system of $n+1$ equations, where the entire currents and loop impedances are unknown.

4.1.2 Solution of the Inverse Problem

In case of a single wire as the primary winding, solving (4.2) for Z_{out} yields

$$Z_{\mathrm{out}} = j\omega L_{\mathrm{ss}} + \frac{\omega^2 M_{1\mathrm{s}}^2}{Z_{\mathrm{loop}_1} + j\omega L_{11}}. \tag{4.3}$$

This expression was derived for the output impedance in (3.16) based on the lumped parameter model for a primary winding with a single turn. The equation shows the impact of self inductance and the mutual inductance on the output impedance. The coupling between windings $M_{1\mathrm{s}}$ is the key parameter to relate the loop impedance and the output impedance together. Based on (4.3), approximation of the output impedance for high and low loop impedances is given by

$$Z_{\mathrm{out}} \approx j\omega L_{\mathrm{ss}} \tag{4.4}$$

and

$$Z_{\mathrm{out}} \approx j\omega \left(L_{\mathrm{ss}} - \frac{M_{1\mathrm{s}}^2}{L_{11}} \right) \tag{4.5}$$

respectively. Equation (4.5), can be further simplified by considering the coupling factor based on (3.15) as

$$Z_{\mathrm{out}} \approx \ j\omega(1-k^2)L_{\mathrm{ss}}. \tag{4.6}$$

Based on (4.6), in case of a full coupling, i.e. $k=1$, the output impedance for a short circuit condition will be equal to zero. Similar to Section 3.3.2, equations (4.4) and (4.6) can be considered as the boundaries for the possible output impedances and give a comprehensive overview of the transformation codomain, where the output impedances are constrained to fall. According to (4.4) and (4.6), depending on the known loop impedance, the output impedance can be determined. However, the actual problem is an inverse problem, where a measured output impedance has to be used to determine the termination impedances at the wire ends. The intermediate parameter to relate the termination impedances and output impedance is the loop impedance. Solving (4.3) for Z_{loop_1} yields

$$Z_{\mathrm{loop}_1} = -j\omega L_{11} + \frac{\omega^2 M_{1\mathrm{s}}^2}{Z_{\mathrm{out}} - j\omega L_{\mathrm{ss}}}. \tag{4.7}$$

This equation shows that the loop impedance can be calculated directly in terms of the output impedance. For this purpose, the self inductance of the primary and secondary side and the mutual inductance must be known. Equation (4.3) and (4.7) describe the

behavior of a perfect impedance probe and the required information to measure the loop impedance from the output impedance. Nevertheless, the parasitic effects such as the CT's connector and capacitive couplings between different metallic structures add other variables to this equation.

From another point of view, the termination impedances can be related to the loop impedance based on the impedance transformation as illustrated in Figure 4.3. Based on transmission line theory, the loop impedance at a certain point along the wire can be considered as the sum of both termination impedances transformed from their origin at wire ends to this point. This concept can be expressed with

$$Z_{\mathrm{loop}_1} = Z'_{\mathrm{L1}} + Z'_{\mathrm{R1}} = \frac{V_{\mathrm{p1}}}{I_1} - Z_{\mathrm{ins}_1}, \tag{4.8}$$

where V_{p1} is an equivalent voltage source representing the excitation and Z_{ins_1} represents the insertion impedance of the CT. The apostrophe symbols indicate the transformed impedances to the position of the CT [49].

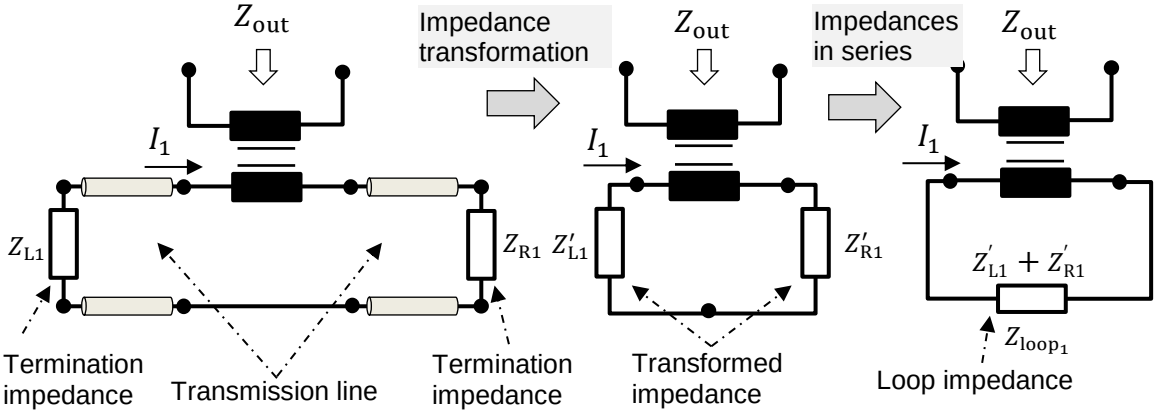

Figure 4.3: Relating the termination impedances to the loop impedance according to the transmission line theory and impedance transformation

According to transmission line theory, the transformation of the impedance Z along a line of length l is given with

$$Z' = Z_{\mathrm{c}} \frac{Z + Z_{\mathrm{c}} \tanh(\gamma l)}{Z_{\mathrm{c}} + Z \tanh(\gamma l)}, \tag{4.9}$$

where Z_{c} and γ refer to the characteristic impedance and the propagation constant of the transmission line. Substituting both transformed impedances Z'_{L1} and Z'_{R1} in (4.8) relates the impedances on the left and right side of the single wire with the loop impedance as follows

$$Z_{\mathrm{loop}_1} = Z_{\mathrm{c}} \left(\frac{Z_{\mathrm{L1}} + Z_{\mathrm{c}} \tanh(\gamma l_{\mathrm{L}})}{Z_{\mathrm{c}} + Z_{\mathrm{L1}} \tanh(\gamma l_{\mathrm{L}})} + \frac{Z_{\mathrm{R1}} + Z_{\mathrm{c}} \tanh(\gamma l_{\mathrm{R}})}{Z_{\mathrm{c}} + Z_{\mathrm{R1}} \tanh(\gamma l_{\mathrm{R}})} \right), \tag{4.10}$$

where l_{L} and l_{R} indicate the length between the CT and the wire end at left- and right side respectively. From the comparison between (4.3) and (4.10) it can be concluded that at least another measurement at a new position along the wiring is required to solve the equation for Z_{L1} and Z_{R1}. By assuming both Z_{loop_1} and Z_{loop_2} as known values obtained from two successive output impedance measurements, the problem can be formulated in terms of a system of two nonlinear equations as follows

$$\begin{cases} Z_{\mathrm{loop}_1} = Z'_{\mathrm{L,p1}} + Z'_{\mathrm{R,p1}} \\ Z_{\mathrm{loop}_2} = Z'_{\mathrm{L,p2}} + Z'_{\mathrm{R,p2}} \end{cases}, \tag{4.11}$$

where the subscript p1 and p2 indicate the first and second CT's position. Similar to (4.10), the transformed impedances in (4.11) should be expanded to relate the loop impedances to the termination impedances at the wire ends. Consequently, the termination impedances can be calculated by solving the system of equations for each frequency. In general, (4.11) can be expanded by performing the measurement at different locations along the wiring. However, the periodical characteristic of the hyperbolic tangent function $\tanh$ can lead to multiple solutions. Basically, the hyperbolic tangent function is defined over the whole complex plane and is a periodic function with the period $j\pi$. This means that the value of the loop impedance repeats periodically from the first measurement in distances d, where $d = jk\pi/\gamma$. In case of a lossless transmission line, the propagation constant can be related directly to the wavelength with

$$\gamma = j\beta = j\frac{2\pi}{\lambda}, \tag{4.12}$$

where β is the phase constant. Hence, the distance between two measurements is not allowed to be multiples of a half wavelength, as it leads to a dependent system of equations. Due to the structure of (4.11), the problem can be considered as a complex system of polynomial equations if the second measurement is performed at any location except for multiples of a half wavelength. The solution can be calculated algebraic or numerically.

In case of MTLs, the output impedance can be calculated directly based on (4.2), if the loop impedances are known (see Figure 4.2). Although the output impedance is directly given based on the loop impedances, there is now way to calculate each loop impedance directly from the output impedance. This problem can also be explained in terms of the CM current. According to [99], the CM current is defined as the sum of all currents in the wiring harness returning back through the ground plane. Conversely, there is no unique definition for the CM impedance. Based on the definition of the CM current, the CM impedance could be interpreted as the impedance between the ground plane and a common node, where all transmission lines are shortened. However, such definition is controversial, due to its irrelevance for practical purposes. Measuring the CM current reveals only the summation of all currents flowing at wires and there is no

way to separate the currents from each other. In case of a single wire at primary, the CM current and the actual current on the wire are equivalent. As given in (4.8), the loop impedance can be calculated by measuring the current I_1. The calculated loop impedance can then be related to the termination impedances based on impedance transformation based on (4.10). Conversely, in case of multiple wires at primary, substituting I_1 with the CM currents I_{CM} in (4.8) does not calculate the loop impedance of each wire. However, based on the abovementioned interpretation of the CM impedance, if all wire ends at each side are shortened to a common node, the measured CM current can be used to calculate the CM termination impedances.

A possible approach to solve the problem is to break down the original problem into the simplest possible form, i.e. a single wire over ground structure. For this purpose, the loop impedance can be obtained by clamping the CT around each wire separately to obtain the termination impedances on both sides of the wire. In this way, the loop impedance can be determined individually and the solutions to the sub-problems can then be combined to give a solution to the original problem. Furthermore, as mentioned at the beginning of this chapter, the same approach can be used to determine the impedance against the common mode interference signal, which is the dominant propagation mode in immunity tests. For this purpose, the common mode characteristic impedance and propagation constant of the wiring harness can be used as substitutes for the corresponding parameters in (4.10).

4.2 Single Probe Method

The most straightforward method to determine the loop impedance is to measure the one-port S-parameter or the impedance at the connector port of a CT clamped around the wiring harness. In general, a VNA determines the complex reflection coefficient at the network's terminals by measuring the ratio of the incident signal to the reflected signal from the network. The primary objective of the single probe method (SPM) is to determine the loop impedance by removing the frequency response of the CT from a measured reflection coefficient at the connector port of the CT. The final objective is to calculate the complex termination impedance separately based on impedance transformation.

4.2.1 Method Description

A BCI probe is clamped around a single wire over a ground plane. The wire ends are terminated to the ground with two impedances. The BCI probe is connected to the VNA port to measure the S-parameter (reflection coefficient) in the desired frequency range. According to the results given in Section 3.2.1 and 4.1, the direct one-port S-parameter measurement S_{m1} (reflection coefficient) is significantly affected by the frequency response of the BCI probe, which must be removed with a de-embedding process. In accordance with the de-embedding process described in Section 2.2.1, the

entire setup is considered as a cascaded network including the two-port BCI coupling attached to the loop impedance as shown in Figure 4.4. Thus, the first step is to reshape and convert the measured one-port S-parameter S_{m1} and the BCI coupling model.

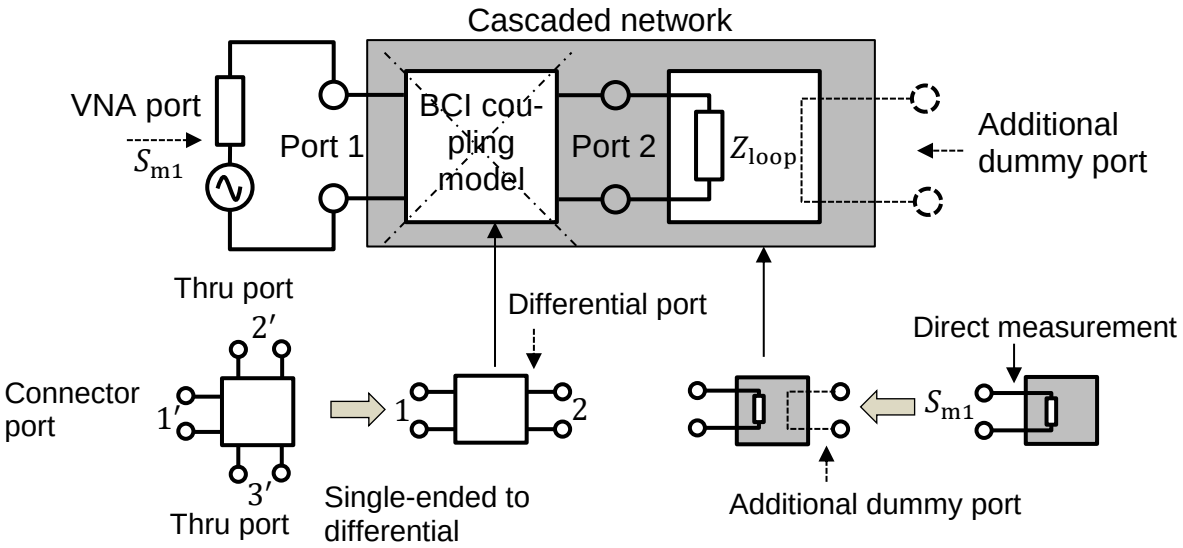

Figure 4.4: Expansion of a one-port S-parameter measurement to a two-port S-parameter matrix to facilitate the deembedding process

The result of the approach proposed in Section 3.2 is a three-port single-ended network. In order to multiply both matrices given by (2.10) for the purpose of de-embedding, the thru ports of the BCI coupling model are converted to a differential port. According to [100] and [101], the reflection coefficients of the new two-port model, S_{11} and S_{22}, are given by

$$S_{11} = S'_{11}, \qquad S_{22} = \frac{1}{2}\,(S'_{22} - S'_{23} - S'_{32} + S'_{33}), \tag{4.13}$$

and the transmission coefficients, S_{12} and S_{21}, are given by

$$S_{12} = \frac{1}{\sqrt{2}}\,(S'_{12} - S'_{13}), \qquad S_{21} = \frac{1}{\sqrt{2}}\,(S'_{21} - S'_{31}), \tag{4.14}$$

where the apostrophe symbol denotes the entries of the extracted three-port BCI model. Alternatively, it may be desirable to obtain the two-port coupling model in a direct process to avoid the complexities related to the three-port modelling process. For this purpose, a calibration setup similar to Figure 4.5(a) is proposed to measure the desired data immediately. The calibration setup is composed of a 7 cm wire, which is soldered between two metallic fixtures located upon a ground plane. The first and the second ports are connected to the VNA. The third port is shortened to the ground with a SMA short-circuit cap to emulate the differential feeding condition, despite the

added parasitic inductance due to the length of the wire. The measured two-port S-parameters can act as the desired two-port BCI coupling model.

The comparison between the directly measured two-port network and the coupling model obtained from the de-embedding is shown in Figure 4.5(b). Despite various parasitic couplings especially at higher frequencies, both datasets show a very similar trend up 1 GHz. Expanding the one-port S-parameter measurement S_{m1} to match the desired 2×2 matrix representation without affecting the actual signal flow is carried out by adding a dummy port to form a two-port network as illustrated in Figure 4.4. The two-port S-parameter matrix $\mathbf{S_m}$ describing the signal flow in this network is given by

$$\mathbf{S_m} = \begin{pmatrix} S_{\mathrm{m1}} & 0 \\ 0 & -1 \end{pmatrix}, \tag{4.15}$$

where both zero entries indicate that no coupling occurs between the ports. The short-circuit between terminals of the second port is presented with -1.

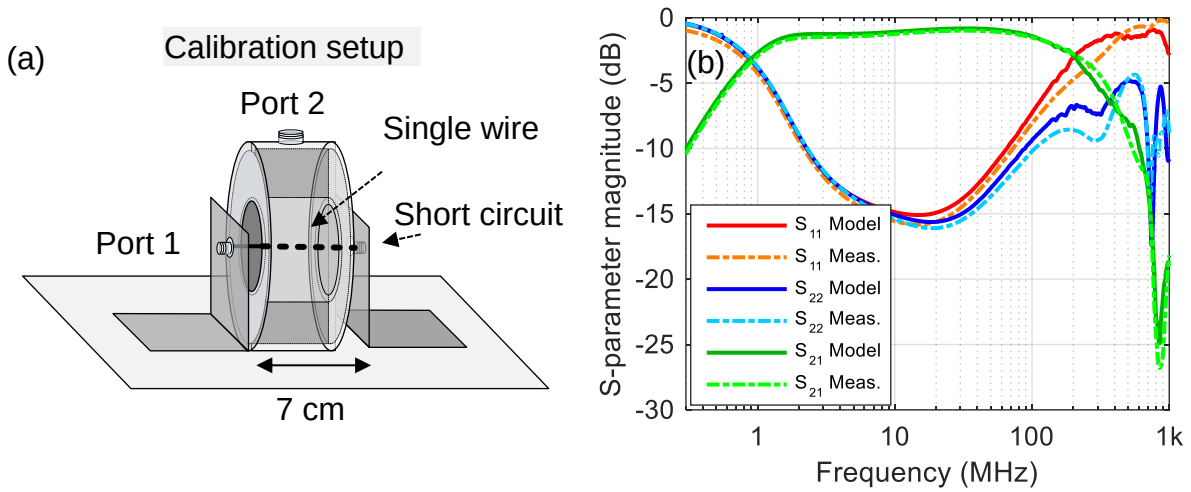

Figure 4.5: Calibration setup to measure the de-embedding data (a), comparison between the two-port S-parameter measured directly and extracted from three-port model after mode conversion (b)

According to (2.10) and the structure of the cascaded network in Figure 4.4, the T-parameter of the loop $\mathbf{T_{loop}}$ can be determined by

$$\mathbf{T_{loop}} = \mathbf{T_{BCI}^{-1}} \mathbf{T_m}, \tag{4.16}$$

where the matrix $\mathbf{T_{BCI}}$ represents the T-parameter of the coupling model. The matrix $\mathbf{T_m}$ represents the T-parameter of the expanded reflection measurement. Finally, the loop impedance is calculated by converting the matrix $\mathbf{T_{loop}}$ back to the Z-parameter and removing the entries related to the dummy port. As described in Section 4.1.2, calculating the impedances at the left- and the right side of the wire ends requires at least two measurements at different locations along the wiring.

4.2.2 Experimental Results

In order to assess the single probe method, a single wire of length $l = 1.7\ \mathrm{m}$ is spanned within two fixtures at height $h = 5\ \mathrm{cm}$ above a ground plane. The main structure of the setup is illustrated in Figure 4.6. Three load configurations are implemented based on the characteristic impedance of the wire ($Z_\mathrm{c} = 337\ \Omega$). The low frequency impedances of the terminal units are $Z_\mathrm{c}/33$, $Z_\mathrm{c}/10$, Z_c and $10Z_\mathrm{c}$. Each terminal unit consists of an SMD resistor soldered between the pin and the body of the a short SMA male connector. The load configurations are given in Table 4.1.

	Z_L	Z_R
Setup I	$Z_\mathrm{c}/33$	$Z_\mathrm{c}/10$
Setup II	$Z_\mathrm{c}/33$	Z_c
Setup III	$Z_\mathrm{c}/33$	$10Z_\mathrm{c}$

Table 4.1: Sample load configurations implemented in three setups for validation

The left end is terminated with $Z_\mathrm{L} = Z_\mathrm{c}/33$ and remains unchanged at each setup. The right end is terminated with $Z_\mathrm{c}/10$, Z_c and $10Z_\mathrm{c}$. The Agilent E5061B VNA and the BCI probe FCC F-140 are chosen for the measurement. The VNA is calibrated with a standard calibration kit prior to the measurement. The measurement cable between the VNA and the probe is equipped with several snap ferrites to suppress the CM current.

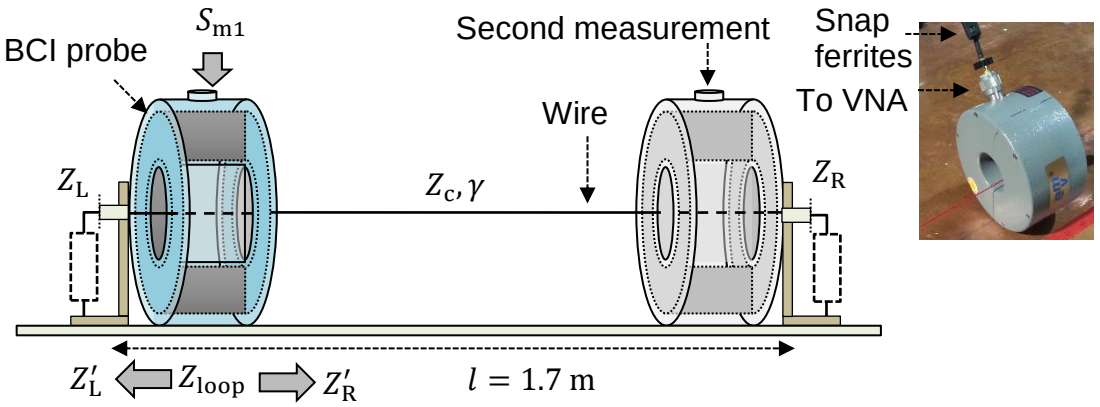

Figure 4.6: Measuring the one-port S-parameter S_{m1} at different locations along the wire to obtain the loop impedance with the single probe method

In the beginning, the reflection coefficient is measured using the BCI probe, located next to the left side of the setup. As discussed in the previous section, at least another measurement is necessary to determine each impedance separately. The gray colored BCI probe in Figure 4.6 represents the second measurement for this purpose. The raw measured data is expanded to obtain a two-port network as given in (4.15). The three-port model of the BCI probe obtained prior to this measurement, is used to calculate the loop impedance according to (4.16). Figure 4.7 shows the direct measured loop impedances for all three setup configurations and the theoretical values expected for the loop impedance at this point.

The expected value of loop impedance is calculated with (4.10) based on the termination impedances measured directly with the VNA. The expected values are the sum of the termination impedance on the right side according to Table 4.1, which are transformed along the transmission line of length $l_{\mathrm{R}} = 1.63\ \mathrm{m}$ and the termination impedance at left side without transformation ($l_{\mathrm{L}} = 0\ \mathrm{m}$). Moreover, the effect of test fixtures is incorporated at this step by correcting the directly measured termination impedances with additional LC circuit representing this effect. Basically, the exact values of these parasitic components are unknown. However, a good estimation can be given based on Section 2.2.2. Otherwise, the effect of fixtures has to be de-embedded from the final results.

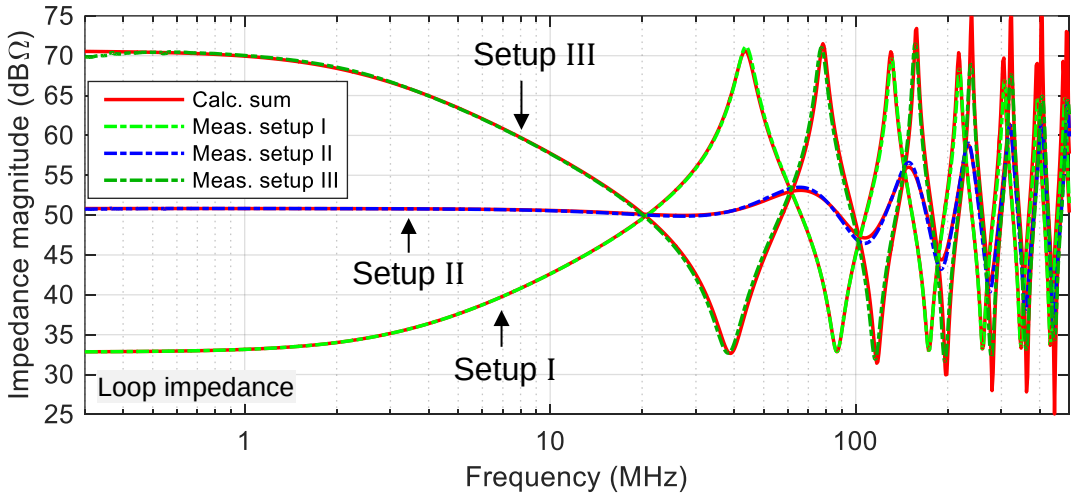

Figure 4.7: Comparison between the measured loop impedance with single probe method and the sum of the transformed termination impedances to the measurement point at the left side of the setup

Overall, the comparison between the results shows a very good agreement for all three setups up to 500 MHz. The resonance frequencies are caused by the mismatch between the transmission line and terminal units. Even in setup II, where the difference between the characteristic impedance and termination impedances is small at low frequencies, the parasitic effects at wire ends lead to several resonances above 30 MHz. The small deviations between the measured and expected values in Figure 4.7 are caused by

- inaccuracies originate from the extracted three-port model of the BCI probe and de-embedding approach,
- lower dynamic of the measurement instrument for low and high load impedances,
- parasitic inductive and capacitive effects especially near the wire ends and near the BCI probe,
- measurement uncertainties of reflection measurement.

As mentioned earlier, the loop impedance acts as the intermediate value to relate the output impedance to the termination impedances. Any improvement in the measurement of the loop impedance can significantly affect the final results, i.e. individual termination impedances.

As explained in Section 4.1.2, in order to obtain the termination impedances separately, at least another reflection coefficient is required. Hence, the loop impedance is determined by locating the BCI probe next to the right end of the setup. In general, measuring the reflection coefficient can be repeated several times. Each measured loop impedance can be related to the termination impedances by means of (4.10). The result will be an overdetermined system of equations with two unknowns and can be solved with different numerical approaches.

The next step is to determine the impedances at each side separately by solving the system of equations based on (4.11). As discussed in previous section, there can be two solutions to this system of equation. However, only one of them corresponds to the actual problem. The knowledge of approximate termination impedance is thus necessary to choose the right answer. This can be obtained from a priori measurements of the load simulator or artificial network in absence of DUT. However, if the impedance at one side is known, only one loop impedance will be enough to calculate the other termination impedance.

The calculated results for the magnitude and phase of termination impedance on the right side are shown in Figure 4.8(a) and (b) up to 500 MHz. The impedance is also measured by connecting the load directly to the VNA in absence of the wire. Overall, the single probe method provides more accurate results at lower frequencies. It can be clearly seen that the calculated impedances show higher deviation over 100 MHz. The calculated results for the left termination shown in Figure 4.8(c) and (d) follow the same trend. As can be seen, the deviations from the directly measured value are more obvious in setup III. The deviation from the directly measured impedance increases with the increasing difference between the termination impedances. The results clearly indicate that the accuracy of the process is directly affected by the value of the loop impedance (intermediate value) and the length of the wire.

From the results can be concluded that generally, it is possible to calculate the termination impedances with the single probe method. However, the accuracy and practicability of this method are limited due to the systematic limitations or the limitations due to the accuracy of measurement. The first limitation is the calculation of the loop impedance as the intermediate value. As discussed in Section 3.3 and also shown in Figure 4.7, the dynamic of VNA to measure the impedance in combination with the CT and the ability of the proposed de-embedding approach to remove the frequency response play crucial roles in the overall accuracy. In order to set up a system of equations, at least two loop impedance values are required. Both intermediate values are

prone to errors, which will propagate to the final solution. The problem of measurement dynamic will be discussed in Section 4.2.2. Adding more number of reflection measurements along the wire result in an overdetermined system of equations, which can be used to improve the results.

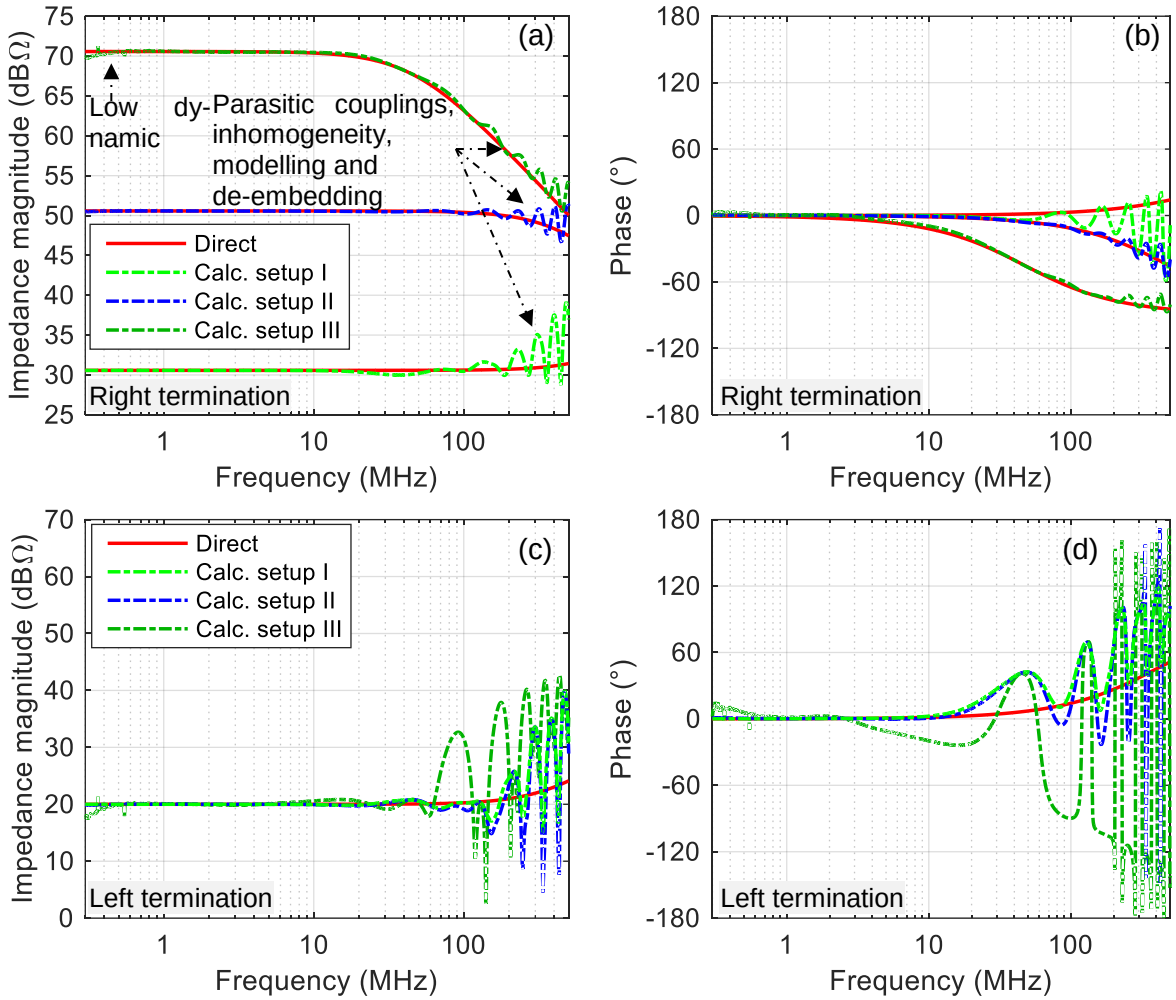

Figure 4.8: Calculation of the magnitude and phase of the termination impedances based on the measured loop impedances at two locations along the wire for three different load configurations. The directly measured magnitudes and phases are presented in red.

A possible solution to reduce the errors is to bypass the three-port modelling by calibrating the CT directly from reflection coefficients. For this purpose, the CT can be calibrated with a calibration jig attached to the temporary primary winding of very short length. The structure of the calibration setup is illustrated in Figure 4.9. In this case, the VNA that is connected to the CT, will measure the loop impedance directly. However, investigations in [50] report similar inaccuracies at higher frequencies due to the parasitic inductance of the temporary structure, limitations of VNAs and the mismatch between the calibration setup and the real test setup.

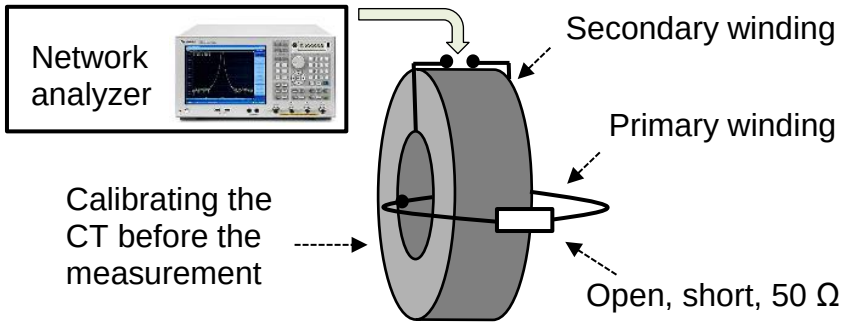

Figure 4.9: Calibrating a CT with a calibration jig before the reflection measurement to measure the loop impedance directly in the actual test setup

The second limitation is the calculation of termination impedance based on the solution to a system of equations. According to (4.10), the system of equations requires the exact value of the characteristic impedance and propagation constant to relate the loop and termination impedances together. Both of these values are considered in the system of equation as known and unique values, which can be calculated theoretically or based on the measurement-based model. However, in the real situation, they are affected by the inhomogeneous sections and parasitic couplings. For example, as discussed in Chapter 3, the loading effect of the BCI probe on the wire and the parasitic capacitive couplings between the BCI probe and unclamped section reduce the accuracy of the final solution. Furthermore, each setup consists of different modules including a BCI probe, wire and termination impedances. Setting up such a system of equations assumes an exact separation of these modules at the desired frequency. However, the validity of this assumption decreases with increasing frequency.

On the whole, from the entire results can be concluded that the single probe method is more appropriate to determine the loop impedance rather than termination impedances. Although this method is the most straightforward method to measure the impedance, both systematic limitations and limitations due to the measurement accuracy prevent its application for all test situations.

4.3 Double Probe Method

Applying two CTs to measure the impedance was initially developed and proposed for the frequency range between 20 kHz and 30 MHz [43]. Several succeeding studies extended the use of the so-called double probe method (DPM) up to 1 GHz by using CTs of a wider frequency bandwidth, more advanced measurement instruments and parametrically less sensitive model of the measurement structure [44-49]. In this section, the first objective is to determine the loop impedance using a BCI probe and a current probe. The final objective is to assess the possibility of calculating the complex termination impedance at each side of the setup separately based on solving a system of equations similar to the single probe method.

4.3.1 Method Description

In this method, a BCI probe and a current probe are clamped around a single wire over a ground plane. The BCI probe and the current probe are connected to the port 1 and port 2 of a VNA respectively to measure the S-parameters. The recorded two-port S-parameter data contains not only the impact of the loop impedance but also the frequency response of both CTs [48-49]. In order to determine the loop impedance with the double probe method, the measured S-parameter data is directly related to the loop impedance.

Figure 4.10(a) illustrates the schematic diagram representing the BCI probe (injection probe), the current probe (monitoring probe) and the loop impedance. Both 50 Ω resistors emulate the standard impedance of the VNA ports. The probes are located next to each other. Therefore, the injected current with the BCI probe and the monitored current can be assumed to be equivalent in magnitude and phase at low frequencies. The fix factors of the measurement at any point along the wire are the measuring probes. Thus, regardless of measuring probes, the monitored current is only a function of the loop impedance at this point. The schematic diagram can be further simplified by an equivalent voltage source V_s and the insertion impedances due to the loading effect of probes, $Z_{\mathrm{ins,BCI}}$ and $Z_{\mathrm{ins,CP}}$, as shown in Figure 4.10(b). In order to determine the loop impedance, the unknown variables acting independently from the setup, i.e. the BCI probe and current probe, are characterized in a calibration setup based on the method specified in [99].

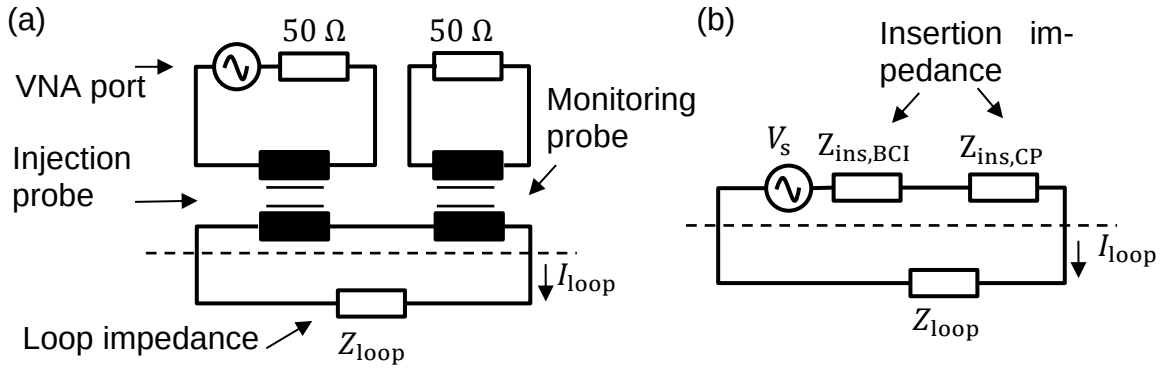

Figure 4.10: Schematic representation of the measurement structure (a), equivalent circuit including the equivalent source and insertion impedances (b).

The proposed calibration configuration is shown in Figure 4.11. Both probes are clamped around a single wire connected between two metallic fixtures. The single wire is shorted at one termination directly to the ground through a SMA short-circuit cap. Two other SMA termination caps including short and 50 Ω are used in the calibration procedure to build the final equation for the calculation of the loop impedance Z_{loop}. In order to simplify the final expression, the intermediate value S is defined as

$$S = \frac{S_{21}}{1 - S_{11}}, \tag{4.17}$$

where S_{11} and S_{21} represent the corresponding entries of a two-port S-parameter matrix. The loop impedance is then calculated using [49] with

$$Z_{\text{loop}} = 50\Omega \frac{S_{50\Omega}}{S_{\text{short}} - S_{50\Omega}} \left(\frac{S_{\text{short}}}{S_{\text{M}}} - 1 \right), \tag{4.18}$$

where S_{short} and $S_{50\Omega}$ are the calculated values of S for the case that the calibration setup is terminated with the standard SMA terminations, short and 50 Ω, respectively. The value S_{M} is the calculated value of S based on the two-port S-parameter measurement in the actual setup illustrated in Figure 4.12.

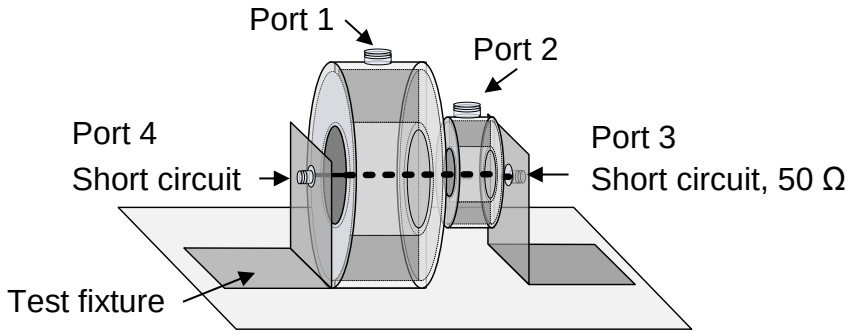

Figure 4.11: Calibration setup using a short wire and two SMA terminations to de-embed the frequency response of both probes from the S-parameter measurement

Similar to the single probe method, an independent system of equations is required to separate the termination impedances Z_{L} and Z_{R}. Such system can be obtained by changing the location of measuring probes along the wire, as illustrated in Figure 4.12. Additionally, the characteristic impedance and the propagation constant of the wire are necessary to relate the measured loop impedances to the termination impedances at the wire ends. Additionally, if one of the impedances is known, the other impedance can be calculated in a single measurement based on the impedance transformation. The same considerations as for the single probe method are valid regarding the number of loop impedance measurements along the wire.

4.3.2 Experimental Results

The measurement setup is illustrated in Figure 4.12. The same load configurations and setup as in the single probe method are used. The Agilent E5061B VNA, the BCI probe (FCC F-140) and the current probe (FCC F-65) are chosen for the measurement. The VNA is calibrated with a standard calibration kit prior to the measurement. Both measurement cables between the VNA and the probes are equipped with several snap ferrites to suppress the CM currents on the cable.

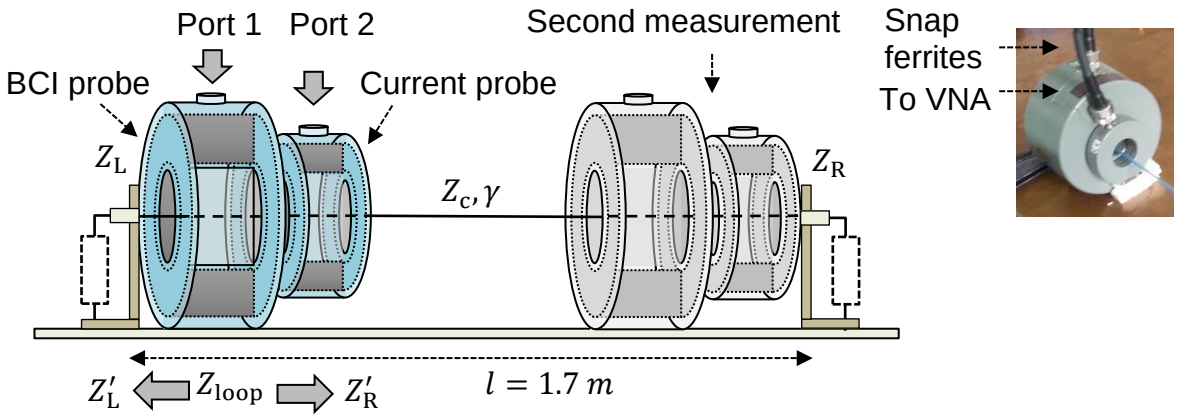

Figure 4.12: Measuring the two-port S-parameter data at different locations along the wire to obtain the loop impedance

In the beginning, the required two-port S-parameters are measured from the calibration setup. Following this, the BCI and current probe are located next to the left side of the setup to measure the two-port S-parameters from the setup. All three datasets are used to calculate the loop impedance based on (4.18).

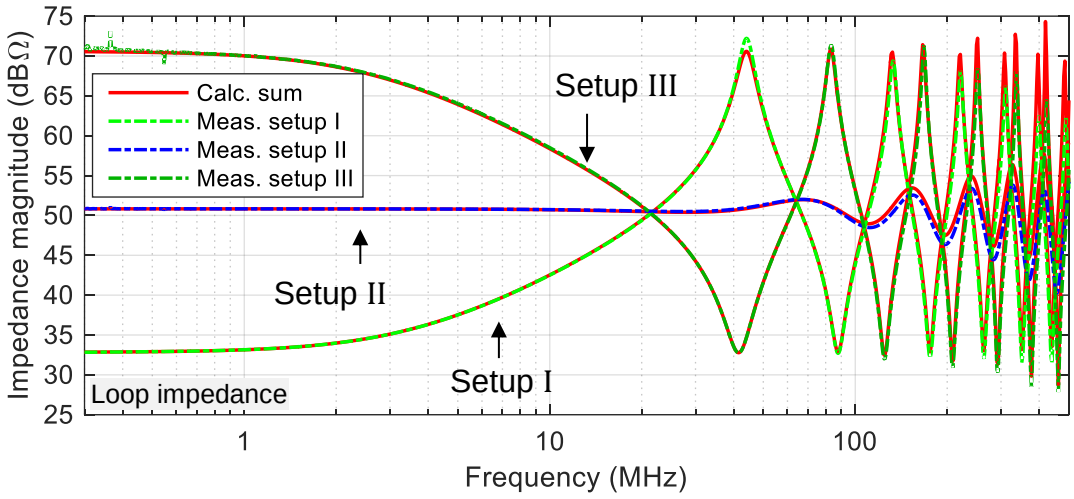

Figure 4.13: Comparison between the measured loop impedance with the double probe method and the sum of transformed termination impedance to the measurement point at the left side of the setup

Figure 4.13 shows the direct measured loop impedances for all three configurations and the theoretical values expected for the loop impedance at this point. Similar to the single probe method, the upper frequency is limited to 500 MHz and the expected value of loop impedance is calculated with (4.10) based on the termination impedances measured directly with the VNA. These values are the sum of the impedance on the right side transformed along the transmission line of length $l_R = 1.61$ m and the left impedance. The comparison between the results shows again a very good agreement. However, the deviations and the frequency shifting are higher than the single probe method. From the results, it can be concluded that the double probe method can also be used to measure the loop impedance.

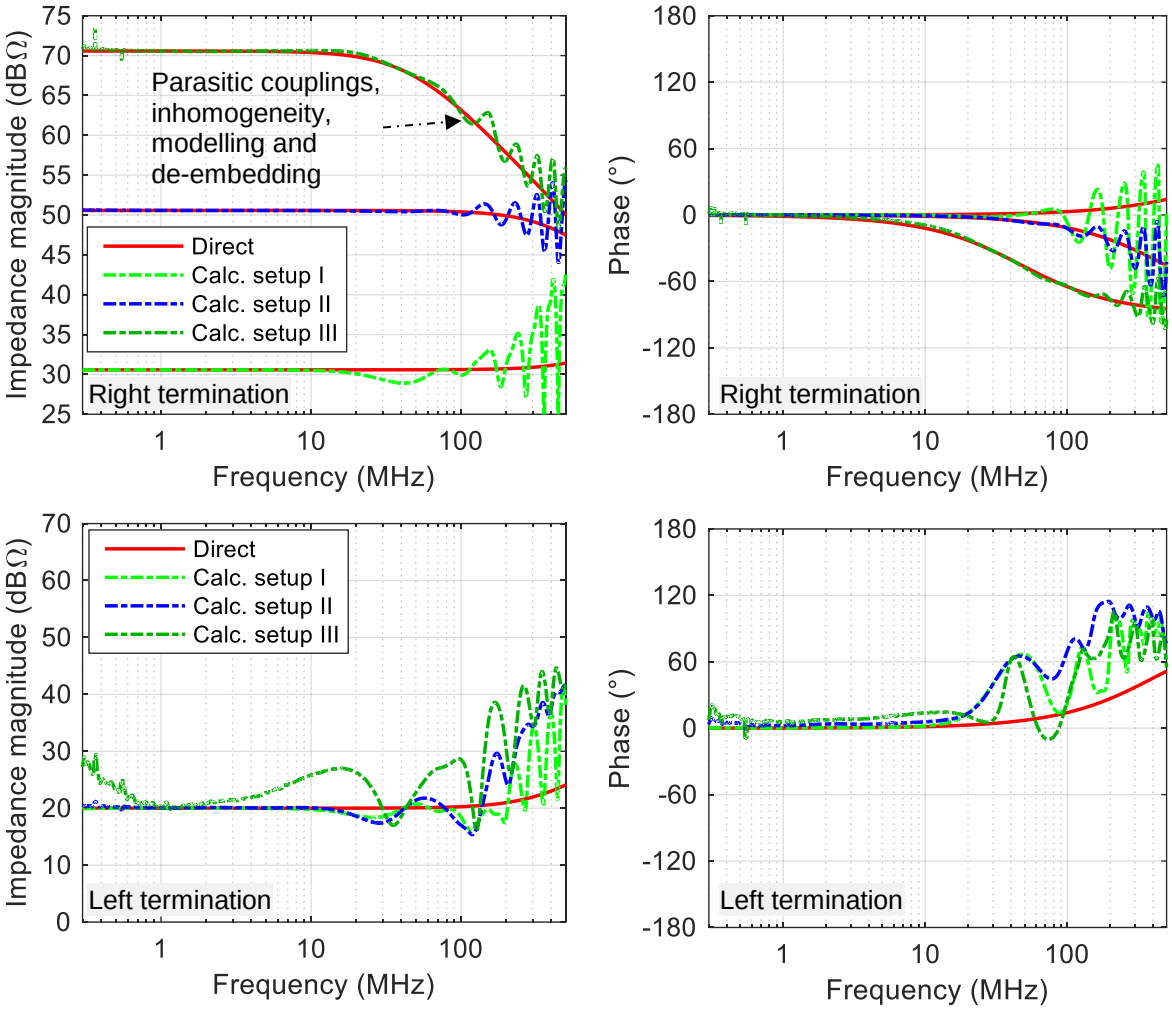

Figure 4.14: Calculation of the magnitude and phase of the termination impedances based on the measured loop impedances at two locations along the wire for three different load configurations. The directly measured magnitudes and phases are presented in red.

The next step is to determine the impedances at each side separately by solving the system of equations or by enforcing the known value at one side. The calculated results for the magnitude and phase of the termination impedance are shown in Figure 4.14. The behavior of all three load configurations is similar to the single probe method.

As discussed in Section 4.2.2, the reason behind the deviations have different sources of origin. One important aspect is a mismatched termination. If there is a mismatch of termination impedance, the standing waves will be inevitable and the loop impedance will have several maxima and minima based on the frequency and line length. The problem can be explained by assuming both CTs to be positioned next to an open circuit at the left side end, i.e. $Z_L = \infty$. According to (4.10), the loop impedance at the measurement point is the sum of both termination impedances transformed to this point. Thus, the loop impedance at this point will be infinite, regardless of the impedance at the right side. Based on (4.12), this situation repeats periodically from the first measurement in multiples of a half-wavelength. Therefore, measuring the other

termination at all of these points will be impossible. Similar situation can occur due to the transformation of the impedance at the right side. For instance, according to (4.10), if $Z_{\mathrm{R}} = 0$, the loop impedance is infinite again at distances from the load that are odd multiples of a quarter-wavelength. In a more general manner, in case of mismatch terminations, i.e. $Z_{\mathrm{R}} \neq Z_{\mathrm{c}}$ or $Z_{\mathrm{L}} \neq Z_{\mathrm{c}}$, very high loop impedance values can occur in the measurement point due to impedance transformation. As discussed earlier, the dynamic range of the VNA to measure high and low loads directly affects the loop impedance measurement with CTs even in case of an ideal transformer. The problem is intensified if the CT has a higher impedance ratio. Consequently, calculation of each termination impedance based on inaccurate intermediate value (loop impedance) will result in deviations. This situation is similar in case of single probe method and double probe method. Moreover, the other reasons for the deviations between directly measured and calculated impedances shown in Figure 4.14 are

- the parasitic elements due to the structure of calibration setup and the length of calibration loop,
- simple transformer model used to develop a calibration procedure,
- parasitic inductive and capacitive elements near the wire ends and between probes.

The main advantage of this method compared to the single probe method is that there is no need to extract a three-port model of the CT and the calibration data is obtained based on direct measurements. However, the calibration setup itself is a source of inaccuracy. The parasitic capacitance between metallic elements (probes and fixtures) and the self inductance of the wire downgrade the quality of the calibration compared to an ideal short or 50 Ω. For example, since even some millimeters of wire introduce an inductance of some nano-Henry, this impedance cannot be ignored at higher frequencies. Further improvements in the calibration procedure are needed for achieving better results for the frequency range above 100 MHz.

Furthermore, as mentioned previously the double probe method is based on the transformer model of probes. Thus, higher order effects of current probes such as parasitic capacitance between wire and probes, position of the wire within the CTs are not considered. These aspects need to be taken into account carefully with increasing frequency.

The final issue is the calculation of termination impedance based on the solution to a system of equations. As mentioned in Section 4.2.2, the system of equations requires the exact value of the characteristic impedance and propagation constant to relate the loop and termination impedances together. Similar complexities and limitations as with the single probe method due to the inhomogeneities and parasitic elements reduce the accuracy of the final results. On the whole, although the double probe

method is a fast and useful method to measure the loop impedance, calculation of the termination impedances is significantly affected by different sources of errors.

4.4 Current Distribution Method

As described in Section 4.2 and 4.3, the loop impedance at a certain location along the wire over a ground plane can be measured from the S-parameters obtained by means of one or two CTs and a VNA. The termination impedances can then be calculated by solving a system of equations, which relates the loop impedances to the termination impedances based on impedance transformation. Conversely, the idea of current distribution method (CDM) is to relate the current magnitude distribution along the wire to the termination impedance at each wire end. The CDM, as indicated by its name, measures the distribution of the current along a single wire with a CT. The measured data is then used to calculate the termination impedance at each side separately. In this way, there will be no need to determine the loop impedance as an intermediate value and solve a system of equations to calculate each termination impedance.

4.4.1 Method Description

According to the transmission line theory, incorporating the terminal constraints Z_{L} and Z_{R} in the general solution of transmission lines gives an expression for the current as a function of position anywhere on the wire [65]. Basically, in the matched case, the magnitude of the current does not vary at all, but in the mismatched cases, the magnitude of the current varies with position. Figure 4.15 shows a sample current distribution along a wire of length $l = 1.7\ \mathrm{m}$ measured in a mismatched case. The current is injected by a BCI probe (FCC F-140) located close to the termination at the left side and measured with a current probe (FCC F-65).

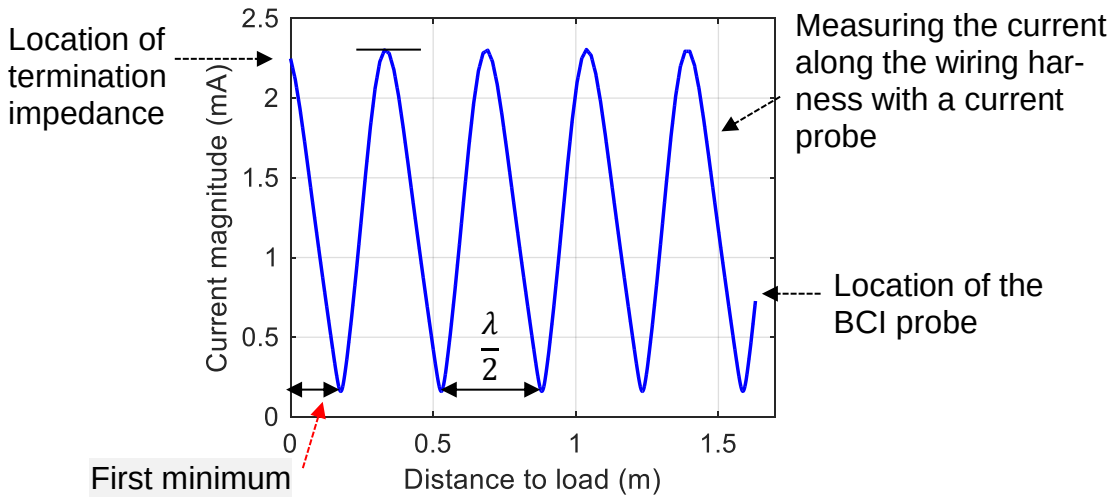

Figure 4.15: Sample current magnitude measured along a wiring of length $l = 1.7\ \mathrm{m}$ at 300 MHz in a mismatched case

From Figure 4.15 can be clearly seen that the maxima and minima are separated by one-quarter wavelength. Additionally, the corresponding points on the magnitude of the current are separated by one-half wavelength in distance. For a transmission line with known characteristic impedance Z_c and propagation constant γ, the ratio of the maximum current $|I_{max}|$ to the minimum $|I_{min}|$ current on the line can be used to determine the termination impedance at each side. The idea is to relate the standing wave ratio to the complex reflection coefficient. According to [102], the complex reflection coefficient Γ at the current minimum and the ratio between current maximum and minimum m are related by

$$\Gamma = \frac{1-m}{1+m}. \tag{4.19}$$

Based on transmission line theory, the reflection coefficient is directly related to the impedance at wire end. Thus, based on [102], the complex termination impedance can be directly calculated from the current distribution along a transmission line using impedance transformation as

$$Z_R = Z_c \frac{m - \tanh(\gamma l_{1min})}{1 - m\ \tanh(\gamma l_{1min})}, \tag{4.20}$$

where l_{1min} indicates the distance of the first current minimum from the end of wire, i.e. the distance to the node representing the termination impedance at the right side. For the calculation of the termination impedance on the left side Z_L, the process is repeated by locating the BCI probe on the right side and determining l_{1min} based on the new configuration. From (4.20) can be seen that the determination of termination impedances, similar to the single probe method and double probe method, is only possible if the characteristic impedance and the propagation constant of the transmission line are known.

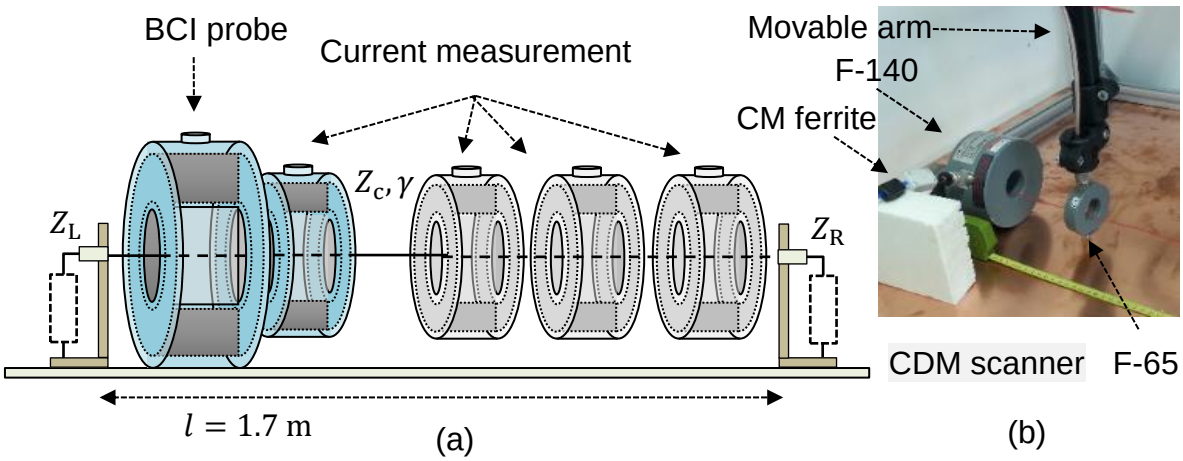

Figure 4.16: Application of the current distribution method along a wire to determine the impedance of terminations (a), automatization of the current measurement with a scanner to improve the accuracy of the measurement and to perform large number of successive measurements (b)

The structure of the measurement setup is shown in Figure 4.16(a). In order to measure the current distribution, a BCI probe can be connected to a signal generator to drive a current into the test setup. A monitoring current probe connected to a spectrum analyzer can then be used to measure the current magnitude in the specified distances from the BCI probe.

Alternatively, the current distribution measurement can be implemented by connecting the BCI probe and the current probe to the port 1 and the port 2 of a VNA respectively. In this case, the current is extracted from S-parameter measurement with

$$I = S_{21} \frac{\sqrt{P_{\mathrm{Fwd}} \cdot 50\ \Omega}}{Z_{\mathrm{T}}}, \tag{4.21}$$

where P_{Fwd} indicates the injected input power to drive the current into the circuit and Z_{T} represents the transfer impedance of the current probe. The S-parameter S_{21} is the transmission coefficient measured with the VNA. Thus, the current distribution can be directly calculated based on the successive S-parameter measurements along the wire, if the forward power and the transfer impedance of the current probe are known.

4.4.2 Experimental Results

As illustrated in Figure 4.16, the current distribution method is validated for three load configurations similar to the previous methods. The measurement is performed by means of a VNA E5061B. Both measurement cables between the probes and the VNA are calibrated prior to the measurement and equipped with CM ferrites.

In the beginning, the measurement of the current magnitude distribution along the wire is realized with a scanning procedure, wherein several successive measurements (scanning steps) record the current magnitude in the specified distances from each other. Measuring the current by moving the monitoring probe can be done manually, however, an automated current measurement with a scanner is preferable to save time and improve the accuracy. As illustrated in Figure 4.16(b), the current probe FCC F-65 is attached to a movable arm, which scans (measures) the transmission coefficients at predefined positions along the wire. A controlling unit including a Matlab program and a microcontroller is used to supervise the scanning steps and save the measured data for the frequency range between 300 kHz and 1 GHz. In order to achieve a trade-off between the accuracy and the measurement duration, the distance between two successive scanning steps is chosen as $d = 3\ \mathrm{cm}$.

Following this, the recorded data is processed in Matlab. The two-port S-parameter data is used to obtain the current distribution along the wire at each frequency separately based on (4.21). As given in (4.20), all required values including the position of the first minimum and the ratio of the current maximum and minimum are extracted from the data. The precision of $l_{1\mathrm{min}}$ has a significant impact on the accuracy of the

procedure. Therefore, the S-parameter data is interpolated from $3\ \mathrm{cm}$ to $0.5\ \mathrm{cm}$ to construct new data points within the range of the measured S-parameters using linear interpolation. The characteristic impedance and the propagation constant of the wire are extracted from the two-port S-parameter measurements in absence of both CTs according to Section 2.2.2. The termination impedance is then calculated for each frequency based on (4.20) using the measured values.

Figure 4.17(a) and (b) show the magnitude and phase of the calculated termination impedance on the right side for all three configurations. Overall, the calculated impedance shows a very good agreement with the directly measured impedances for all setup configurations above 50 MHz. In order to determine the termination impedance at the left side, the BCI probe is located adjacent to the left fixture and the current distribution method is repeated for each load configuration. The magnitude and phase of the calculated termination impedance on the left side is shown in Figure 4.17(c) and (d). In contrast to the previous methods, the results do not depend on the loop impedance or the ratio of termination impedances.

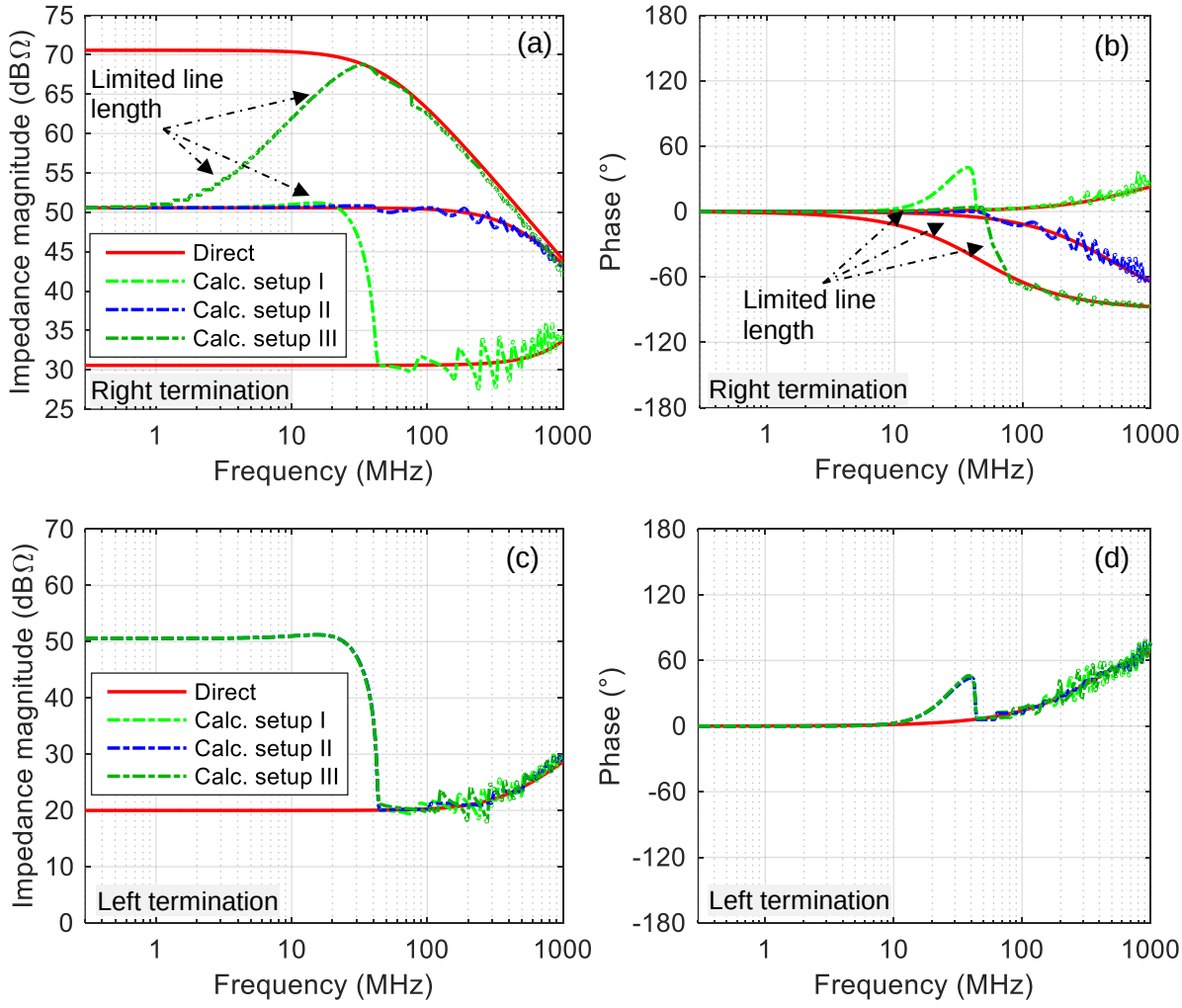

Figure 4.17: Calculation of the magnitude and phase of the termination impedances based on current distribution method

As mentioned previously, at least a wire of length quarter-wavelength is required to ensure that the scanning procedure finds at least one current minimum along the wire. According to transmission line theory, for instance, for a wire of length $l = 1.7\ \mathrm{m}$ prescribed in ISO 11452, the lowest frequency is approximately 44 MHz. This behavior can be directly seen for both magnitude and phase of the calculated results. To obtain the impedance at lower frequencies the length of the wire must be extended to match the lowest frequency.

Theoretically, the current distribution method calculates the exact value of the termination impedance. However, the differences between ideal the real situation lead to different errors, which propagate to final results. The sources of error can be classified in two categories. The first category comprises the errors related to (4.20). In order to calculate the termination impedance directly, the characteristic impedance and propagation constant of the wire are required. As mentioned before, the loading effect of both CTs and the inhomogeneity near metallic surfaces account for variety of parasitic effects, which are not comprised in (4.20). Consequently, using unique values for the characteristic impedance and propagation constant in (4.20) lead to errors at this step. The second category comprises the accuracy of the primary data and precision of the scanner procedure. The quality of the primary S-parameter measurement is affected by the measurement instrument, current probe and measurement cables. Although the measuring cables are calibrated before the measurement, successive movements of the current probe along the wire affect the quality of the measurement. Furthermore, the accuracy of estimated results is extremely sensitive to the current distribution resolution and the exact position of the current minima. Interpolating the data to find the exact position of the minimum can also affect the precision of the final results.

Although the high number of scanning steps and the low frequency limitation are the main disadvantages of this method, the capability of measuring each termination impedance separately without any knowledge of the other termination impedance is the main advantage of the current distribution method.

4.5 Extended Single Probe Method

As shown in the previous sections, the implementation and validation of the indirect impedance measurement requires different measurement, modelling and de-embedding steps. All these measurements and calculations inevitably involve uncertainties and errors, which propagate through all the calculation processes to the final results often in a complex manner. The ultimate goal in this chapter was to determine the complex termination impedances without disconnecting the terminal units from the wire. Regardless of the limitations concerning the measurement instrument, two dominant parasitic effects including the inhomogeneities and the loading effect of CTs on

the wire account for the main inaccuracies in the calculations. Incorporating these inhomogeneities and de-embedding unwanted effects not only require considerable time and effort but also introduce other elements of uncertainty in the calculations. In order to bypass these complexities and incorporate the entire components simultaneously, the wire-over-ground structure, the CT and the fixtures are assumed to be the unchanging factors of the measurement setup. Conversely, the terminal units are considered as the changing factor, which varies from a measurement setup to another. The extended single probe method (ESPM) proposed in this section incorporates the unchanging factor as a black box model. The goal is to directly relate the reflection coefficient measured with a VNA at the connector port of a CT to the complex termination impedances.

4.5.1 Method Description

As discussed in Chapter 2, the S-parameters of a network provide sufficient details about the reflections and the transmissions between different ports without having the knowledge of the internal structure of the setup. In line with this, the entire test setup in absence of the terminations circuits including the wire-over-ground structure, fixtures and the CT is considered as a three-port network. The signal flow diagram of such network is illustrated in Figure 4.18(a), where the values a and b indicate the incident and the reflected waves. Port 1 represents the CT's connector port. Port 2 and port 3 represent SMA connectors on the fixtures. In absence of terminal units, the S-parameters of this three-port network can be measured directly with a VNA to characterize the unchanging factor of the setup. Termination of port 2 and port 3 with loads prevents the access to these ports. Thus, only a reflection coefficient can be measured in this situation at the connector port of the CT as shown in Figure 4.18(b).

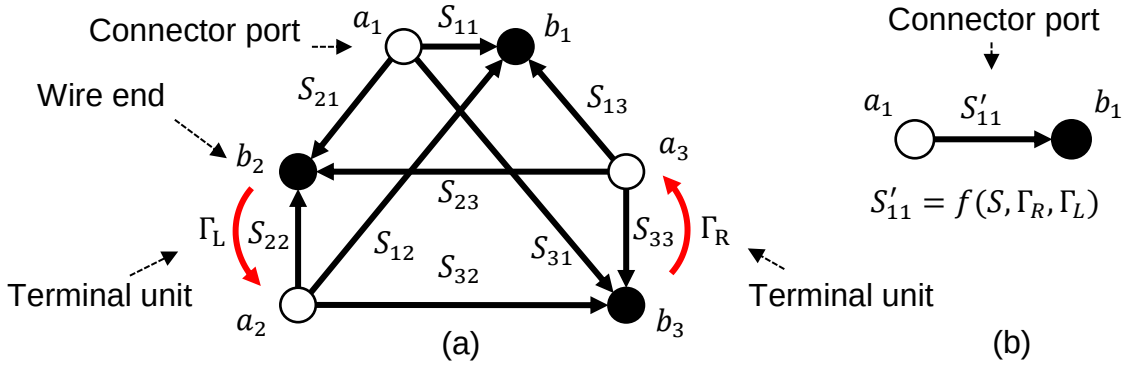

Figure 4.18: Signal flow diagram representing the entire test setup based on [1] and [2] (a), measured reflection coefficient at the CT's input port if the wire ends are terminated with arbitrary impedances (b)

Port 1 represents the CT's connector port. Port 2 and port 3 represent SMA connectors on the fixtures. In absence of terminal units, the S-parameters of this three-port network can be measured directly with a VNA to characterize the unchanging factor of the setup. Termination of port 2 and port 3 with loads prevent the access to these

ports. Thus, only the reflection coefficient can be measured in this situation at the connector port of the CT as shown in Figure 4.18(b).

The structure of the test setup is illustrated in Figure 4.19. The CT can be located at any point along the wire. To characterize the current situation, the three-port S-parameter matrix **S** is measured by connecting the VNA to the CT's connector port and the SMA connectors (calibration step). Variation of the CT's position leads to a new S-parameter matrix, which represents the new current signal flow between different ports. The general mathematical expression for the three-port S-parameter for any measurement was given in (2.4). Since both termination impedances are assumed to be unknown, at least two measurements are required. However, in order to avoid a dependent system of equations and improve the accuracy, the calibration step can be repeated at more locations along the wire.

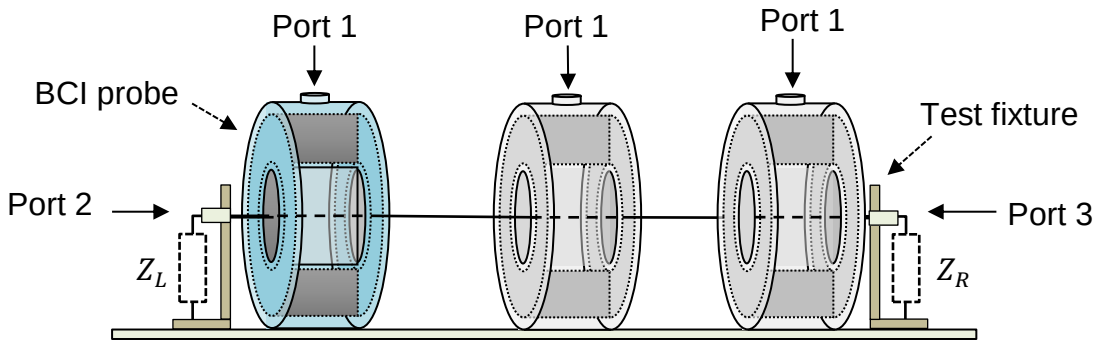

Figure 4.19: Measuring the three-port S-parameter data in absence of the termination impedances (calibration step) at different locations along the wiring

The second step is to perform a reflection measurement, while the SMA connectors are terminated with unknown loads, Z_{L} and Z_{R}. The location of the CT has to be exactly the same as during the calibration step. As illustrated in Figure 4.18(b), the measured reflection coefficient S'_{11} is a function of the three-port S-parameters **S** at a certain location and both reflections at the SMA connectors. Termination of both SMA connectors corresponds to add two secondary constraints into the system of equations given in (2.4) as follows

$$a_2 = \Gamma_{\mathrm{L}} b_2, \tag{4.22}$$

$$a_3 = \Gamma_{\mathrm{R}} b_3, \tag{4.23}$$

where Γ_{L} and Γ_{R} represent the reflection coefficients at the left side and the right side of the wire respectively. Any measurement set in this method includes two steps:

- three-port S-parameter calibration step,
- reflection measurement at the same location.

The difference between the reflection coefficients S_{11} and S'_{11} during each measurement set, is the result of the different terminations at the port 2 and 3. The termination constraints remain constant for each set of measurement. Substitution of (4.22) and (4.23) in (2.4) gives a general expression for the reflection coefficient S'_{11} as a function of the matrix **S** and the reflections at the terminations, Γ_{L} and Γ_{R}

$$f(\Gamma_{\mathrm{L}}, \Gamma_{\mathrm{R}}) = S'_{11} - \frac{S_{11} - \Gamma_{\mathrm{L}}(S_{11}S_{22} - S_{12}^2) - \Gamma_{\mathrm{R}}(S_{11}S_{33} - S_{13}^2) + \Gamma_{\mathrm{L}}\Gamma_{\mathrm{R}}(S_{11}S_{22}S_{33} - S_{11}S_{23}^2 - S_{33}S_{12}^2 + S_{12}S_{31}S_{23} + S_{13}S_{32}S_{21} - S_{22}S_{13}^2)}{1 - \Gamma_{\mathrm{L}}S_{22} - \Gamma_{\mathrm{R}}S_{33} + \Gamma_{\mathrm{L}}\Gamma_{\mathrm{R}}(S_{22}S_{33} - S_{23}^2)} \tag{4.24}$$

where S_{nn} represents the corresponding entry in the three-port S-parameter matrix **S**, which are obtained during the three-port measurement. Both reflection coefficients, Γ_{L} and Γ_{R}, are unknown. Therefore, at least another set of measurement is required to determine each reflection separately. However, as mentioned previously, the number of successive measurement can be improved to obtain more accurate results. Combination of the ESPM's measurement sets results in a system of nonlinear equations F, which can be solved for each frequency with a numerical approach such the method of least squares. The general form of F for sample measurement sets at three different locations is given with

$$F = 0 \Rightarrow \begin{cases} f_{\mathrm{m1}}(\Gamma_{\mathrm{L}}, \Gamma_{\mathrm{R}}) = 0 \\ f_{\mathrm{m2}}(\Gamma_{\mathrm{L}}, \Gamma_{\mathrm{R}}) = 0, \\ f_{\mathrm{m3}}(\Gamma_{\mathrm{L}}, \Gamma_{\mathrm{R}}) = 0 \end{cases} \tag{4.25}$$

where the subscripts m1, m2 and m3 indicate the function resulted from the first, second and third measurement sets.

4.5.2 Experimental Results

The same setup as for the previous methods is chosen for the validation of the ESPM. In the beginning, as illustrated in Figure 4.19, the BCI probe is located at three points along the wire including two locations close to both fixtures at the left and right end and a location in the middle of the wire. The three-port measurement is performed between 300 kHz and 1 GHz by connecting the port 1 to the BCI probe's connector port. Both other ports are connected to the SMA connectors mounted on the fixtures. Following this, the terminal units are connected to the fixtures and the reflection measurement is performed at the same locations as in the previous step. Finally, the system of nonlinear equations described in (4.25) is solved separately for each frequency to determine the termination impedances.

Figure 4.20 shows the direct measured termination impedances for all three load configurations and the calculated values based on the extended single probe method. The comparison between the results shows an excellent agreement even at higher

frequency range as all transformations are calibrated. From the results can be concluded that ESPM is very successful to remove to the entire frequency response of the setup (black box or the unchanging factor).

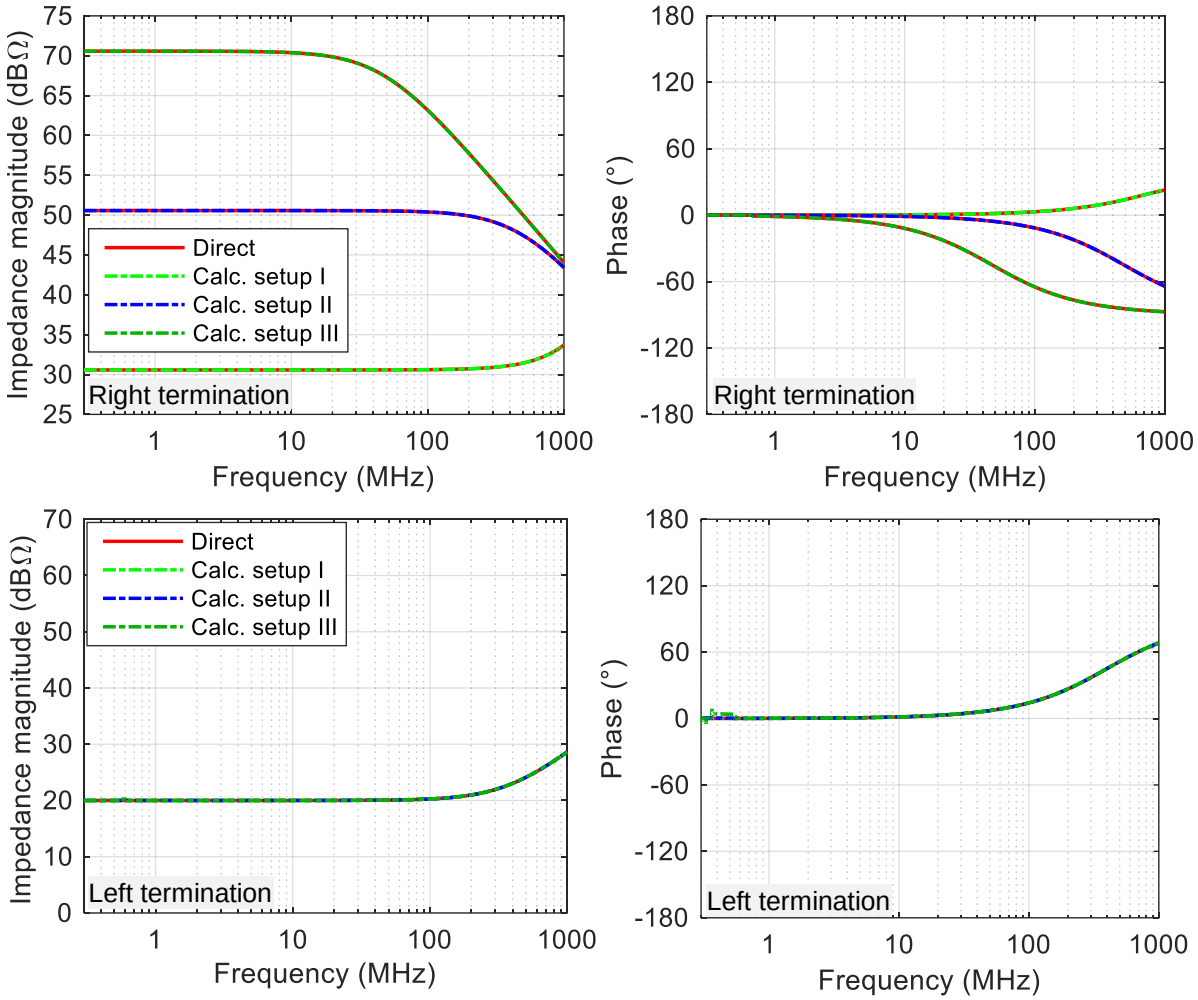

Figure 4.20: Calculation of the magnitude and phase of the termination impedances based on the extended single probe method performed at three locations along the wiring for three different load configurations. The directly measured magnitudes and phases are presented in red.

The main advantages of the extended single probe method are as follows:

- characterization of the characteristic impedance, propagation constant and the inhomogeneities are not required,
- no primary modelling or de-embedding process are required,
- there is no need to measure intermediate values such as loop impedance,
- both termination impedances are determined simultaneously.

However, the dynamic range of VNA measurement is the first limitation of the ESPM similar to the other proposed method. Although, the dynamic range can be increased by reducing noise floor through IF bandwidth reduction and averaging, each method has the disadvantages that they increase the complexity of measurement and has a

unique effect on measurement speed. Regardless of these methods, further improvement can be achieved by using the segmented sweep feature found in some network analyzers. The second limitation is that having access to the wire ends (port 2 and 3) is a critical aspect which may not be applicable in some test configurations. Relating the reflection coefficient measurement and the three-port measurement is the crucial step of the extended single probe method. Therefore, the applicability of the calibration step, i.e. measuring the three-port measurement, in absence of the terminal units must be examined in advance.

4.6 Summary of the Proposed Methods

In order to expand the BCI as a substitute for the ALSE, a detailed knowledge of the termination impedances is required. This chapter presented four methods to determine the magnitude and phase of termination impedances by means of current transformers including: single probe method (SPM), double probe method (DPM), current distribution method (CDM) and extended single probe method (ESPM). All four methods were experimentally validated in a real situation. An overview of the advantages and disadvantages of these methods is given in Table 4.2.

Method	Discussion
Single probe method	Advantages: • Only one CT is required • Simple reflection measurement with a VNA and a CT clamped around the wire • De-embedding of the CT's frequency response includes a simple matrix multiplication • Appropriate for the loop impedance measurement • Two measurements are sufficient to determine the termination impedances Disadvantages: • Complex three-port modelling is required for de-embedding • Loop impedance is related to termination impedances based on impedance transformation, which assumes unique characteristic impedance and propagation constant for transformation length despite inhomogeneities at different locations along the wire • Termination impedances can only be determined by solving a system of equations if both impedances are unknown • Several sources of error due to the measurement, modelling and de-embedding • Solution is very sensitive to small errors and shows resonances at high frequencies State of the art: • Measuring the impedance is possible. High accuracy is given up to 200 MHz.

Double probe method	Advantages: • De-embedding data is measured directly from the calibration setup • No primary modelling or de-embedding is required • Appropriate for the loop impedance measurement • Two measurements are sufficient to determine the termination impedances Disadvantages: • Low dynamic at low and high frequencies • Loop impedance is related to termination impedances based on impedance transformation, which assumes unique characteristic impedance and propagation constant for transformation length despite inhomogeneities at different locations along the wire • Parasitic capacitance and inductance elements in calibration setup • Solution is very sensitive to small errors and shows resonances at high frequencies State of the art: • Measuring the impedance is possible. High accuracy is given up to 100 MHz.
Current distribution method	Advantages: • Termination impedances are directly measured without calculating the loop impedance • No modelling or de-embedding is required • No phase information is required • Combination of a signal generator and a spectrum analyzer can be employed instead of a network analyzer to measure the current distribution • Similar performance for high and low termination impedances Disadvantages: • Low frequency limitation due to the limited wire length • High number of measurements to obtain the required current distribution • Data interpolation is required • Assuming a unique characteristic impedance and propagation constant to calculate termination impedance despite inhomogeneities at different locations along the wire • Very sensitive to inaccurate parameters involved in calculating the termination impedances State of the art: • Measuring the impedance is possible. High accuracy is given up to 1 GHz.
Extended single probe method	Advantages: • Very high accuracy • Exact separation between termination impedance and setup

	• No modelling and wire characterization are required • Termination impedances are directly measured without calculating the loop impedance or any intermediate parameter • Accuracy is limited only to the dynamic range of measurement device Disadvantages: • Several calibration and measurement steps are required • Any change to the wire structure invalidates the calibration measurements • Both wire ends have to be accessible to the network analyzer at the calibration step State of the art: • Measuring the impedance is possible. High accuracy is given up to 1 GHz.

Table 4.2: Overview of the non-invasive methods to measure the impedance using current transformers

The investigations in this chapter were limited to a setup structure from a single wire over a ground plane. As mentioned earlier in this chapter, a possible solution to overcome the limitations concerning wire bundles is to break down the original problem into a set of sub-problems. In this way, the impedance matrices at wire ends can be filled in a stepwise fashion by solving the problem for each wire separately.

5 Reproducing the ALSE Currents with a BCI Probe

Application of the ALSE method requires the generation and radiation of high field intensities. Due to security and environmental reasons, such radiated test must be performed in an anechoic chamber [1]. The financial aspect related to the required facilities and equipment, and often waiting times for the preparation and final testing are the major considerations to the potential users. Moreover, both calibration and testing are highly sensitive to small changes and prone to error. These problems have led to the suggestion of replacing ALSE with BCI in different publications. The idea that, the effects of a radiated test could be emulated by injecting currents generated with less power is very appealing, because it allows the users to achieve the same interference levels outside anechoic chambers with less effort and cost.

According to Section 2.2.4, the radiated fields generated during the ALSE testing can be considered as distributed sources along the entire wiring harness. Conversely, the BCI can be considered as a lumped voltage source located at a certain position along the wiring harness. Basically, reproducing the ALSE currents can be interpreted in two different ways. While the first concept investigates the possibility of obtaining the same current distribution along the entire wiring harness, the second concept focuses on enforcing equivalence only between the currents flowing into the terminal units attached to the harness ends. As mentioned earlier, different theoretical and experimental investigations including [3-11] prove that there is no general solution to this problem. In fact, unless for some exceptional cases, radiation and injection cannot be made equivalent due to different coupling mechanisms. Although any investigation to improve the correlation based on the first concept automatically comprises the second concept too, the first concept is still irrelevant from the immunity testing perspective and increases the complexity of the problem. Consequently, in line with the idea of improving the correlation between ALSE and BCI, the second concept is chosen in this work and the formulation of the problem is limited in a way that it is feasible and realizable in practical applications. For this purpose, the following assumptions have been made. The first and the most fundamental assumption, is that the DUT and load simulator are linear networks. The second is that several specific ports can be considered in terms of placement at harness ends, where the equivalency should to be established. These ports are terminated with loads, where the currents are of interest. As mentioned earlier in this work, the term “termination current” is used to indicate the current of interest. Due to the significant limitations and complexities given in [3-11], the investigation and application in this work is restricted to a single wire over ground structure. The developed procedure could be used as a possible solution to break down the problem for the general case of wire bundles, i.e. individually performing the test for each single wire among the wire bundle under test.

The main objective in this chapter is to develop a process to systematically search for the BCI conditions which result in similar or even identical interference levels at the terminal units as in the ALSE method. The proposed process combines the extracted ALSE and BCI coupling models in Chapter 2, and the indirect method of measuring the termination impedances with current transformers in Chapter 4. In this way, the models and impedances are used to determine the termination currents in a simulation environment and to find the best possible BCI conditions by means of an optimization process.

In the beginning of this chapter, the degrees of freedom are defined and the problem is formulated in terms of a system matrix. Following this, the limitations of using an analytical method to determine the correct BCI conditions is investigated and discussed. After this, application of a numerical method to solve the problem with an optimization function is presented and analyzed. Section 5.2 builds on the modelling procedure in Chapter 2, to reproduce the ALSE currents with a BCI probe and contains the experimental results. In Section 5.3, the limitations of the proposed process are given and discussed.

5.1 Determination of Feeding and Positioning Conditions

Degrees of freedom are often defined as the number of independently variable factors affecting the range of states in a system. These factors will be used in this section to achieve the same ALSE termination currents with a BCI probe. The degrees of freedom chosen from a typical BCI test setup are:

- injected power into the BCI probe (feeding condition),
- position of the BCI probe along the wiring harness (positioning condition).

The amount of the injected power is restricted to the ability of the available signal amplifier and the position of the BCI probe is restricted to a location between both boundaries of the wiring harness.

5.1.1 Application of Analytical Methods

As described in Chapter 4, the impact of an injection probe on a transmission line can be described in terms of an equivalent voltage source V_{s} and an equivalent insertion impedance Z_{ins}. Without the loss of generality, the primary investigation is carried out for a circuit structure composed of the equivalent circuit of an injection probe, a transmission line with known characteristic impedance Z_{c} and propagation constant γ, and two termination impedances Z_{L} and Z_{R}. Both impedances act as the substitutes for the left and the right terminal units in a real test setup including DUT and load simulator. The circuit schematic including the line voltage waves, line current waves and impedances is illustrated in Figure 5.1. The transmission line of length l is divided

in two sections. The position of the injection probe is given with l_p, which indicates the length of the transmission line on the left side of the injection probe. In order to simplify the equations, the length of the injection probe is assumed to be small enough to be ignored. Hence, the length of the other transmission line is $l - l_\mathrm{p}$. The potential difference across the BCI probe's equivalent circuit is represented by V_T. This representation has the sole purpose of enforcing Kirchhoff's voltage and current laws, and to include the relations that are imposed by the particular interconnections within the circuit.

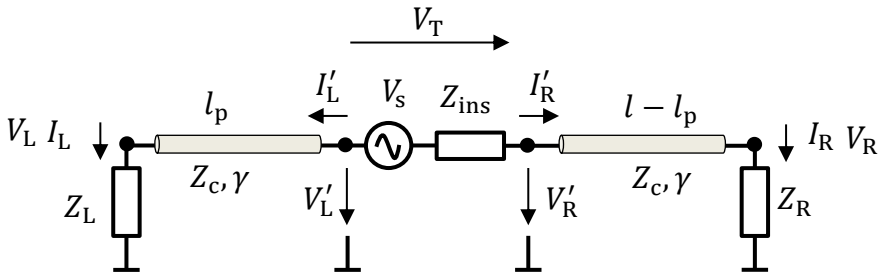

Figure 5.1: Simplified representation of an injection probe located at a point along a wire over a ground plane and the related line voltages and currents

For the left transmission line, the terminal voltage and current at one end are related to the terminal voltage and current at the other end by means of chain parameters (ABCD-parameters) as follows

$$\cosh(\gamma l_\mathrm{p})\, V'_\mathrm{L} - Z_\mathrm{c}\sinh(\gamma l_\mathrm{p})\, I'_\mathrm{L} - Z_\mathrm{L} I_\mathrm{L} = 0, \tag{5.1}$$

$$-\frac{1}{Z_\mathrm{c}}\sinh(\gamma l_\mathrm{p})\, V'_\mathrm{L} + \cosh(\gamma l_\mathrm{p})\, I'_\mathrm{L} - I_\mathrm{L} = 0. \tag{5.2}$$

Similarly, the system of equations describing the relation between voltages and currents at the terminals of the second transmission line is given by

$$\cosh\left(\gamma(l - l_\mathrm{p})\right) V'_\mathrm{R} - Z_\mathrm{c}\sinh\left(\gamma(l - l_\mathrm{p})\right) I'_\mathrm{R} - Z_\mathrm{R} I_\mathrm{R} = 0, \tag{5.3}$$

$$-\frac{1}{Z_\mathrm{c}}\sinh\left(\gamma(l - l_\mathrm{p})\right) V'_\mathrm{R} + \cosh\left(\gamma(l - l_\mathrm{p})\right) I'_\mathrm{R} - I_\mathrm{R} = 0. \tag{5.4}$$

Two other equations are obtained by using the KVL at the source loop and the KCL between the source nodes respectively with

$$V'_\mathrm{L} - V'_\mathrm{R} = V_\mathrm{T}, \tag{5.5}$$

$$I'_\mathrm{L} + I'_\mathrm{R} = 0. \tag{5.6}$$

The equations (5.1)-(5.6) describe a complete BCI coupling. Such description can be used, for example, to calculate the current injected into terminals for a BCI probe if the

feeding and the positioning conditions are known. Furthermore, (5.1)-(5.6) can be formulated in terms of a matrix equation of the form

$$\mathbf{A}\mathbf{x} = \mathbf{b}, \tag{5.7}$$

where the system matrix $\mathbf{A}$ is given by

$$\mathbf{A} = \begin{pmatrix} \cosh(\gamma l_\mathrm{p}) & 0 & -Z_\mathrm{c}\sinh(\gamma l_\mathrm{p}) & 0 & -Z_\mathrm{L} & 0 \\ -\frac{1}{Z_\mathrm{c}}\sinh(\gamma l_\mathrm{p}) & 0 & \cosh(\gamma l_\mathrm{p}) & 0 & -1 & 0 \\ 0 & \cosh(\gamma(l-l_\mathrm{p})) & 0 & -Z_\mathrm{c}\sinh(\gamma(l-l_\mathrm{p})) & 0 & -Z_\mathrm{R} \\ 0 & -\frac{1}{Z_\mathrm{c}}\sinh(\gamma(l-l_\mathrm{p})) & 0 & \cosh(\gamma(l-l_\mathrm{p})) & 0 & -1 \\ 1 & -1 & 0 & 0 & 0 & 0 \\ 0 & 0 & 1 & 1 & 0 & 0 \end{pmatrix} \tag{5.8}$$

and the other vectors are

$$\mathbf{b}^\mathrm{T} = (0 \quad 0 \quad 0 \quad 0 \quad 0 \quad V_\mathrm{T}), \tag{5.9}$$

$$\mathbf{x}^\mathrm{T} = (V_\mathrm{L}' \quad V_\mathrm{R}' \quad I_\mathrm{L}' \quad I_\mathrm{R}' \quad I_\mathrm{L} \quad I_\mathrm{R}). \tag{5.10}$$

If the probe's feeding and the positioning conditions, V_T and l_p, are given, the linear system of equations can be solved for the vector $\mathbf{x}$, for example, by the method of matrix inversion, Gaussian elimination or Cramer's rule. However, the main objective in this chapter can be interpreted as an inverse problem, where I_L and I_R are given and V_T and l_p are to be determined. In line with this concept, two new constraints can be enforced to the system of equations describing the ALSE coupling as follows

$$I_\mathrm{L} - I_{\mathrm{ALSE_L}} = 0, \tag{5.11}$$

$$I_\mathrm{R} - I_{\mathrm{ALSE_R}} = 0, \tag{5.12}$$

where $I_{\mathrm{ALSE_L}}$and $I_{\mathrm{ALSE_R}}$ represent the given ALSE termination currents at the left side and the right side of the transmission line respectively.

In order to solve the system of equations straightforwardly, it should be converted to the general form of (5.7). According to (5.1)-(5.4), the position of the injection probe l_p, appears only as an argument of the hyperbolic functions (5.6). Application of the hyperbolic or trigonometric identities does not prove to be useful for this purpose, as they only reformulate the problem in terms of other hyperbolic functions. Additionally, using the Taylor series expansions of hyperbolic functions leads to polynomials in terms of the function arguments γl_p as

$$\sinh(\gamma l_{\mathrm{p}}) = \gamma l_{\mathrm{p}} + \frac{(\gamma l_{\mathrm{p}})^3}{3!} + \frac{(\gamma l_{\mathrm{p}})^5}{5!} + \cdots \tag{5.13}$$

$$\cosh(\gamma l_{\mathrm{p}}) = 1 + \frac{(\gamma l_{\mathrm{p}})^2}{2!} + \frac{(\gamma l_{\mathrm{p}})^4}{4!} + \cdots. \tag{5.14}$$

This imposes additional constraints to the system of equations. Consequently, using the numerical methods proves to be convenient to seek the best possible values for V_{T} and l_{p} such that all constraints are simultaneously satisfied.

5.1.2 Application of Mathematical Optimization

In this section, an optimization function is developed to approximate the ALSE termination currents using a BCI probe based on given feeding and positioning constraints. Basically, an optimization problem consists of maximizing or minimizing an objective function by systematically selecting values from within an allowed domain and calculating the value of the objective function. In order to find the best possible injection power P_{f} and position l_{p} of the BCI probe at each frequency, the objective function ϵ_{t} is defined. The $\epsilon_{\mathrm{t}}(P_{\mathrm{f}}, l_{\mathrm{p}})$ represents the total error function including the injected power P_{f} and the position of the BCI probe l_{p} as arguments of the function and is given by

$$\epsilon_{\mathrm{t}}(P_{\mathrm{f}}, l_{\mathrm{p}}) = w_{\mathrm{L}} \frac{\left|I_{\mathrm{ALSE_L}} - I_{\mathrm{BCI_L}}(P_{\mathrm{f}}, l_{\mathrm{p}})\right|}{\left|I_{\mathrm{ALSE_L}}\right|} 100 + w_{\mathrm{R}} \frac{\left|I_{\mathrm{ALSE_R}} - I_{\mathrm{BCI_R}}(P_{\mathrm{f}}, l_{\mathrm{p}})\right|}{\left|I_{\mathrm{ALSE_R}}\right|} 100 + \epsilon_{\mathrm{p}}(l_{\mathrm{p}}), \tag{5.15}$$

where $I_{\mathrm{ALSE_L}}$ and $I_{\mathrm{ALSE_R}}$ represent the reference ALSE termination currents at the left and right side, which can be measured or simulated according to Section 2.2.4. The BCI termination currents at certain P_{f} and l_{p} are represented by $I_{\mathrm{BCI_L}}$ and $I_{\mathrm{BCI_R}}$. Both weighting coefficients $\mathrm{w_L}$ and $\mathrm{w_R}$ are defined to emphasize the contribution of the particular error at one side to the total error. The magnitude of the difference between the termination currents is divided by the ALSE termination current and expressed in terms of per 100 to represent the percent error at each side. The function $\epsilon_{\mathrm{p}}(l_{\mathrm{p}})$ represents an additional artificial error function to avoid large position variation along the wire. The reason to define unequal weighting coefficients is to minimize the deviation between the reference current and generated current with the BCI at the DUT side. This may become necessary if the overall performance of the process with equal weighting coefficients does not reach an acceptable accuracy.

The problem of concern is to determine the optimal forward power and position of the BCI probe that minimizes the objective function. The overall process is illustrated in Figure 5.2. As mentioned previously, assigning appropriate domains of definition for both arguments P_{f} and l_{p} is very important to avoid unrealistic or impractical results.

For the forward power, the domain is the set of non-negative real numbers. However, both upper and lower limits can be selected according to the power capability of the used signal generator and power amplifier. The power capability (constraint) in this work is between -145 dBm and 52 dBm. The lower limit is the lowest power provided by the signal generator R&S SMA100A employed in this work. The upper limit is due to the specification of the applied power amplifier PRANA DT150. For the positioning, the domain is the length of the wiring harness. However, it is limited between 3.5 cm and 166.5 cm due to the length of the used BCI probe. The reference point is the middle point of the BCI probe. In other words, the position describes the distance between the load at the DUT side and the middle point of the BCI probe.

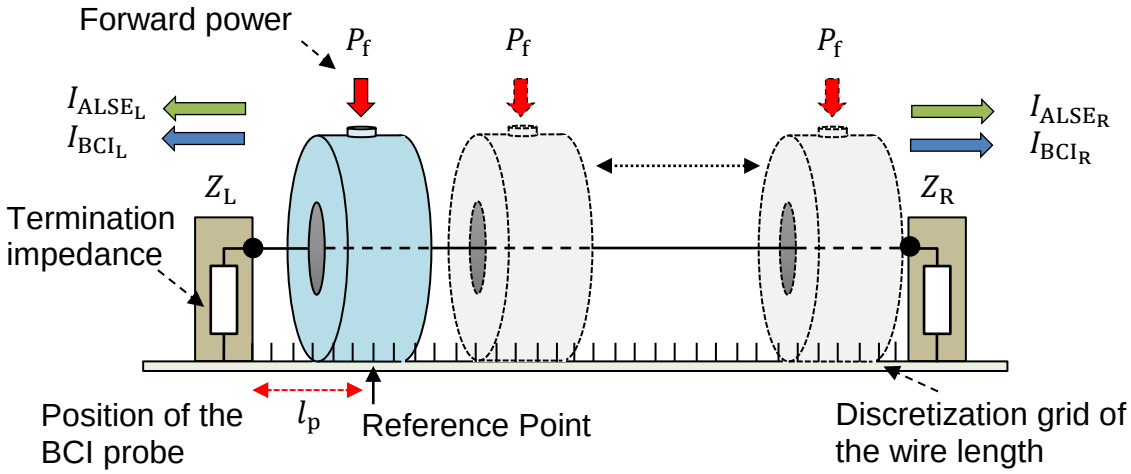

Figure 5.2: Determination of the best possible feeding and positioning conditions to approximate the ALSE termination currents with the BCI termination currents

In order to discretize the domains of definitions for P_f and l_p, both continua are subdivided into a finite number of elements (grid). Generally, the number or size of the grid, through which the domain is discretized, affects the accuracy and convergence of the solution, and therefore need to be chosen with care. If the size of the grid is small, the outcome solution is expected to be more accurate but the cost of computation increases rapidly.

5.1.3 Data Preparation and Method Description

The overview of the applied process to find the best possible forward power and position is illustrated in Figure 5.3. As outlined in Section 5.1.2, the currents flowing into terminal units at each side of the wiring harness during an ALSE test are the reference values during the process. Based on the results presented in Chapter 2, there are two methods to determine the reference values. The first approach is to directly measure the ALSE termination currents with two current probes located next to both harness ends during a real ALSE test. The second approach, as described in Section 2.2.4, is to simulate these reference values by combining the S-parameter models of

the antenna coupling and terminal units to form a cascaded network. The second approach requires the impedance of both terminal units for the desired frequency range. These impedances can be measured separately with a VNA or measured in situ by one of the indirect methods proposed in Chapter 4.

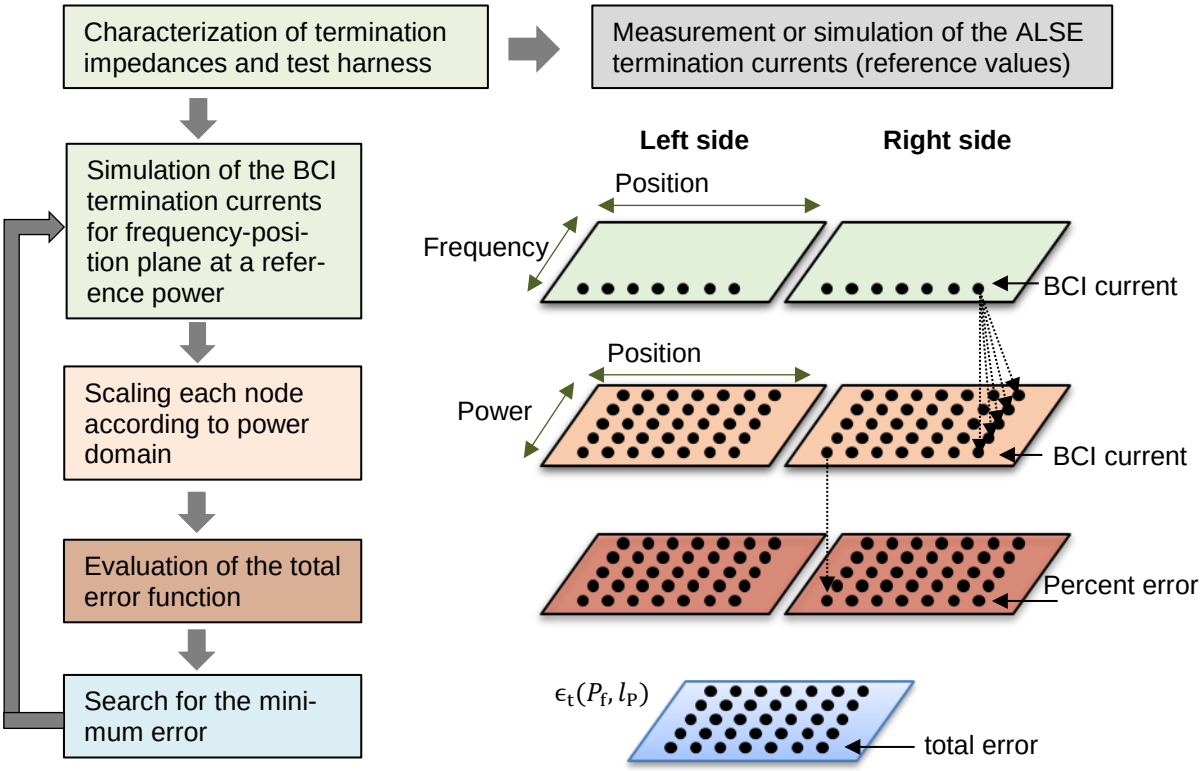

Figure 5.3: Overview of the process to determine the optimal forward power and position to approximate the ALSE termination currents

As described in Section 2.3.1, calculation of the currents flowing into the terminal units at a certain position and forward power requires a coupling model for the BCI probe, the per-unit-length parameters of the transmission line and the impedance of the terminal units. The modelling of the BCI probe and the characterization of the transmission line to simulate the BCI immunity test structure are carried out according to Section 2.2.2 and 2.2.3. Based on the cascaded network, the BCI termination currents are calculated for a reference forward power and the entire domain of the probe's position. The calculated BCI termination current at a certain frequency consists of a vector for each side separately. The reference power selected at this step is 0 dBm. The frequency-position planes in Figure 5.3 are demonstrated as vectors to separate the results for each frequency. Each node indicates the calculated BCI termination current for a certain position and the reference power at the frequency of interest.

The next step is the uniform scaling of each current vector by the scale factors defined by the forward power domain. Such scaling is initially a linear transformation obtained by the scalar multiplication of each BCI current vector with every element of the forward power domain. The results are two $n_p \times n_l$ matrices representing the entire

possible combinations, where n_{p} and n_{l} represent the number of elements in the forward power domain and the probe's position domain respectively. The power-position planes demonstrated in Figure 5.3 represent both matrices, where each element indicates the calculated BCI termination current. In order to determine the difference between the reference ALSE termination current at each side and the corresponding BCI termination current, the error is calculated. The results are again two $n_{\mathrm{p}} \times n_{\mathrm{l}}$ matrices represented in form of the error plane at each side.

The final step is to evaluate the function $\epsilon_{\mathrm{t}}(P_{\mathrm{f}}, l_{\mathrm{p}})$ based on (5.15). Finding the smallest entry (node) in the total error matrix is straightforward. The forward power and BCI probe position that minimize the function are the optimal feeding and positioning conditions according to the selected grid. The process is repeated for each frequency to cover the entire frequency range. As given in (5.15), the artificial error function to avoid significant position variation along the wire is considered with $\epsilon_{\mathrm{p}}(l_{\mathrm{p}})$. The primary position of the BCI probe is the midpoint of the wire. This is taken into account during the initialization at the first frequency. The error related to the position changes is calculated by

$$\epsilon_{\mathrm{p}}(l_{\mathrm{p}}) = k_{\mathrm{er}} \times \frac{|\text{Position grid} - \text{Last position}|}{\text{Setup length}}, \tag{5.16}$$

where k_{er} indicates the weighting coefficient to control the impact of position variations (position jumps) of the BCI probe.

5.2 Experimental Results

In order to validate the optimization method proposed in this section, an immunity test setup is prepared. The setup consists of a wire of length $l = 1.7\ \mathrm{m}$, spanned between two metal test fixtures at 5 cm above the ground plane. A small PCB consists of a temperature sensor LM 35 serves as the DUT during the entire test. The temperature sensor has three pins including power supply, ground and analog output [60]. The prepared PCB is equipped with a 1 µF capacitor between the power supply pin and the ground. Additionally, a RC parallel circuit is soldered between the analog output and the ground based on the proposed configuration for the high capacitive structures in [60]. The first step in this section is to perform the ALSE test for two different test configurations by subjecting the analog output pin and the power supply pin to an electromagnetic disturbance. Both test configurations are shown in Figure 5.4. Following this, the impedance of both terminal units at each test configuration is indirectly measured by means of a BCI probe. Finally, the measured ALSE termination currents are reproduced by means of the optimization process described in Section 5.1.2.

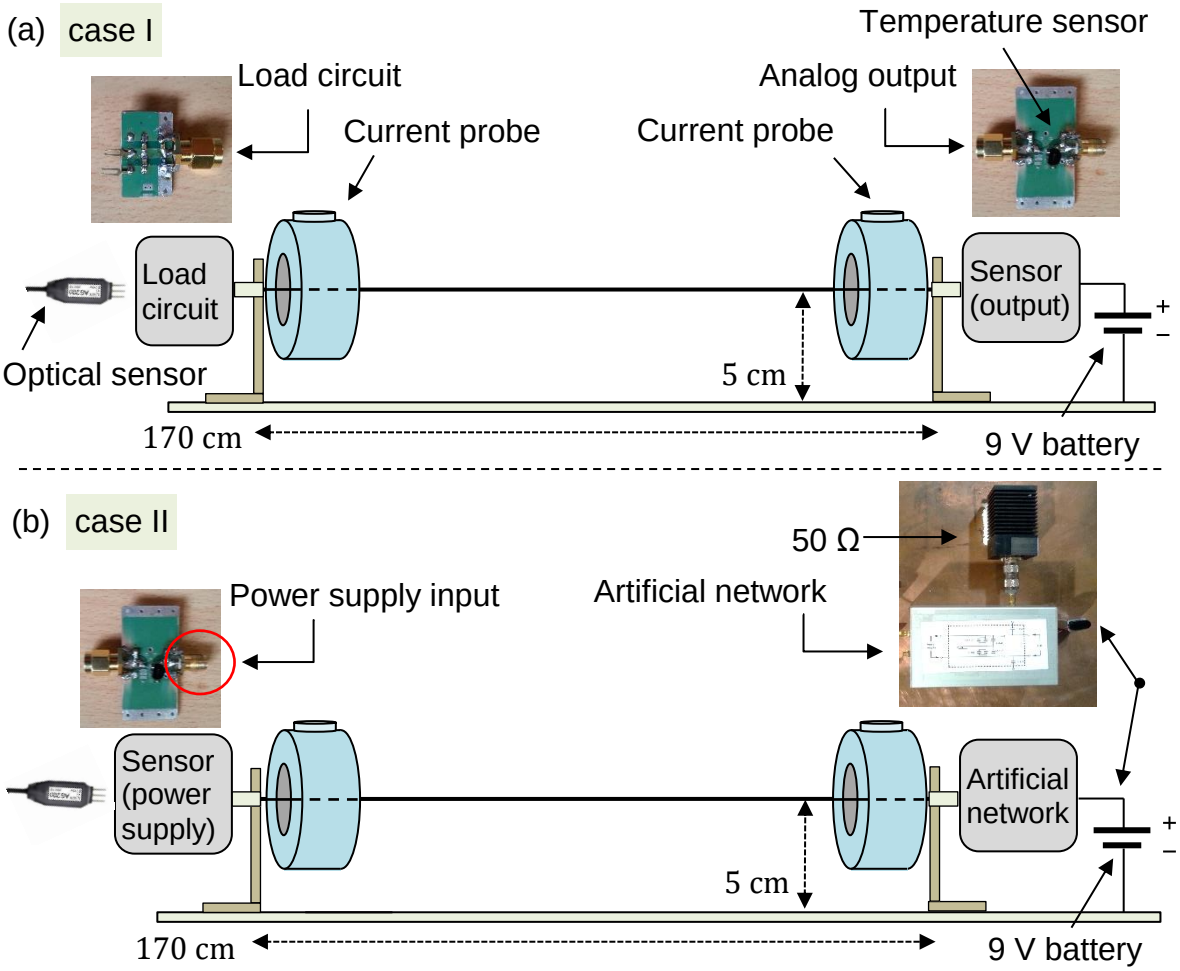

Figure 5.4: Structure of the ALSE test setups, case I represents the sensor-load configuration (a), and case 2 represents the sensor-AN configuration (b)

5.2.1 Description of Test Configurations

In order to perform the ALSE test, two different test configurations are selected. The first case (case I) consists of the DUT at the right side and a load circuit at the left side of the wire. As illustrated in Figure 5.4(a), the wire representing the wiring harness is directly connected to the analog output pin of the temperature sensor and the load circuit. This means that the analog output is subjected directly to the electromagnetic disturbance. The load circuit is a PCB which consists of a 30 nF capacitor and a 100 Ω resistor in parallel. The DC voltage is measured with an optical sensor (Langer A200) between the wire and the ground at the left side. The sensor's power supply pin is connected to a 9 V battery.

As illustrated in Figure 5.4(b), the second case (case II) consists of the DUT at the left side and an artificial network on the right side. A 9 V battery is connected to the artificial network and serves as the power supply of the temperature sensor.

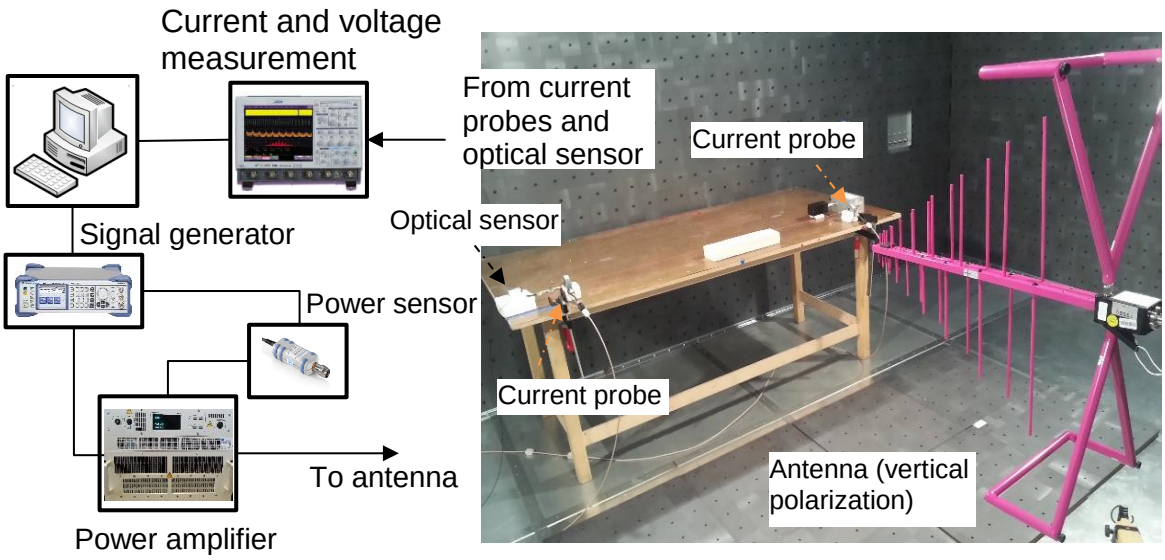

Figure 5.5: Structure of the ALSE test setup and the test equipment outside located the chapter

In this case, the power supply pin of the temperature sensor is subjected directly to the electromagnetic disturbance. The optical sensor (Langer A200) measures the DC voltage between the analog output of the sensor and the ground at the DUT side. The structure of the test setup and the measurement instruments are illustrated in Figure 5.5. The ALSE test is performed at the calibrated field of 100 V/m for vertical polarization between 80 MHz and 1 GHz. The highest forward power is restricted to 52 dBm due to the capability of the power amplifier. The frequency step is 1 MHz between 80 MHz and 100 MHz. The frequency step is 10 MHz for the rest of the frequencies. The ALSE method is performed for the analog output and the power supply separately.

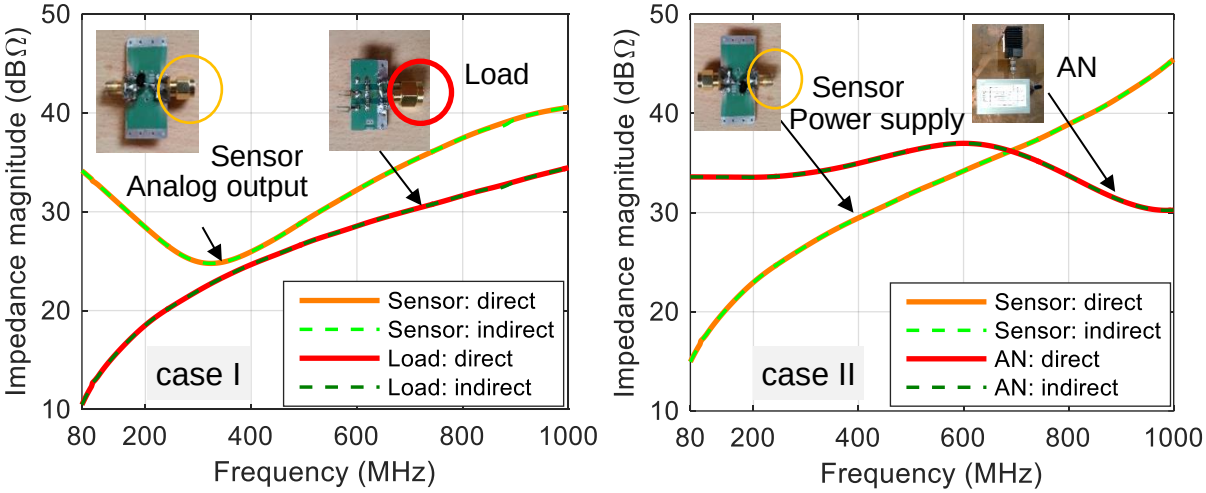

Figure 5.6: Measuring the impedance at the wire ends. Case I includes the sensor's analog output and the load PCB. Case II includes the sensor's power supply and the artificial network.

As described in Section 5.1.2, in order to reproduce the ALSE termination currents, the impedance of each termination impedance is required. As discussed earlier

in Chapter 4, the extended single method measures the termination impedance with the highest accuracy in the frequency range of interest. Consequently, the impedance measurement is performed at both setups with the extended single probe method. The comparison between magnitude of the directly measured and the indirectly measured termination impedances with the BCI probe between 80 MHz and 1 GHz are shown in Figure 5.6. As expected, there is a very good agreement between the directly and indirectly measured impedances. From the results can be concluded that almost no error will be added to the total error function as result of inaccurate impedance measurement

5.2.2 Measurement Results and Reproducing Currents

The reference termination currents measured during the ALSE tests (red, orange) and the simulated BCI termination currents at the reference power and sample positions (dark blue, light blue) are shown in Figure 5.7. In order to make the plot elements more identifiable, the BCI termination currents don't comprise the results for the entire positioning grid. The black arrow indicates the direction of the optimization process. The objective of the optimization process is to minimize the deviation of the BCI currents from their reference ALSE currents at each frequency. In other words, the process tries to match the termination currents at the left side (red, dark blue) and the termination currents at the right side (orange, light blue) simultaneously.

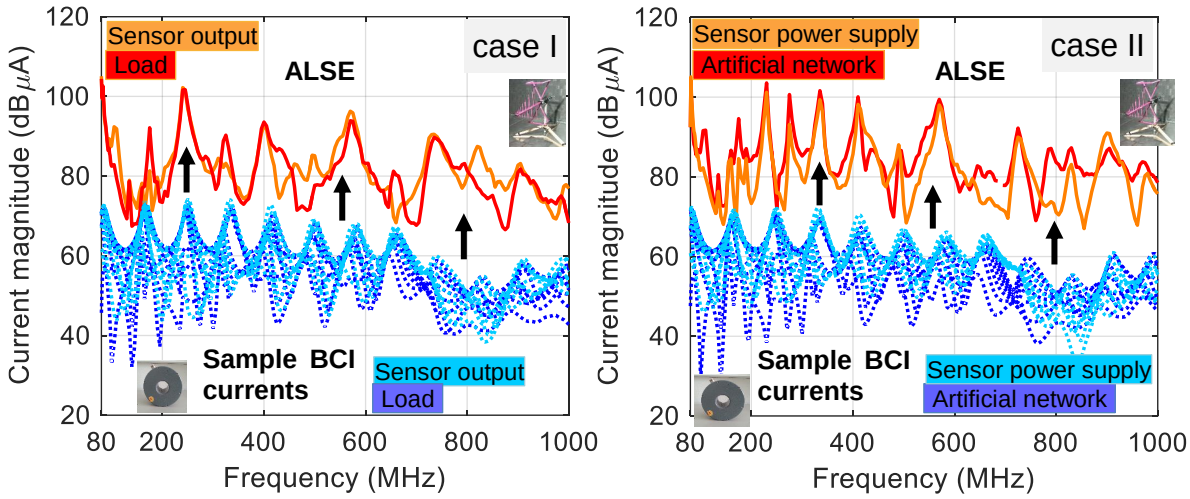

Figure 5.7: Minimizing the deviation between the ALSE currents and the BCI currents at both test configurations. The BCI currents are shown only for sample positions of BCI

The exact simulation of the BCI currents is only possible, as the termination impedances are characterized in advance. Furthermore, the power amplifier is assumed to operate linearly with a constant gain of 150 W during the process. In order to reproduce the ALSE currents with a BCI probe, the optimal feeding and positioning conditions are calculated according to Section 5.1.3. The comparison between the ALSE termination currents measured directly during the test and the reproduced termination currents with the BCI probe are shown in Figure 5.8. The deviation between the results

are depicted in light and dark green. Similar to Figure 5.7, red and orange colors indicate the reference ALSE currents and the blue color indicate the reproduced BCI current. As an overall trend, it is clear that the process achieves better results for the sensor-load configuration (case I) than the sensor-AN configuration (case II). The higher deviations are distributed without particular regard to the frequency axis. For example, while in case I the maximum deviation occurs at 480 MHz, in case II the maximum deviation occurs at 180 MHz. Due to the equivalent weighting coefficients, no priority was given to the efficiency at one side during the process. However, the overall tendency shows that the smaller current magnitude at each frequency is better reproduced.

The optimal value of the individual objective function $\epsilon_{\mathrm{t}}(P_{\mathrm{f}}, l_{\mathrm{p}})$ for the entire frequency are shown in Figure 5.9. The overall trend for the objective function is significantly affected by the percent errors of the current at each side. The objective functions reach their highest points, where the variation of BCI probe position or the injected forward power cannot reproduce the current at both sides simultaneously. From the results can be concluded that the artificial positioning error has almost no influence on the objective functions. This means that even high jumps along the harness cannot reduce the minimum error achieved in both cases.

The measured immunity levels during the ALSE test (orange, light blue) and the calculated BCI forward power (red, dark blue) for both test configurations are demonstrated in Figure 5.10. As can be seen from the graph, the calculated BCI forward power (feeding condition, P_{f}) is less than the severity level during the ALSE test at the entire frequency range. This overall trend corresponds to the conclusions in Chapter 2, where it was shown that generally less power is required to achieve a certain interfering levels during the BCI test.

The calculated probe's position (positioning condition) illustrated Figure 5.11 for case I and case II are respectively depicted in red and dark blue. The comparison between both plots does not indicate a particular trend for the positioning conditions. The discretization grid and power grid were selected as 1 cm and 0.1 dBm respectively. The proposed process searches straightforwardly at each frequency for the global optimum in the specified, discrete domain of positions and injected powers. One way to obtain a smoother function is to reduce the size of the position and power grids. Due to the structure of (5.5), there may exist several local minima with increasing frequency (see Figure 5.12). Another way to obtain a smoother function is to restrict the search within a particular neighborhood of the last position. However, as local optima deliver sub-optimal solutions to the global problem in many cases, the algorithm needs to continue the search beyond the neighborhood of the last position.

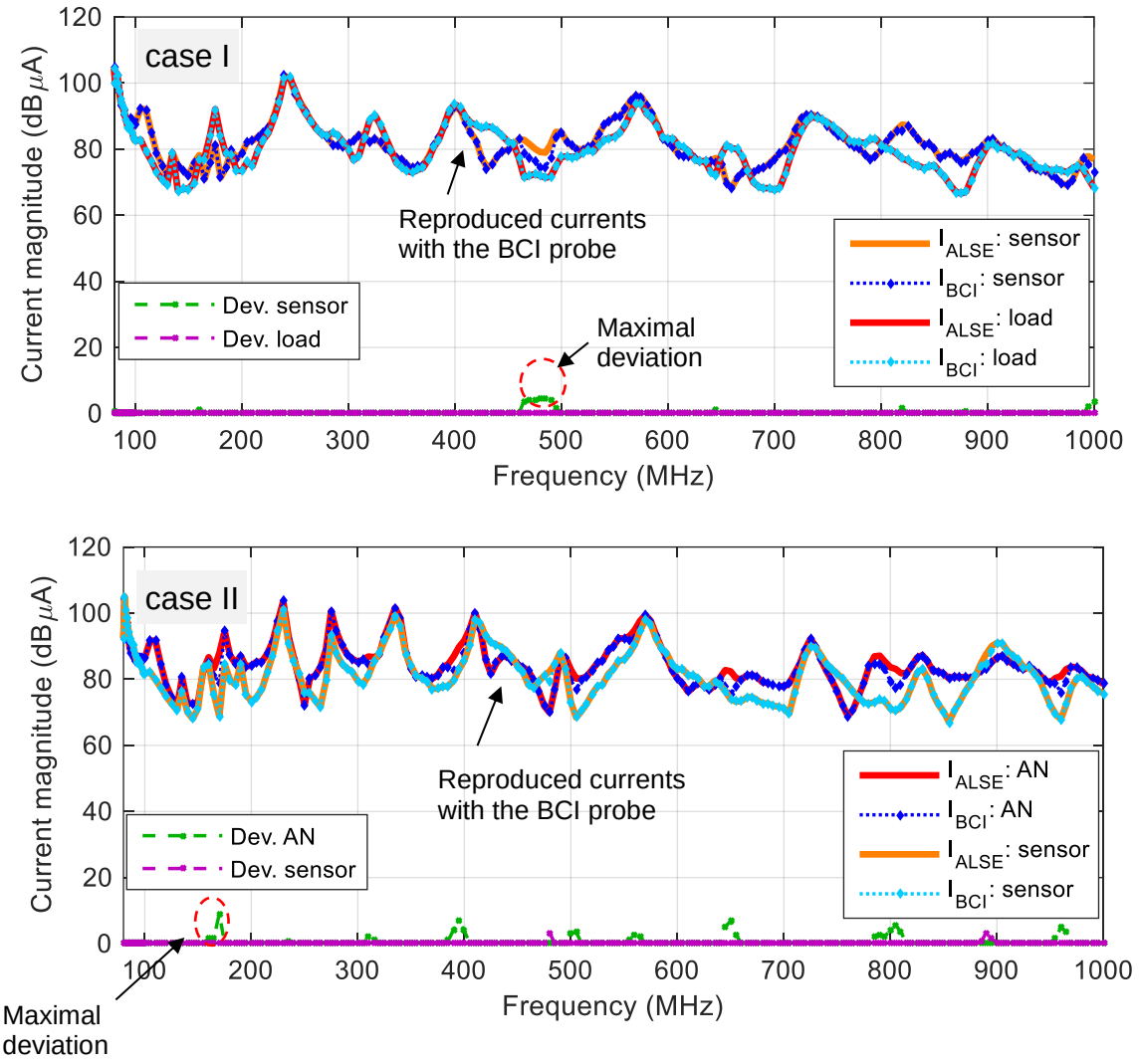

Figure 5.8: Comparison between the measured ALSE currents at both terminations for the case I and case II and the measured currents for the immunity level.

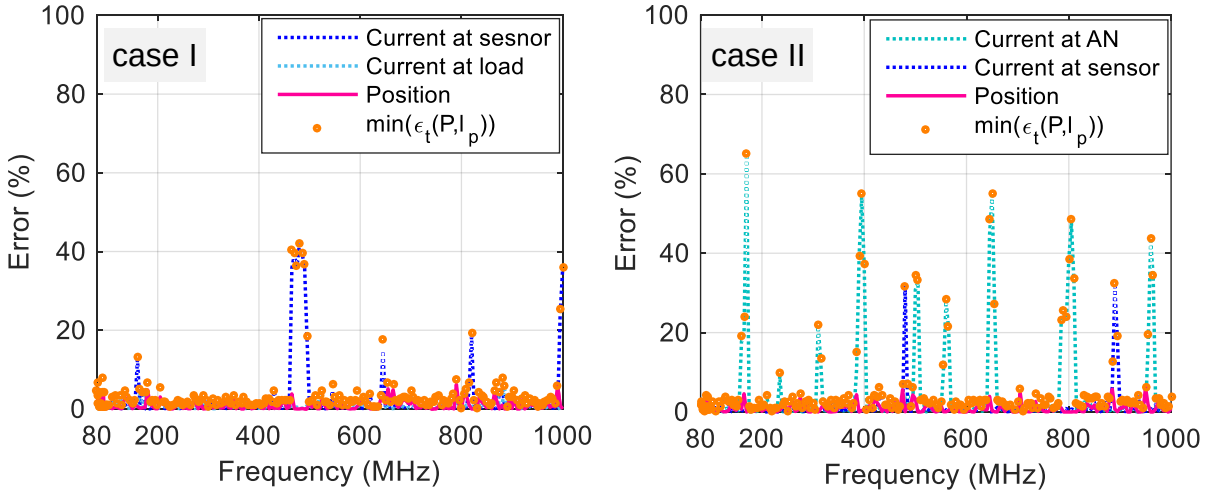

Figure 5.9: Comparison between the value of the objective function for the best possible feeding and positioning conditions. The individual errors regarding the current at each side and the artificial errors to reduce position variations are presented with blue and pink colors respectively.

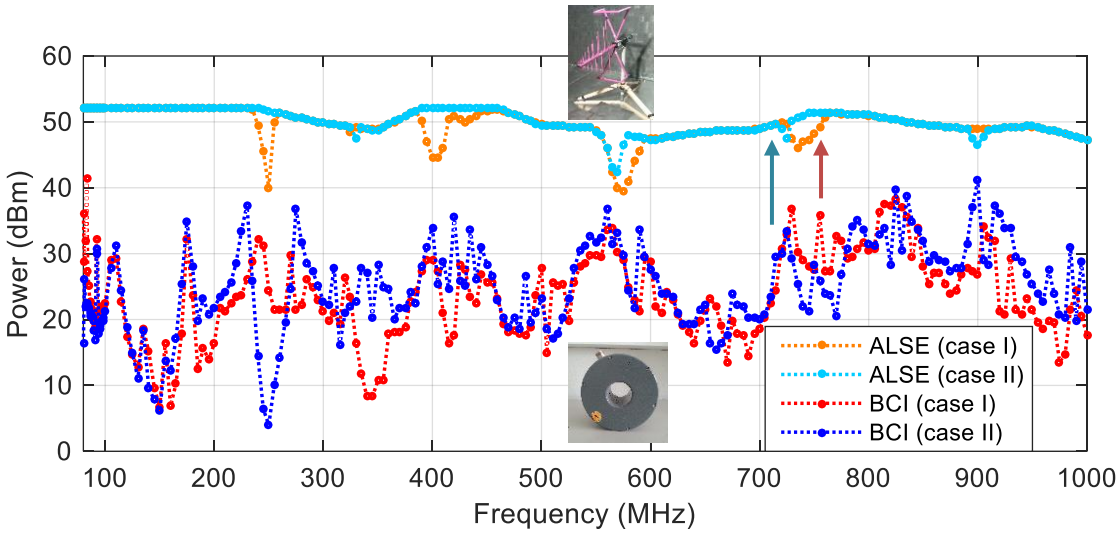

Figure 5.10: Comparison between the immunity level obtained during the ALSE tests at 100 V/m (vertical polarization) and the BCI power levels to reproduce the same current

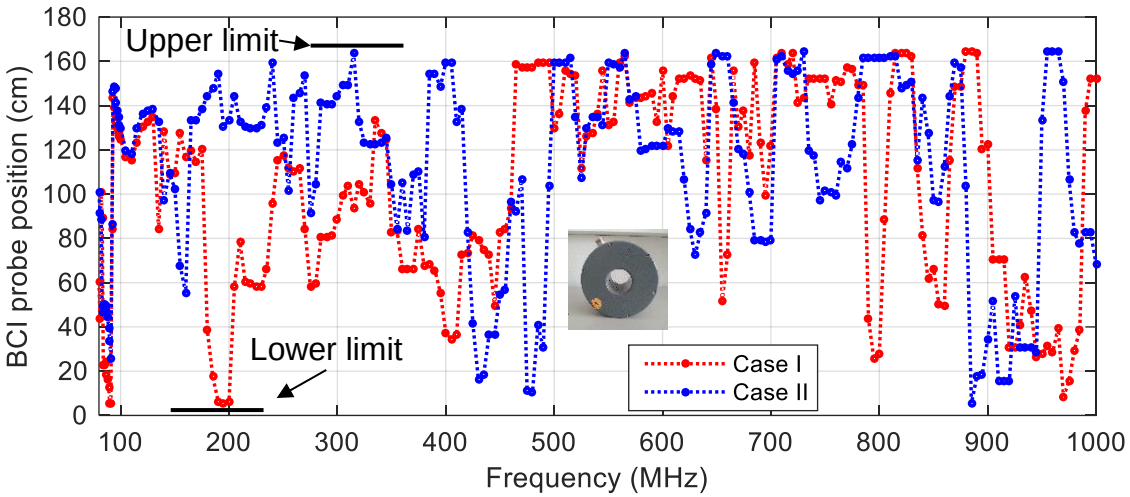

Figure 5.11: Comparison between the calculated positioning conditions according to the grid defined for the probe's position

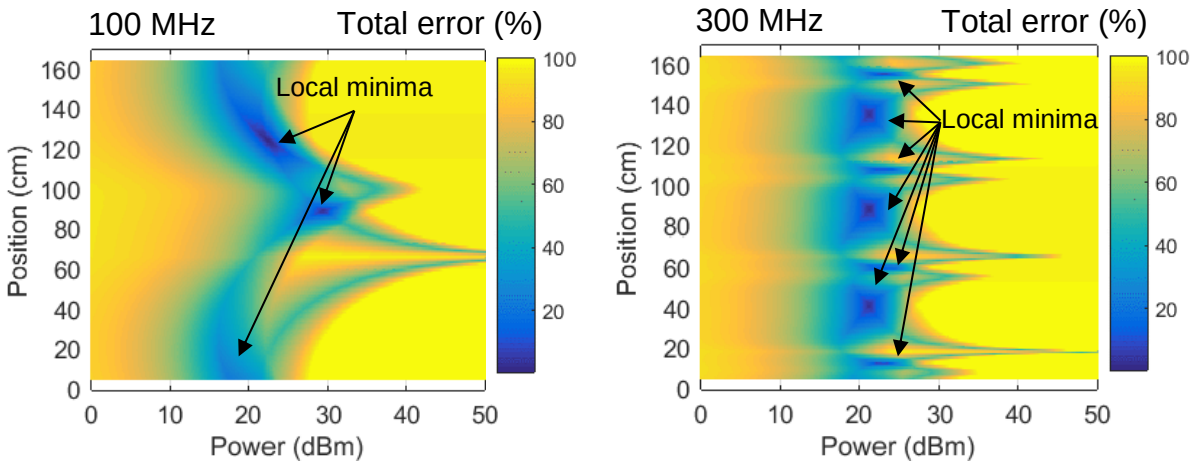

Figure 5.12: Total error function calculated at 100 MHz and 300 MHz and the formation of several local minima with increasing frequency

5.3 Limitations of Reproducing ALSE Currents with BCI

The experimental results presented in the previous section confirmed that reproducing the ALSE currents achieves a good match for the selected test scenarios. However, the scope of these scenarios does not allow generalizing. The limitations of the proposed optimization process and the complexities of practical applications make it hardly possible to use the entire process in a straightforward manner.

First, the limitations related to the characterization of the ALSE and BCI couplings and termination impedances are considered. Concerning the ALSE coupling, the first issue is the determination of the reference ALSE termination currents. In the previous section, the measured ALSE termination currents were directly used as the references in the optimization process. However, in line with the idea of substituting ALSE with BCI, it is important to calculate the ALSE termination currents without performing the real test by means of a simulation environment. With respect to the results in Section 2.3.2, the measurement-based ALSE model can be used to calculate the reference currents if the termination impedances are known. The second issue concerning the ALSE coupling is the exact characterization of the impedance of the terminal units under operation condition. As discussed in Chapter 4, using CTs to determine the impedance is affected by errors of different origin, especially when it comes to using the single probe method, double probe method and current distribution method. Application of the proposed methods in Chapter 4, beyond the specified frequency range increases the errors related to the calculated ALSE and BCI termination currents in a simulation environment. These errors must be considered in calculating the termination currents. Although the extended single probe method is the most promising method in terms of accuracy and bandwidth, it requires an exact characterization of the setup in absence of the terminal units.

In a similar way as that of the ALSE coupling, an accurate model of the BCI coupling is required. The described measurement-based BCI coupling is a powerful tool, which can be used to simulate the BCI termination currents for different feeding and positioning conditions. However, as discussed in Chapter 2, the measurement-based modelling of BCI is also prone to some errors and therefore, adequate precautions should be taken to avoid these. Moreover, similar to the ALSE model, calculation of the BCI termination currents requires the impedance of terminal units. Any error in measurement of the impedances will lead to incorrect feeding and positioning conditions.

The test scenarios selected in this chapter included a single wire over a ground plane and terminal units with a linear behavior. This can be considered as a significant simplification, since typical test scenarios consist of a bundle of wires and nonlinear terminal units. With respect to the test setups in the real applications, two issues should be taken into account: first, the expansion of coupling models to the setups with wire

bundles. And second, the expansion of the impedance measurement to nonlinear terminal units. As described in Chapter 2, characterization of the ALSE and BCI coupling to wire bundles can be considered as linear processes, which can be carried out based on the measurement-based modelling approach by increasing the number of ports. However, the expansion of the indirect measurement methods to characterize the nonlinear behavior of terminal units increases extremely the complexity of the modelling and should be the subject of further research.

Second, the limitations related to the calculation of the optimal feeding and positioning conditions are considered. The focus in this thesis was on solving the problem based on numerical methods, however, finding an analytical solution to the system of equations given in Section 5.1.1 based on the harness characteristics and the termination impedances should be the subject of investigation in future works. The experimental results considered only the magnitude of the termination currents. Nevertheless, the effect of difference in the phase of termination currents should be analyzed. The proposed optimization process for the specific case of a single wire above a ground plane carried out straightforwardly according to the objective function given in (5.15). However, in case of wire bundles, the complexity increases rapidly, if the goal is to achieve the same current at all wires. For example, in case of three wires over a ground plane, the optimization process has to minimize the deviation of six different currents, i.e. three currents at each side. From the results presented in this chapter can be concluded that it is not possible to meet a certain accuracy or deviation even for a single wire over a ground plane with the chosen degrees of freedom. Hence, application of the entire process in case of wire bundles does not appear to be expedient and requires principal modifications in the objectives of the optimization process or the degrees of freedom. The following solutions can be considered to achieve better results:

- The first solution is the specification of an appropriate trade-off to reduce the complexity of the objective function. For example, the objective function can be modified in a way that the ALSE termination currents are reproduced at a certain port instead of the entire ports. In other words, the entire process including impedance measurement and optimization, is carried out for a certain wire among the wire bundle.
- The second solution is the expansion of the degrees of freedom. Such expansion can be realized, for example, by using several injection probes instead of only one. This idea can be implemented by clamping the injection probes around the wire bundle at different positions as described in [39] and [41] or by clamping one or two injection probes around each wire separately. Both of these concepts, especially the second one, significantly expand the degree of freedom and allow achieving better performance.

As mentioned earlier, the problem could be simplified if only the CM termination currents are considered. The limitation of this simplification resides in the fact that in case of wire bundles, imposing equivalence between ALSE and BCI in terms of CM currents does not assure the equivalence of currents in each wire of the wire bundle. Altogether, individual parts of the proposed process such as the modeling and impedance measurement methods possess the potential of being investigated separately.

Summary and Outlook

The most commonly used automotive immunity test methods are described in ISO 11452 series. Absorber Line Shielded Enclosure (ALSE) and Bulk Current Injection (BCI) apply different coupling mechanisms to assess the immunity of a device under test. The recommended test setup for each method comprises a wiring harness connected between two terminal units including a device under test and a load simulator. Despite using similar test setups, different interference currents are injected into the terminal units at each test method and therefore, the correlation between the test results is often poor.

The idea in this thesis is to improve the correlation by reproducing the interference currents at the terminal units during an ALSE test with a BCI probe. Any attempt to achieve the same interference currents requires not only accurate coupling models for ALSE and BCI but also the input impedance of terminal units under normal operation condition. In order to remain operational, the device under test must be connected to the load simulator. This implies applying non-invasive methods to measure the input impedance of terminal units without disconnecting the wiring harness.

In this context, a precise and fast measurement-based modelling was proposed in this thesis to calculate the interference currents at the terminal units with known input impedances during ALSE or BCI tests. In line with the idea of developing non-invasive methods to measure the input impedance of terminal units, the behavior of different current transformers in terms of output impedance, transfer impedance and insertion were analyzed. Different indications on the practicability, strengths and weaknesses of using different current transformers for the impedance measurement were given and discussed. In order to measure the required input impedance values with current transformers, four methods were proposed including the single probe method (SPM), the double probe method (DPM), the current distribution method (CDM) and the extended single probe method (ESPM). The proposed methods were compared and limitations of each method were discussed. Finally, an optimization process was introduced to control the injected currents into terminal units based on the input impedance of terminal units and the coupling models of ALSE and BCI. The process controls the feeding and positioning conditions of a BCI probe to achieve the minimum deviation between the ALSE and BCI termination currents based on the specified degrees of freedom.

The combination of non-invasive methods with current transformers to measure the input impedance of terminal units and reproducing the ALSE interference currents with a BCI probe was proposed for the first time in this thesis. The success in achieving good results at majority of frequencies in the sample test scenarios confirmed the applicability of the proposed process.

All investigations were focused on the specific case of a single wire over ground structure representing the wiring harness. The reason was to reduce the complexity and assess the applicability of each method by breaking down the original problem to simpler sub-problems. Therefore, the expansion of the proposed methods for the case of wiring harness should be investigated in future works. Concerning the impedance measurement with CTs, the accuracy and bandwidth of the proposed methods should be expanded by improving the de-embedding methods or increasing the number of primary measurements. The concept of impedance measurement could be further improved by a combination of capacitive and inductive coupling. In respect of reproducing the same interference levels, further investigations have to be carried out on development of multiple coupling techniques using several CT's to increase the degrees of freedom. Moreover, more focus should be put on deriving a closed-form analytical solution for the proper feeding and positioning conditions as it offers a clear view into how variables and interactions between them affect the final result. Since all of the work presented here is based on linear loads, one important area for extension of this work is nonlinear loads, which should be the subject of further research.

Although many of the above-mentioned issues are currently subjects of research, this research is scattered or deals with small areas, and is generally not enough to achieve the required comprehensive overview of the entire process. Therefore, continuous improvement of these limitations requires expanded and coordinated research groups, which contribute more interest and research efforts to overcome the complexities and limitations. Altogether, the theoretical and experimental work presented in this thesis was intended to draw attention to the potential of BCI to substitute ALSE using the measurement-based modelling and the indirect measurement of impedance with CTs.

Reference

[1] ISO 11452-2: “Road vehicles – Component test methods for electrical disturbances from narrowband radiated electromagnetic energy - Part 2: Absorber-lined shielded enclosure (ALSE)”, 2004.

[2] ISO 11452-4: “Road vehicles – Component test methods for electrical disturbances from narrowband radiated electromagnetic energy - Part 4: Bulk Current Injection (BCI),” 2004.

[3] D. A. Hill: “Current Induced on Multiconductor Transmission Lines by Radiation and Injection,” IEEE Transactions on Electromagnetic Compatibility, Vol. 34, No. 4, Nov. 1992.

[4] J. W. Adams, J. Cruz and D. Melquist: “Comparison Measurements of Currents Induced by Radiation and Injection,” IEEE Transactions on Electromagnetic Compatibility, Vol. 34, No. 3, Aug. 1992.

[5] J. M. Harris: “A Comparison of Bulk Cable Current Injection and Radiated Field Susceptibility Test Methods,” IEEE International Symposium on Electromagnetic Compatibility, USA, Aug. 1993.

[6] J. Perini, L. S. Cohen: “On the Equivalence of Radiated and Injected Tests,” IEEE International Symposium on Electromagnetic Compatibility, USA, Aug 1995.

[7] S. Pignari and F. G. Canavero, “Theoretical Assessment of Bulk Current Injection Versus Radiation,” IEEE Transactions on Electromagnetic Compatibility, Vol. 38, Aug. 1996.

[8] D. H. Trout: “Investigation of the Bulk Current Injection Technique by Comparison to Induced Currents from Radiated Electromagnetic Fields,” IEEE International Symposium on Electromagnetic Compatibility, USA, Aug. 1996.

[9] S. Pagnari and F. G. Canavero: “On The Equivalence Between Radiation and Injection in BCI Testing,” IEEE International Symposium on Electromagnetic Compatibility Proceedings, China, May 1997.

[10] G. Spadacini and S. A. Pignari: “A Bulk Current Injection Test Conforming to Statistical Properties of Radiation-Induced Effects,” IEEE Transactions on Electromagnetic Compatibility, Vol. 46, No. 3, Aug. 2004.

[11] M. Coenen, H. Pues and T. Bousquet: “Automotive RF immunity test set-up analysis: Why test results can't compare,” EMC Compo, Croatia, 2011.

[12] C Taylor, R. Satterwhite and C. Harrison: “The Response of a Terminated Two-Wire Transmission Line Excited by a Nonuniform Electromagnetic Field”, IEEE Transactions on Antennas and Propagation, Vol. 13, No. 6. Nov. 1965.

[13] C. R. Paul: “Frequency response of multiconductor transmission lines illuminated by an electromagnetic field,” IEEE Transactions on Electromagnetic Compatibility, No. 4, 1976.

[14] A. Agrawal, H. Price and S. Gurbaxami: “Transient response of Multiconductor Transmission Lines Excited by a Nonuniform Electromagnetic Field,” IEEE Transactions on Electromagnetic Compatibility, Vol. 22, Canada, Jun. 1980.

[15] F. Rachidi, “Formulation of the Field-To-Transmission Line Coupling Equations in Terms of Magnetic Excitation Field,” IEEE Transactions on Electromagnetic Compatibility, Vol. 35, No. 3, Aug 1993.

[16] M. Omid, Y. Kami, and M. Hayakawa: “Field Coupling to Nonuniform and Uniform Transmission Lines”, IEEE Transactions on Electromagnetic Compatibility, Vol. 39, No. 2, Aug 1997.

[17] L. Paletta, J.P. Paramantier, F. Issac, P Dumasand and J.C. Alliot: “Susceptibility Analysis of Wiring in a Complex System Combining a 3-D Solver and a Transmission-Line Network Simulation,” IEEE Transactions on Electromagnetic Compatibility, Vol. 44, No. 2, May 2002.

[18] G. Spadacini, S. A. Pignari and F. Marliani: “Incident-Field Measurement in Proximity of Wiring Harness for Radiated Susceptibility Assessment,” IEEE International Symposium on Electromagnetic Compatibility, Aug. 2005.

[19] S. Buntz, H. Leier, S. Fuchs, D. Gwisdalla and W. Menzel: “Modeling of Radiated Immunity Measurements by an Active Two-Port Model,” International Zurich Symposium on Electromagnetic Compatibility, Germany, Sep. 2007.

[20] J. R. K. Kuvedu-Libla: “Radiated Immunity Tests of Automotive EMC Challenge Vehicle Active Antenna Designs,” IEEE International Symposium on Electromagnetic Compatibility, USA, Aug. 2008.

[21] V. Rodriguez: “Automotive Component EMC Testing: CISPR 25, ISO 11452-2 and Equivalent Standards,” IEEE Electromagnetic Compatibility Magazine, Vol. 1, No. 1, July 2012.

[22] G. Spadacini, F. Grassi, F. Marliani and S. A. Pignari: “Transmission-Line Model for Field-to-Wire Coupling in Bundles of Twisted-Wire Pairs Above Ground,” IEEE Transactions on Electromagnetic Compatibility, Vol. 56, No. 6, Dec. 2014.

[23] M. Leone, H. L. Singer: “On the Coupling of an External Electromagnetic Field to a Printed Circuit Board Trace” IEEE Transactions on Electromagnetic Compatibility, Vol. 41, No. 4, Dec. 2014

[24] M. F. Sultan: “Modeling of a bulk current injection setup for susceptibility threshold measurements,” IEEE International Symposium on Electromagnetic Compatibility, USA, 1986.

[25] A. Orlandi: “Circuit Model for Bulk Current Injection Test on Shielded Coaxial Cables,” IEEE Transactions On Electromagnetic Compatibility, Vol. 45, No. 4, Nov. 2003.

[26] F. Lafon, Y. Benlakhouy and F. De-Daran: “Injection Probe Modeling for Bulk Current Injection Test on Multi Conductor Transmission Lines,” IEEE Transactions on Electromagnetic Compatibility, Vol. 46, No. 3, Aug. 2004.

[27] A. Orlandi, G, Antonini, and R. M. Rizzi: “Equivalent Circuit Model of a Bundle of Cables for Bulk Current Injection (BCI) Test,” IEEE Transactions on Electromagnetic Compatibility, Vol. 48, No. 4, Nov. 2006.

[28] G. Antonini, A. C. Scogna, and A. Orlandi: “Grounding, Unbalancing and Length Effects on Termination Voltages of a Twinax Cable During Bulk Current Injection,” IEEE Transactions on Electromagnetic Compatibility, Vol. 46, No. 2, May 2004.

[29] F. Grassi, F. Marliani, and Sergio A. Pignari: “Circuit Modeling of Injection Probes for Bulk Current Injection,” IEEE Transactions On Electromagnetic Compatibility, Vol. 49, No. 3, Aug. 2007.

[30] L. Weber; S. Dickmann: “SPICE Simulation Method for BCI Component Tests” International Zurich Symposium on Electromagnetic Compatibility, Germany, Sep. 2007.

[31] J. McLean, R. Sutton: “The Time Domain Response of BCI Transformers,” IEEE International Symposium on Electromagnetic Compatibility, USA, Aug. 2009.

[32] S. Kwak, J. Jo, S. Noh, H. Lee, W. Nah and S. Kim: “Bulk Current Injection Test Modeling Using an Equivalent Circuit for 1.8V Mobile ICs,” Asia-Pacific Symposium on Electromagnetic Compatibility, Australia, 2012.

[33] N. J. Carter: “Low Cost Susceptibility Testing,” IEEE Colloquium on Low Cost EMC Testing, England, Sep. 1993.

[34] F. Lafon, F. De-Daran and L. Caves: “Harness Influence in Bulk Current Injection Testing.”, International Zurich Symposium and Technical Exhibition on Electromagnetic Compatibility, Switzerland, 2005.

[35] F. Grassi and S. A. Pignari: “Characterization of the Bulk Current Injection Calibration-Jig for Probe-Model Extraction,” IEEE International Symposium on Electromagnetic Compatibility Proceedings, Italy, Jul. 2010.

[36] P. S. Crovetti and F. Fiori: “A Critical Assessment of the Closed-Loop Bulk Current Injection Immunity Test Performed in Compliance with ISO 11452-4,” IEEE Transactions on Instrumentation and Measurement, Vol. 60, No. 4, Apr. 2011.

[37] F. Grassi, C. Rostamzadeh, D. Bellan, G. Spadacini and S. A. Pignari: “Assessment of the Bulk Current Injection Test Procedure Based on the Substitution Method,” Asia-Pacific Symposium on Electromagnetic Compatibility, Australia, 2013.

[38] F. Grassi, C. Rostamzadeh, P. Kolbe, G. Spadacini and S. A. Pignari: “Assessing Linearity of Injection Probes Used in BCI Test Setups for Automotive Applications,” IEEE International Symposium on Electromagnetic Compatibility, USA, Aug. 2013.

[39] M. Cuvelier, J. Rioult, M. Klingler and S. Ficheux: “Double Bulk Current Injection: A New Harness Setup to Correlate Immunity Test Methods,” IEEE International Symposium on Electromagnetic Compatibility, Turkey, May 2003.

[40] F. Marliani, G. Spadacini and S. A. Pignari: “Double Bulk Current Injection Test with Amplitude and Phase Control,” EMC Zurich 2007, Germany, 2007.

[41] F. Grassi, G Spadacini, F. Marliani and S. A. Pignari: “Use of Double Bulk Current Injection for Susceptibility Testing of Avionics,” IEEE Transactions on Electromagnetic Compatibility, Vol. 50, No. 3, Aug. 2008.

[42] H. Rakouth, C. Cammin, L. Comstock and J. Ruiz: “Automotive EMC: Key Concepts for Immunity Testing” IEEE International Symposium on Electromagnetic Compatibility, USA, Aug. 2007

[43] J. R. Nicholson and J. A. Malack: “RF impedance of power-lines and line impedance stabilization networks in conducted interference measurements,” IEEE Transactions on Electromagnetic Comparability, May 1973.

[44] P. J. Kwasniok, M.D. Bui, A.J. Kazlowski and S.S. Richly: “Technique for measurement of input impedance of electronic equipment in the frequency range from 1 MHz to 1 GHz,” IEEE Transactions on Electromagnetic Compatibility, No. 4, Nov. 1992.

[45] P. J. Kwasniok, M.D. Bui, A.J. Kazlowski and S.S. Stuchly: “Technique for Measurement of Power-Line Impedance in the Frequency Range from 500 kHz to 500 MHz,” IEEE Transactions on Electromagnetic Comparability, No. 1, Feb. 1993.

[46] P. J. Kwasniok, M.D. Bui, A.J. Korlowski and S.S. Stuchly: “An improved method of measuring power-line impedance using two current probes,” IEEE Transactions on Electromagnetic Comparability, No. 4, Nov. 1993.

[47] K. Y. Sec and L. Yang, “Measurement of noise source impedance of SMPS using two current probes,” Electronics Lerners, Oct. 2000.

[48] B. L. Harlacher and R. W. Stewan: “Comparison of common mode impedance measurements using 2 current probe technique versus VII techniques for ClSPR 22 conducted emission measurement,” IEEE International Symposium on Electromagnetic Compatibility, Canada, August 2001.

[49] G. Liu, Y. Ding, C. Chen, R. Kautz, J. L. Drewniak, D.J. Pommerenke, and M. Y. Koledintseva: “A Dual-Current-Probe Method for Characterizing Common-Mode Loop Impedance,” IEEE Instrumentation and Measurement Technology Conference, USA, May 2003.

[50] A. Junge and A. Enders: “Kontaktlose Bestimmung von Leitungsimpedanzen bei Hochfrequenz,” EMV-Düsseldorf, Germany, 2006.

[51] A. Junge: “Kontaktlose Verfahren zur breitbandigen Messung an Leitungen bei Hochfrequenz,” TU Braunschweig, Dissertation, 2009.

[52] F. Zur Nieden: “Charakterisierung und Modellierung von ESD-Pulsquellen,” TU Dortmund, Dissertation, 2014.

[53] International Organization for Standardization, ISO 11452 Revisions, http://www.iso.org/, 2016

[54] ISO 11452-4: Road vehicles – Component test methods for electrical disturbances from narrowband radiated electromagnetic energy - Part 4: Harness excitation methods,” 2011.

[55] ISO 11452-1: “Road vehicles – Component test methods for electrical disturbances from narrowband radiated electromagnetic energy - Part 1: General principles and terminology,”.

[56] C. L. Holloway, R. R. DeLyser; R. F. German, P. McKenna, M. Kanda: “Comparison of Electromagnetic Absorber Used in Anechoic and Semi-Anechoic Chambers for Emissions and Immunity Testing of Digital Devices,” IEEE Transactions on Electromagnetic Compatibility, Vol. 39, No. 1, Feb. 1997.

[57] M. Wiles and V. Rodriguez: “Choosing the Right Chamber for Your Test Requirements,” EMC Directory & Design Guide, http://www.ets-lindgren.com/, May 2010.

[58] W. H. Emerson: “Electromagnetic wave absorbers and anechoic chambers through the years,” IEEE Transactions on Antennas and Propagation, USA, Jul. 1973.

[59] D. Hansen, N. Ari and H. Garbe: “An Investigation into the Scattering a Radiation Characteristic of RF-Absorbers,” IEEE International Symposium on Electromagnetic Compatibility, USA, 1988.

[60] Texas Instruments Inc., LM35 Precision Centigrade Temperature Sensors, Datasheet, http://www.ti.com/, Oct 2016.

[61] C.L Holloway, R.R. DeLyser, R.F. German: “Comparison of Electromagnetic Absorber Used in Anechoic and Semi-Anechoic Chambers for Emissions and Immunity Testing of Digital Devices,” IEEE Transactions on Electromagnetic Compatibility, Feb. 1997.

[62] K. Kurokawa: “Power Waves and the Scattering Matrix,” IEEE Transactions on Microwave Theory and Techniques, Vol. 13, No. 2, Mar. 1965.

[63] R. W. Beatty and D. M. Kerns: “Relationships between different kinds of network parameters, not assuming reciprocity or equality of the waveguide or transmission line characteristic impedances”, Proceedings of the IEEE, Vol. 52, No. 1, Jan. 1964.

[64] D. A. Frickey: “Conversions between S, Z, Y, H, ABCD, and T parameters which are valid for complex source and load impedances,” IEEE Transactions on Microwave Theory and Techniques, Feb. 1994.

[65] C. R. Paul: “Analysis of Multiconductor Transmission Lines,” John Wiley & Sons, New York, 1994.

[66] F. M. Tesche, M. V. Ianoz and T. Karlsson: “EMC Analysis Methods and Computational Models,” John Wiley & Sons, 1997.

[67] M.J. Degerstrom, B.K. Gilbert and E.S. Daniel: “Accurate resistance, inductance, capacitance, and conductance (RLCG) from uniform transmission line measurements,” Electrical Performance of Electronic Packaging Conference, IEEE-EPEP, Oct. 2008.

[68] M.K. Sampath, “On addressing the practical issues in the extraction of RLGC parameters for lossy multi-conductor transmission lines using S-parameter models,” Electrical Performance of Electronic Packaging Conference, Oct. 2008.

[69] Avant! Corporation, Star-Hspice Manual, Jun. 2001

[70] C. A. Balanis: “Modern Antenna Handbook,” John Wiley & Sons, New York, 1994.

[71] M. Bittera, V. Smiesko, K. Kovac and J. Hallon: “Directional properties of the BiLog antenna as a source of radiated electromagnetic interference measurement uncertainty,” IET Microwaves, Antennas & Propagation, Vol. 4, No. 10, Oct. 2008.

[72] Elmac Services, “What to look for in an EMC Antenna,” Application Note: SAN011, http://www.elmac.co.uk/, Oct. 2016.

[73] Teseq AG, CBL 6144 X-WING BILOG ANTENNA 26 MHz to 3 GHz, Datasheet, http://www.teseq.com/.

[74] CISPR 16-1-4: “Specification for radio disturbance and immunity measuring apparatus and methods – Part 1-4: Radio disturbance and immunity measuring apparatus – Ancillary equipment – Radiated disturbances,” 2008

[75] S. Miropolsky and S. Frei: “Introduction to S-parameter Measurements using Vector Network Analyzer,” 2012.

[76] Fischer Custom Communications, http://www.fischercc.com/, March 2016.

[77] R. Feldtkeller: “Theorie der Spulen und Übertrager,” Hirzel Verlag, Stuttgurt 1963.

[78] Wm. T. McLyman: “Transformer and Inductor Design Handbook,” Marcel Dekker, Inc., 2004

[79] G. R. Skutt, “High-frequency dimensional effects in ferrite-core magnetic devices,” Dissertation, Virginia Polytech. 1996.

[80] C.E. Cuellar Quispe: “HF Characterization and Modeling of Magnetic Materials for Passive Components Used in EMI Filters,” Dissertation, Lille University, 2013.

[81] D. C. Smith: “Current Probes, More Useful Than You Think,” IEEE Int. Symp. EMC, Denver, pp. 284-289, Aug. 1998.

[82] C.F.M. Carobbi and L.M. Millanta: “The Loading Effect of Radio-Frequency Current Probes,” IMTC 2006, Italy, Apr. 2006.

[83] C.F.M. Carobbi and L.M. Millanta: “Circuit Loading in Radio-Frequency Current Measurements: The Insertion Impedance of the Transformer Probes”, IEEE Transactions on Electromagnetic Compatibility, Vol. 59, No. 1, Jan. 2010.

[84] A.R. Ruddle, S.C. Pomeroy and D. D. Ward: “Calibration of Current Transducers at High Frequencies,” IEEE Transactions on Electromagnetic Compatibility, Vol. 43, No. 1, Feb. 2001.

[85] G. Cerr, R. De Leo, V. M. Primiani, S. Pennesi and Paola Russo: “Wide-Band Characterization of Current Probes,” IEEE Transactions on Electromagnetic Compatibility, Vol. 45, No. 14, Nov. 2001.

[86] Tektronix, Inc., AC Current Probes: CT1, CT2, CT6 Data Sheet, http://www.tek.com/, Mar. 2016.

[87] CISPR 16-1-2: “Specification for radio disturbance and immunity measuring apparatus and methods – Part 1-2: Radio disturbance and immunity measuring apparatus – Ancillary equipment – Conducted disturbances,” 2003.

[88] M. Bartoli, A. Reatti and M. K. Kazimierczuk: “High-frequency models of ferrite core inductors,” Industrial Electronics, Control and Instrumentation, Sep.1994.

[89] Keysight Technologies, Application Note 1369-1, http://www.keysight.com/, “Solutions for Measuring Permittivity and Permeability with LCR Meters and Impedance Analyzers,” 2016.

[90] H.E. Bussey: “Measurement of RF Properties of Materials a Survey,” Proceedings of the IEEE, Vol 55, Jun. 1967

[91] A.C. Lynch: “Precise Measurements on Dielectric and Magnetic Materials,” IEEE Transactions on Instrumentation and Measurement, Vol 23, No 4, Dec. 1974.

[92] C. Rostamzadeh, F. Grassi and F. Kashefi: “Modeling SMT Ferrite Beads for SPICE Simulation,” IEEE International Symposium on Electromagnetic Compatibility, USA, Aug. 2011.

[93] Fair Rite Product Corp., Application Note Materials - Fair Rite, http://www.fair-rite.com/design-tools/materials/, Oct. 2016.

[94] Keysight Technologies, Application Note 1287-3, http://www.keysight.com/, “Applying Error Correction to Network Analyzer Measurements,” 2002.

[95] T. Bednorz: “Measurement Uncertainties for Vector Network Analysis,” Rohde & Schwarz Application Note 1EZ29_1E, May 1998.

[96] L.e. Duda, R. D. Moyer “Determination of the Uncertainties of Reflection Coefficient Measurements of a Microwave Network Analyzer,” NCSL Workshop & Symposium, USA, 1998.

[97] O. Ostwald, “Frequently Asked Questions about Network Analyzers ZVR,” Rohde & Schwarz Application Note IEZ38_3E, Jan. 1998.

[98] Keysight Technologies, Application Note 5989-5935, http://www.keysight.com/, “Ultra-Low Impedance Measurements Using 2-Port Measurements,” 2007.

[99] CISPR 22: “Information technology equipment - Radio disturbance characteristics - Limits and methods of measurement,” 1997.

[100] D. E. Bockelman and W. R. Eisenstadt: “Combined Differential and Common-Mode Scattering Parameters: Theory and Simulation,” IEEE Transactions on Microwave Theory and Techniques, Vol. 43, 1995.

[101] D. E. Bockelman and W. R. Eisenstadt: “Pure-Mode Network Analyzer for On-Wafer Measurements of Mixed-Mode S-Parameters of Differential Circuits,” IEEE Transactions on Microwave Theory and Techniques, Vol. 43, 1997.

[102] O. Zinke and H. Brunswig: “Hochfrequenztechnik 1 - Hochfrequenzfilter, Leitungen, Antennen,” Springer, Berlin, 2000

[103] Fischer Custom Communications, Inc., Bulk Current Injection Probes, http://www.fischercc.com/, Oct. 2016.

List of Publications

1. Hassanpour Razavi, S.A.; Frei, S.: "*Characterization of Current Transformers for Impedance Measurements in Automotive Immunity Test Setups,"* EMC Europe, Wroclaw, Poland, 2016

2. Hassanpour Razavi, S.A.; Frei, S.: *"Characterization of DUT impedance in immunity test setups,"* Advances in Radio Science 14, 155–159, Miltenberg, Germany, 2016

3. Hassanpour Razavi, S.A.; Zeichner, A.; Frei, S.: *"Erhöhung der Korrelation zwischen BCI- und Antennenprüfverfahren durch Bestimmung von Abschlussimpedanzen mittels potenzialfreier Messung mit Stromsensoren, "* EMV Düsseldorf, Germany, 2016

4. Hassanpour Razavi, S.A.; Miropolsky S.; Frei, S.: *"Measurement-Based Circuit Modeling of Conducted and Radiated Automotive Immunity Test Setups,"* EMC Europe, Gothenburg, Sweden, 2014

5. Hassanpour Razavi, S.A.; Miropolsky S.; Frei, S.: *"Verbesserung der Korrelation zwischen dem BCI- und dem Antennenprüfverfahren für Kfz-Komponenten durch Anpassung von Verstärkerleistung und Position der BCI-Zange,"* EMV-Düsseldorf, Germany, 2014

6. Zeichner, A.; Hassanpour Razavi, S.A; Frei S.: "*Immunity of Modulation Schemes in Automotive Low Bitrate Power Line Communication Systems,"* EMC Europe, Dresden, Germany, 2015

7. Hilger, U.; Hassanpour Razavi, S.A.; Miropolsky S.; Frei, S.: *"Untersuchung des Einflusses von Parametervariationen auf die Störfestigkeit differentieller Kfz-Bussysteme,"* EMV-Düsseldorf, Germany, 2014

8. Scheier, S.; Hassanpour Razavi, S.A.; Frei, S.: *"Simulationsbasierte Optimierung von ESD-Schutzkonzepten für Integrierte Schaltungen,"* ASIM Tagung, Düsseldorf, 2013